Quantum Dynamics of Photochemical Model Reactions via Conical Intersections

–

Quantendynamik Photochemischer Modellreaktionen entlang konischer Durchschneidungen

INAUGURAL – DISSERTATION

to obtain the academic degree
Doctor rerum naturalium (Dr. rer. nat.)
submitted to the Department of Biology, Chemistry and Pharmacy
of Freie Universität Berlin

by

Sherin Alfalah

from Kuwait

February, 2010

Erstgutachter:	Prof. Dr. Jörn Manz
Zweitgutachter:	Prof. Dr. Leticia González
Tag der Disputation:	15. 02. 10

Publications

S. Alfalah, O. Deeb, S. Zilberg, Y. Haas, Chem. Phys. Lett., *Solvent effect on the conical intersection of 4-cyclopentadienylidene-1,4-dihydropyridine (CPDHP)*, 459, 100 (2008).

S. Alfalah, S. Belz, O. Deeb, M. Leibscher, J. Manz, S. Zilberg, J. Chem. Phys., *Photoinduced quantum dynamics of ortho- and para-fulvene: Hindered photoisomerization due to mode selective fast radiationless decay via a conical intersection*, 130, 124318 (2009).

S. Alfalah, D. Kinzel, J. González-Vázquez, L. González, Chem. Phys., *Nonadiabatic photoisomerization versus photodissociation dynamics of the chiral fluoroethylene derivative (4-methylcyclohexylidene)fluoromethane*, submitted.

Abstract

This work deals with quantum chemistry and quantum dynamics of cis-trans isomerization via conical intersections for three model systems of reduced dimensionality. The focus is on obtaining clear pictures of the quantum dynamics in the excited electronic state using fulvene and 4-(methyl-cyclohexylidene)-fluoromethane as model systems. The effect of solvent polarity on the conical intersection is also investigated using 4-cyclopentadienylidene-1,4-dihydropyridine as model system.

Ab initio potential energy surfaces are built for the ground and first excited electronic states of the molecules 4-(methyl-cyclohexylidene)-fluoromethane and 4-cyclopentadienyl idene-1,4-dihydropyridine. For fulvene , model potential energy surfaces are generated based on analysis of the corresponding ab initio potential energy surfaces. To investigate the dynamics of the isomerization process, the nuclear wave packets evolving on one- or two-dimensional coupled potential energy surfaces are simulated for fulvene and the 4-(methyl-cyclohexylidene)-fluoromethane. For this purpose, the original adiabatic potential energy surfaces with kinetic couplings are transformed to the diabatic ones with potential couplings. To investigate the effect of laser pulses on the dynamics of the isomerization process, preliminary simulations based on one-dimensional ab inito potentials and dipole functions of the 4-(methyl-cyclohexylidene)-fluoromethane model system are carried out.

It is found that for fulvene, radiationless decay due to vibrations along the symmetric allylic stretch is faster than the radiationless decay along the torsional coordinate. For 4-(methyl-cyclohexylidene)-fluoromethane, torsional/rotational motions can be conserved in the excited as well as in the ground state. Furthermore, for the model 4-cyclopentadienylidene-1,4-dihydropyridine, the conical intersection between the ground and first excited electronic state shifts in non-polar solvents, whereas in polar solvents the degeneracy is lifted.

Kurzfassung

Die vorliegende Dissertation beschäftigt sich mit der Quantenchemie dreier Modellmoleküle und deren Quantendynamik bei Cis-trans-Isomerisierungen, die über eine konische Durchschneidung verlaufen. Als Modellsysteme für die Untersuchung der Quantendynamik im angeregten elektronischen Zustand dienen die Verbindungen Fulven sowie das 4-(Methyl-cyclohexyliden)-fluoromethan und deren Bewegungen entlang ausgewählter Koordinaten. Anhand des Moleküls 4-Cyclopentadienylidene-1,4-dihydropyridin wird der Einfluss der Polarität des Lösungsmittels auf die konische Durchschneidung aufgezeigt.

Ab initio Potenzialenergieflächen werden für den Grundzustand und den ersten angeregten elektronischen Zustand für die Modellverbindungen 4-(Methyl-cyclohexyliden)-fluoromethan and 4-Cyclopentadienylidene-1,4-dihydropyridine berechnet, während für das Fulvenmolekül Modellpotenziale genutzt werden, die auf ab initio Daten beruhen. Um die Dynamik der Isomerisierung zu erforschen, werden die Bewegungen der Kernwellenpakete des Fulvens sowie des 4-(Methyl-cyclohexyliden)-fluoromethans auf ein- oder zweidimensionalen Potenzialflächen simuliert. Hierfür werden die erhaltenen adiabatischen Potenziale und deren kinetische Kopplungen untereinander in diabatische Potenziale mit Potenzialkopplungen umgewandelt. Der Einfluss der Laseranregung auf die Dynamik der Molekülisomerisierung entlang eines eindimensionalen Reaktionspfades wird am Beispiel des 4-(Methyl-cyclohexyliden)-fluoromethans berechnet.

Beim Fulven erfolgt der strahlungslose Zerfall aus dem angeregten elektronischen Zustand durch die symmetrische allylische Streckschwingung des Cyclopentadiengerüsts schneller als über die Torsion entlang der C=C Doppelbindung. Beim 4-(Methyl-cyclohexyl iden)-fluoromethan wird gezeigt, wie eine Rotations-Torsions-Bewegung sowohl im Grundzustand als auch im angeregten Zustand erhalten bleiben kann. Die konische Durchschneidung zwischen dem Grundzustand und dem ersten angeregten elektronischen Zustand des 4-Cyclopentadienyliden-1,4-dihydropyridins wird lokalisiert und deren Verschiebung bzw. Aufhebung unter dem Einfluss unpolarer und polarer Lösungsmittel herausgestellt.

Acknowledgement

I would like to express my thanks to many people who have supported me throughout the past four and half years..

I am grateful to my advisors, Jörn Manz, Omar Deeb, Leticia González and Monika Leibscher for their guidance, kindness, patience, and commitment to teaching. I am also grateful to Jesus González for his kind guidance and interesting discussions.

I would like to thank Shmuel Zilberg and Yehuda Haas for kind advice and cooperation in locating the conical intersections.

I would like to thank Steffen Belz and Daniel Kinzel for being so willing to answer questions and for all their kind help, in particular, I would like to thank Steffen Belz and Thomas Grohmann for their kind help in submitting my thesis. I would like to thank Holger Naundorf for the technical help with the computers and software.

To the Deeb group, AG Manz and AG González past and present: thank you for making the working environment so friendly and open.

I also thank the Deutsche Forschungsgemeinschaft for the financial support of my Ph.D. study in the frame work of a trilateral cooperation between Israel, Palestine, and Germany.

I would like to thank my family, especially my dear parents for their support and encouragement all the times. Finally, I would like to express my deep gratefulness for the spirit of my grandfather who was motivating and supporting me all the time. I hope his spirit is happy now for making one of his dreams true.

Contents

Chapter 1

Introduction

The development of civilization has always been severely related to the design and construction of devices, from the wheel to the jet engine, able to facilitate human movement and travel. Nowadays scientists investigate the possibility of designing and constructing motors and machines at the nanometer scale, i.e. at the molecular level. Chemists are able to manipulate atoms and molecules and are therefore in the ideal position to develop bottom-up approaches for the construction of nanoscale devices [1]. Synthetic molecular motors are molecular machines capable of rotation under energy input. Although the term "molecular motor" has traditionally referred to a naturally occurring protein that induces motion, some groups also use the term when referring to non-biological, non-peptide synthetic motors. The prospect of synthetic molecular motors was first raised by the nanotechnology pioneer Richard Feynman in 1959 in his classic talk *There's Plenty of Room at the Bottom*. The basic requirements for a synthetic motor are repetitive 360 degrees motion, the consumption of energy and unidirectional rotation. The first two efforts in this direction, the chemically driven motor by Kelly and co-workers and the light-driven motor by Feringa and co-workers, were published in 1999 in the same issue of Nature [2, 3]. The words "motor" and "machine" are often used interchangeably when referred to molecular systems. The operation of a molecular machine is accompanied by partial conversion of free energy into heat, regardless of the chemical, photochemical, and electrochemical nature of the energy input. In the situation of artificial nanomotors, stimulation by light has several advantages compared to stimulation by chemical or electrochemical means. First, the amount of energy given to a chemical system by using photons can be carefully controlled by the wavelength and intensity of the exciting light. Other properties of light, such as polarization, can also be used. Lasers provide the opportunity of working

in very small spaces and extremely short time domains. On the other hand, the irradiation of large areas and volumes can be easily carried out, in that way allowing the parallel (or even synchronous) concentration on a very high number of individual nano-devices. Furthermore, photochemical methods are useful for monitoring the operation of the motor. The construction of artificial molecular machines is one of the major contemporary challenges in nanoscience [4, 5, 6]. The functioning of these machines will critically depend on the ability to power and control rotary movement like in the macroscopic motors used in daily life and the rotary motors present in biological machines, most elegantly seen in ATP synthase [7, 8, 9]. The synthesis of molecular motors and the demonstration of unidirectional rotary motion driven by light or chemical conversions has laid the foundation for future nanomotors [7, 8, 9, 10, 11]. While the realization of building useful nanomachines remains far off, a general consensus abounded that investigating biological systems and understanding the implications of the laws of thermodynamics and quantum mechanics for the behavior of nanostructures will help drive important advances in the seek for molecular machinery. Molecular rotors were demonstrated to have practical applications and many experimental studies indicated that highly directed translation and rotation of individual molecules are just approaching. Recently, the first quantum simulations have been carried out, representing the ignition of unidirectional intramolecular rotations in chiral molecules by means of linearly polarized laser pulses in the infrared (IR) frequency domain [12, 13, 14]. This approach can be an alternative to chemical, electrochemical or photochemical stimuli of molecular rotors [3, 15, 16, 17, 18, 19], which is an important challenge in molecular engineering [20, 21, 22, 23]. It was found in Ref [24] that quantum ignition of intramolecular rotation can be accomplished by first, a few-cycle infrared (IR) laser pulse excites the torsional vibration in an oriented molecule. Consequently, a Franck-Condon type transition is induced from the electronic ground to the excited state by a well-timed ultrashort ultraviolet (UV) laser pulse. As a result, the torsional motion is converted into a unidirectional intramolecular rotation, with high angular momentum ($\approx 100\,\hbar$). The mechanism is confirmed using representative laser driven wave packets which are propagated on ab initio potential energy curves of the model system (4-methyl-cyclohexylidene)fluoromethane.

1.1 Phase Localization of Conical Intersections: Quantum Chemistry–Quantum Dynamics (PLCI–QC–QD) Approach

This thesis is part of a trilateral project that aims to predict, analyze and propose laser pulses for the control of photochemical reactions which proceed via conical intersections, by means of a combination of three quantum methods. These include (1) phase localization of conical intersections (PLCI), (2) state–of–the–art quantum chemical (QC) calculations of relevant potential energy surfaces and couplings, and (3) quantum dynamics (QD) propagation of nuclear wavepackets and the design of laser pulses for the control of reaction dynamics via conical intersections. The ultimate general purpose of these studies is to analyze molecular motions, e.g. in order to drive a molecular motor or switch by laser pulses. Such analysis is performed using models with reduced dimensionality. The effect of the environment on conical intersections is also considered. The three fields that are applied in this thesis will be discussed shortly in this section.

1.1.1 Phase Localization of Conical Intersections (PLCI)

Molecular rotary motors are systems capable of undergoing unidirectional and repetitive rotations under the action of external energy inputs. The construction of molecular rotary motors causes several challenges, mainly because it is difficult to satisfy the unidirectional rotation requirement. Now, artificial rotary motors driven by light have only been obtained by exploiting a C=C photoisomerization reaction in alkenes. Photochemical reactions often give different products than thermal ones. A full understanding of such reactions is needed for some of the most important processes in nature such as photosynthesis, vision and the preparation of novel compounds. Unlike thermal reactions, which proceed on a single potential surface, photochemical reactions involve at least two potential surfaces. Quantum methods have been very successful in analyzing the path of thermal reactions and the techniques methods developed for this purpose can also be extended to photochemical ones. The most competent transition from one surface to another is at degenerate points (conical intersections, CI). The computational location of CIs involves high level quantum chemical calculations which are now feasible using modern computer technology. Several methods were developed for this purpose and have been applied to explain many different reactions. A model developed by Haas and Zilberg [25, 26, 27] leads to locate the conical intersection relevant to a given reaction. The model is based

on the pioneering work of Teller [28] and the phase change theorem of Herzberg and Longuet-Higgins [29, 30] who noted the singular behavior of the electronic wavefunction around a degeneracy. This observation is the basis of the approach used in this study to localize the conical intersection. The model used in this approach allows the efficient calculation of the properties of CIs in many systems [25, 26, 27, 31]. The basic assumption is the total wavefunction of a molecular system that can be written approximately as the product of an electronic wave function and a nuclear one (the Born-Oppenheimer approximation). The phase change theorem considers possible changes in the phase of the total electronic wave function, when the system goes along a closed trajectory around a point in phase space. It was shown that a CI necessarily is found in a system, if the total electronic wave function changes its phase upon traversing a complete loop. In the phase localizing of conical intersection (PLCI) model, reaction coordinates are used to construct the loop. A reaction is phase preserving (**p**) or phase inverting (**i**) depending on whether the total electronic wave function preserves its sign or inverts it during the reaction. Three reactions are typically required to form a complete loop, converting a reactant A to B, B to C and C back to A (see Figure 1.1). The A, B and C species are isomers, differing in their electron spin-pairing arrangements (i.e., chemical bonding). The loop is formed around these isomers, termed as anchors. If one or all three reactions are phase inverting, a CI arises within the loop [25, 26, 27]. If a photochemical reaction is initiated by exciting molecule A, for example, and the system passes from the electronically excited state to the ground state via the conical intersection, two products B and C may be formed. Depending on the properties of the system, a different number of anchors may be required. Sometimes, a reactant and a product may be connected by two distinct elementary reactions, one is phase preserving and the other is phase inverting. If so, a loop enclosing a CI is formed from only two species, and a single product is expected from photo-excitation.

1.1.2 Potential Energy Surfaces (PES)

On the frame of the Born–Oppenheimer ansatz [32], the quantum dynamics is governed by the structure of the PES in the ground and excited electronic states, the couplings between these states, and the nuclear masses. In the classical mechanics approach to photochemical reactions, studying the reaction dynamics of a polyatomic molecule is essentially figured as placing 'billiard balls' on these PESs, near the Franck-Condon (FC) point, and following their trajectories towards one or the other channel. Potential surfaces are key quantities for understanding molecular processes. Due to the existence of wells, barriers, avoided crossings, conical intersections etc., rather complicated topographies, which can hardly be guessed or parameter-

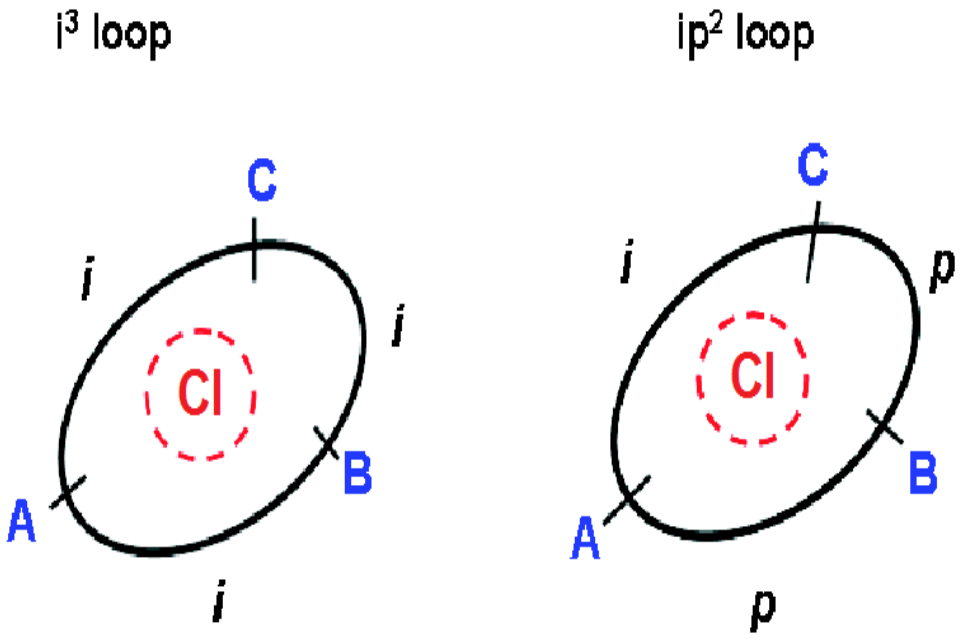

Figure 1.1: $\mathbf{i}^3$ (left) and $\mathbf{ip}^2$ (right) Longuet-Higgins loops; **i** indicates a sign inverting reaction and **p** indicates a sign preserving reaction. In $\mathbf{i}^3$ loop, the three reactions are sign inverting while in the $\mathbf{ip}^2$ loop, the two reactions are sign preserving, one sign inverting. Both $\mathbf{i}^3$ and $\mathbf{ip}^2$ loops are sign inverting loops, therefore, a conical intersection exists within the loop.

ized in a simple manner, are common. Potential surfaces and the couplings must be calculated by ab initio methods point by point, scanning at least that part of the PES that is sampled during the reaction of interest [33]. Typically at least 5-10 grid points are required for each coordinate. Finally, for practical applications, all the calculated points on the PES have to be fitted to an analytical function which then is employed in the dynamics calculations. The lack of high-quality complete PESs and couplings is still a bottleneck for realistic calculations and this situation will not essentially change in the near future.

1.1.3 Real-Time Dynamics and Effects of Laser Pulses

In addition to the knowledge about the PESs, the couplings and the location of the conical intersection, understanding the dynamics of the quantum wave packets evolving on those coupled surfaces is crucial for a full understanding of photochemi-

cal reactions. Time-dependent wave-packet methods have been employed to explore the quantum dynamics in the presence of conical intersection with ab initio based models as well as simplified generic model Hamiltonians. Processes like photodissociation and photoisomerization have been investigated by means of quantum dynamic calculations. One can theoretically describe photochemical processes and infer information about the reaction mechanism and ultimately about the multidimensional PES when light sources with weak intensities and long durations are used as in all traditional experiments. Typical time-scales for fragmentation are 10^{-12} seconds or even shorter whereas pulse lengths of conventional lasers are in the range of 10^{-9} seconds. Therefore, it is naturally impossible to analyze directly the time-dependence of the reaction. A 'revolution' in molecular dynamics set in at the end of the 1980s, when new laser systems with pulse lengths in the range of 10^{-14} (10 femtoseconds) or so became accessible. With such short light sources it is possible to 'see' directly molecular vibrations in the laboratory [34, 35, 36, 37, 38]. Ultrafast laser pulses have been employed as a "real-time camera" to observe elementary photochemical processes ever since femtosecond lasers became available to researchers in chemical physics [39]. An important class of photoreactions, which has successfully been investigated by femtosecond spectroscopy, is cis-trans photoisomerization [40, 41]. Femtosecond laser pulse techniques allow the use of pulsed excitations in order to control molecular dynamics. The control parameters are the laser frequencies, durations, polarizations and the delay time between the pulses. A typical control experiment uses two lasers with pulse durations in the sub-picosecond regime. First, a laser pulse excites the system from the ground to an upper electronic state. Since the laser has a small temporal width Δt, it excites a wave packet, i.e., a coherent superposition of several stationary (time-independent) states, in the excited manifold rather than a single stationary level as in an experiment with an infinitely long light pulse; the energetic width ΔE of the wave packet is given by $\Delta E \Delta t \approx h$. This wave packet is not an eigenstate of the upper PES and therefore it starts to move. The motion of this wave packet is then probed with the second laser, which is fired with a well defined delay time after the first pulse. The absorption spectrum or the ionization yield as a function of the delay time and pulse frequency then provide information about the time evolution of the molecule on the upper potential energy surface [42]. The ability to shape laser pulses allows for a generalized concept, in which phase and shape of a (femtosecond) laser pulse are optimized in order to create specially customized material wave packets and to manipulate their dynamics [43, 44]. Shi, Woody, and Rabitz developed "optimal control theory". This application relies on engineering control concepts to maximize a specific product yield by optimizing the tunable laser field [45, 46]. Judson and Rabitz extended this approach to include an evolutionary algorithm that directly compares the product yield with the desired output, iteratively re-optimizes the electric field, and thus solves the Schrödinger equation [43, 47]. This method was successfully tested experimentally in several

systems [44]. Mathematically, the problem of finding the right pulse shapes can be formulated as a problem in the calculus of variations, or as a problem of optimal control theory, which may be viewed as an application of the calculus of variations to problems with differential equation constraints. In the case of quantum optimal control, the relevant differential equation is the time-dependent Schrödinger equation, with the electric field interacting with the dipole of the molecule. Coherent control [48, 49] of the motion of a molecular system with continuous wave excitation and extensions to short and/or intense lasers has become a hot topic in the 1990s. The general question is very simple: can one find a particular pulse or sequence of pulses that forces the molecule to do what it refuses to do without the applied light field? Several control schemes have been suggested and applied to simple systems, mostly diatomics. The idea of coherent control is very appealing; some day it might become possible to open chemical reaction pathways, which are either energetically forbidden or just too inefficient without external field. However, a lot more investigations, both experimental and theoretical, are required before this goal is achieved. The internal motion of a realistic multimode system is, except for few simple cases, very complicated and to untie this motion is a terrifying task in itself.

1.1.4 Nonadiabatic Effects

Processes that take place on a single PES without coupling to other electronic states, i.e., processes for which the Born Oppenheimer approximation, are more the exception rather than the rule. Most of photochemical processes evolve on several potential energy surfaces and violate the Born Oppenheimer approximation (see section 2.1.1). This is expected if one recalls that with increasing excitation energy the density of electronic states generally increases as well, i.e., the separation between different PESs diminishes and as a consequence transitions between different states become more and more probable. Such transitions generally occur in the vicinity of avoided crossings and conical intersections where the mixing between different states is, by definition, largest. The theoretical description of nonadiabatic transitions is quite difficult. For a correct description one needs the nonadiabatic coupling terms (NACTs) which are often neglected in the Born Oppenheimer approximation. These coupling terms are usually ignored in dynamical treatments with the argument that the motion of the electrons is much faster than the nuclear motion so that the two can be adiabatically decoupled, i.e., one first solves the Schrödinger equation for the electrons with the nuclear coordinates being fixed, which yields the potential energy surfaces, and subsequently one solves the equations of motion for the nuclei on these potential energy surfaces. However, when two potential surfaces are close to each other, this approximation might break down and decoupling electronic and nuclear

motion becomes baseless. As a consequence one has to take into account simultaneous motion on several potential energy surfaces and the coupling terms between them. Therefore, rather than working in the adiabatic representation one makes a uniform transformation to a diabatic representation in which the above matrix elements are as small as possible [50, 51] (see section 2.2.2 and 2.2.2). Simulating the non-adiabatic nuclear dynamics quantum mechanically remains a challenge which increases with the number of nuclear degrees of freedom that have to be included and with the number of coupled electronic states. The price to be paid is that the electronic Hamilton operator in the new representation is not diagonal. However, the coupling due to the nondiagonal elements of the electronic Hamilton operator is easier to take into account than the kinetic energy coupling terms and therefore the diabatic representation is in practice the method of choice. Accurate approaches to calculate NACTs have been implemented in the quantum chemical program suites MOLPRO [52]. Recently, systematic determination and investigation of the NACTs and related seams of CIs were carried out for $C_2H_2^+$ [53, 54] and methylamine [55], demonstrating the often oscillatory and sharp peaks of (angular) NACTs which cannot easily be reproduced by model couplings. An alternative approach to calculate time-derivative coupling terms instead of the coupling vectors has been presented in [56]. Simulations of nuclear dynamics are usually carried out using a diabatic representation of the potential energy surfaces. A method for the diabatization of more than two coupled electronic states has been developed by M. Baer (see Ref. [57]), which leads to quantization rules for the NACTs.

1.2 Goals of this Thesis

The principal goal of this thesis is to obtain the clearest picture of the molecular dynamics in the excited electronic state as the molecule leaves the Franck-Condon region, passes through the 'transition state' (i.e., the barrier, if there is any), and finally reaches the reaction channel(s) of efficient rotation (for molecular motors) competing against fragmentation. An ultimate question is whether laser radiation can be used to control the photochemistry of the models used in this study to produce molecular rotors. Key questions are: What is the lifetime of the molecule in the upper state and how does this lifetime depend on the excitation energy? What is the branching ratio for the possible chemical channels? Is the reaction governed by one and only one electronic state or does it take place on several potential energy surfaces? All of these questions are ultimately determined by the shape of the potential energy surface of the particular excited state, the couplings and the masses of the nucleus. Therefore, the excited state PES and the couplings are the

cornerstone for understanding the photochemical reaction of polyatomic molecules. For this purpose, three model systems will be used in this thesis:

Fulvene. Fulvene is known to have CIs between the ground and first excited electronic states, S_0 and S_1, respectively [58, 59, 60]. It has been shown that CIs exist along the seam for all torsion angles, connecting the CI at planar structure with the CI at twisted configuration [61, 62]. The last CI is associated with cis–trans isomerization and has been located by means of the Longuet–Higgins method [60]. This study aims to investigate and compare the radiationless decay due to vibration along symmetric allylic stretching coordinates and the torsion coordinates. These results have been confirmed in later studies on more accurate three dimensional ab-initio PES where it has been shown that after vertical excitation, the fast radiationless decay along the symmetric allylic stretching coordinates prevents the slower torsion of the CH_2 group (see Ref [63]). Recently, some dynamical studies has been carried out on the fulvene molecule [63, 64, 65]. The authors in Ref. [63, 64, 65] proposed a wavepacket interferometric scheme for the separation of different nuclear spin isomers. In this study, we investigate the photoinduced nonadiabatic dynamics of this symmetric model, fulvene, by a combination of quantum chemical ab initio calculations and quantum dynamical simulations. We will explore the quantum dynamics of the corresponding photoexcited nuclear wavepacket on the model ground and first excited electronic states potential energy surfaces of fulvene. Therefore, a three-dimensional model Hamiltonian for the cis–trans isomerization of fulvene will be constructed. The parameters for the adiabatic model PES are obtained from quantum chemical ab initio data. Finally, we will discuss the propagation of photoexcited nuclear wavepacket on the coupled surfaces and the corresponding ultrafast non-radiative decay caused by the CIs. We will use the fulvene molecule as a model to carry out 2D dynamics simulations for two different models, one using symmetric and anti-symmetric allylic stretch modes and one using torsion and anti-symmetric allylic stretch mode, using a model Hamiltonian with linear coupling. This chapter aims to learn something general on non-adiabatic vibrations and torsional motion.

4-(methyl-cyclohexylidene)-Fluoromethane (4MCF). Chiral 4MCF molecule is a fluoroethylene derivative with two R/S enantiomers connected by a torsion around the C=C double bond. Analogous to the degeneracy points found for fluoroethylene [66], CIs involving torsion, pyramidalization, and H–atom migration have been reported for 4MCF [67]. A new CI associated with the elimination of HF has alsox been located [68]. Based on these optimized CIs, it was proposed that irradiation of 4MCF yields the chiral isomer upon C=C rotation in the presence of polar

solvents, while in gas phase, dissociation of the HF fragment should be observed [68]. 4MCF was proposed as a model system for a light-induced chiral molecular switch or a molecular rotor [24, 69, 70]. All these devices are originated from the ability of 4MCF to switch between the R/S enantiomers efficiently, generated by specific laser or sequence of laser pulses especially designed for this purpose. Dynamical studies on 4MCF have only considered the torsion and pyramidalization coordinates so far [69, 70, 24]. For this model with broken symmetry, we will investigate the effect of laser pulses which may turn out useful for future investigations of controlling efficient rotations of the HF "propeller" fragment, competing against the HF elimination as a non-desired competing mechanism. That should obviously be avoided, for the photoisomerization reaction. The competing dynamics are demonstrated on adiabatical as well as nonadiabatically coupled potential energy surfaces. This study consider explicitly the torsional dynamics around the C=C bond along with the competing HF photodissociation dynamics.

4-cyclopentadienylidene-1,4- Dihydropyridine (CPDHP). For this model system with its experimental twin, 1-butyl-4-(1H-inden-1-ylidene)-1,4-dihydropyridine (BIDP), we provide a calculation of the potential surface along the two coordinates predicted to lift the degeneracy according to the Longuet-Higgins loop method [29, 30]. A conical intersection that exists between the S_0 and S_1 surfaces of the CPDHP molecule in the gas phase and in non-polar solvents is shown to be eliminated in polar solvents. Burghardt and Hynes [71] used an extension of the two-electron two-orbital model of Bonačić-Koutecký et al. [72] to estimate the solvent effect on the CI of small protonated Schiff base. The solvent was modeled by 'Marcus-like' parabolas using a parameterized force constant. The authors in [71] describe two situations: a "frozen" solvent polarization where the solvent coordinate is fixed throughout, imposing a pronounced non equilibrium solvation situation, and the case of equilibrium solvation which implies extremely rapid solvent motion, adiabatically adjusting to the solute charge distribution. It was suggested in [71] that for an ultrafast spectroscopic experiment, the first case is the more realistic picture of solvation effects [73]. Using this approach, the authors found that a conical intersection existing in the gas phase (vacuum) can be eliminated. In this study we are interested in comparing with the experimental results observed in Ref [74], therefore our choice for the solvation model agrees in accordance with the suggestions in [71, 73]. This study provides a systematic calculation of the effect of solvent polarity on the energy of conical intersections that analyzes both polar and non-polar solvents. In this chapter we will first introduce the model system used to carry out the quantum mechanical calculations and then discuss the effect of the different solvents on the conical intersection.

1.3 Structure of the Thesis

The remainder of this thesis will consist of the following. Chapter 2 introduces the reader to the theoretical concepts of quantum chemistry and quantum dynamics. Specifically, the numerical methods used to obtain the results presented in this work are explained along with an approach to investigate of effects of laser pulses which may turn out useful for future investigations of control. The results of the model simulations are presented in chapters 4, 5 and 6, each chapter focusing on a different molecular model system. Chapter 3 presents the symmetric model system Fulvene. In this chapter we will explore the quantum dynamics of the corresponding photoexcited nuclear wavepacket on the model ground and first excited electronic states potential energy surfaces of fulvene. In chapter 4 the model system with broken symmetry (4-methyl cyclohexylidene)fluoromethane is presented. In this chapter, the two-dimensional potential energy surfaces as well as permanent and transition dipole moments for this system are presented. Furthermore, the results of quantum dynamical simulations for 4MCF as well as those for optimization of vibrational infra-red and ultra-violet pulses are presented. Chapter 5 represents the calculation of the potential surface along the two coordinates lifting the degeneracy of the 4-cyclopentadienylidene-1,4-dihydropyridine (CPDHP) molecule. This will allow investigating the effect of solvent polarity on the energy of conical intersections in both polar and non-polar solvents. Finally, chapter 7 contains the summary and an outlook.

Chapter 2

Theory

This chapter summarizes the theoretical concepts that are relevant to the quantum chemical and quantum dynamic investigations presented in this thesis. The time-independent Schrödinger equation will be introduced in Section 2.1, after which the electronic and nuclear Schrödinger equations will be treated separately, within the Born-Oppenheimer approximation. In section 2.3, solutions to the nuclear Schrödinger equations will be presented. The time-dependent nuclear Schrödinger equation (TDSE) is reviewed in section 2.4, including a discussion of numerical methods for solving the TDSE. Adiabatic and diabatic representations are discussed in section 2.2.2 and 2.2.2 while transforming of adiabatic states to diabatic ones is discussed in section 2.2.2. The chapter finishes with an approach to molecular control using laser fields in section 2.4.3.

2.1 The Time-Independent Schrödinger Equation (TISE)

To describe the state of a system in quantum mechanics, the existence of a function called the wave function or the state function is postulated. To obtain the desired information about a state, this wave function must be found. For this purpose, we need to solve the Schrödinger equation which is an eigenvalue problem, with state energies as eigenvalues.

$$\hat{H}|\Psi\rangle = E|\Psi\rangle. \tag{2.1}$$

Here, $|\Psi>$ is the state or wave function, E is the total energy and $\hat{H}$ is the quantum-mechanical energy operator which corresponds to the classical Hamiltonian total energy function (H). The Hamiltonian operator in the spin-free approximation ($\hat{H}$) is given, in atomic units, by the relation [33]:

$$\hat{H} = -\sum_{i=1}^{N} \frac{1}{2}\nabla_i^2 - \sum_{A=1}^{M} \frac{1}{2M_A}\nabla_A^2 - \sum_{i=1}^{N}\sum_{A=1}^{M} \frac{Z_A}{R_{iA}} + \sum_{i=1}^{N}\sum_{j>i}^{N} \frac{1}{r_{ij}} + \sum_{A=1}^{M}\sum_{B>A}^{M} \frac{Z_A Z_B}{R_{AB}} \quad (2.2)$$

The sum here is over all the N electrons and M nuclei of the system. M_A is the mass of nucleus A, Z_A is the charge of nucleus A, r_{ij} is the distance between electrons i and j, R_{iA} is the distance between electron i and nucleus A, R_{AB} is the distance between nuclei A and B and ∇_i^2 is the Laplacian which is given as

$$\nabla_i^2 = \left(\frac{\partial^2}{\partial x_i^2} + \frac{\partial^2}{\partial y_i^2} + \frac{\partial^2}{\partial z_i^2}\right). \quad (2.3)$$

Eq. 2.2 can be written as

$$\hat{H} = \hat{T}_e + \hat{T}_N + \hat{V}_{eN} + \hat{V}_{ee} + \hat{V}_{NN}. \quad (2.4)$$

Here, $\hat{T}_e$ is the kinetic energy operator of electrons, $\hat{T}_N$ is the kinetic energy operator of the nuclei, $\hat{V}_{eN}$ is the Coulomb attraction between the nuclei and electrons, $\hat{V}_{ee}$ is the repulsion between electrons and $\hat{V}_{NN}$ is the repulsion between the nuclei. As the separation between the electrons and nuclei goes to infinity ($R_{AB} \to \infty, R_{iA} \to \infty, r_{ij} \to \infty$), the three potential energy terms go to zero, corresponding to the zero level of potential energy. Considering all the coordinates of all N electrons and M nuclei in the system, the sum of all the terms in eq. 2.4 will give the molecular Hamiltonian. Solving the Schrödinger eq. 2.1 with the molecular Hamiltonian is a terrifying problem. Fortunately, there is a useful approximation to circumvent this problem in which one solves the equation by separating the electronic and nuclear motion. This approximation is outlined in section 2.1.1.

2.1.1 The Born-Oppenheimer Approximation and the Concept of a Potential Energy Surface (PES)

The Born-Oppenheimer approximation [75] is an essential first step in simplifying the molecular Schrödinger equation to the point so that computations can take place. In this approximation, due to the significant difference in mass between an electron ($m_e \sim 10^{-31} kg$) and nucleus ($M_A \sim 10^{-27} kg$), the nuclei are regarded as fixed while the electrons are moving in the field of nuclei. In this approximation the

wave function Ψ is written as a product of the electronic wave function Ψ_e and the nuclear one Ψ_{eN}

$$\Psi(r, R) \simeq \Psi_e(r; R)\Psi_{eN}(R), \tag{2.5}$$

where the electronic wave function Ψ_e depends explicitly on the electronic coordinates and parametrically on the nuclear coordinates. The electronic wave function Ψ_e is the solution of the electronic Schrödinger equation,

$$\hat{H}_e\Psi_e = E_e\Psi_e. \tag{2.6}$$

where $\hat{H}_e$ is the electronic Hamiltonian operator and E_e is the electronic energy. Within the Born-Oppenheimer approximation, the kinetic energy of the nuclei (T_N) can be neglected and the repulsion between the nuclei (V_N) can be considered to be constant. Any constant added to the Hamiltonian operator only adds to the operator eigenvalues (energy) and has no effect on the operator eigenfunctions. The remaining terms in eq. 2.2 form the electronic Hamiltonian. Omitting the nuclear kinetic and nuclear repulsion energy terms from the molecular Hamiltonian which is written as [33],

$$\hat{H}_e = -\sum_{i=1}^{N}\frac{1}{2}\nabla_i^2 - \sum_{i=1}^{N}\sum_{A=1}^{M}\frac{Z_A}{r_{iA}} + \sum_{i=1}^{N}\sum_{j>i}^{N}\frac{1}{r_{ij}}. \tag{2.7}$$

Because the nuclei are considered fixed, the electronic wave function depends explicitly on the electronic coordinates but parametrically on the nuclear coordinates and so does the electronic energy. This approximation holds in general if $(m_e/M_A)^{1/4} \ll 1$. The total energy for fixed nuclei ($E_{tot,e}$) must include the constant repulsion term,

$$E_{tot} = E_{tot,e} = E_e + \sum_{A=1}^{M}\sum_{B>A}^{M}\frac{Z_A Z_B}{R_{AB}}. \tag{2.8}$$

Once the electronic problem is solved, it is possible to solve for the motion of the nuclei. The total energy of an atomic arrangement ($E_{tot,e}(R_A)$) provides a potential for nuclear motion and can be represented as a curve or a multidimensional surface, with atomic positions as variables. This function constitutes a potential energy surface (PES), result of the Born-Oppenheimer adiabatic approximation, which allows us to model chemical reactions. A potential energy surface is a mathematical relationship linking molecular structure with its energy. Minima on the potential energy surface can then be identified with the classical picture of equilibrium structures of molecules (reactant, product and intermediates); saddle points of second order are related to transition states.

In eq. 2.2, since the electrons move faster than the nuclei, it is reasonable approximation to replace the electronic coordinates by values obtained by averaging over the electronic wave function [33]. In this effective electronic field, the nuclear Hamiltonian ($\hat{H}_{N,e}$) which describes the vibrational, rotational and translational motion of the molecule depending on the electronic state e can be expressed as [33]

$$\hat{H}_{N,e} = -\sum_{A=1}^{M} \frac{1}{2M_A} \nabla_A^2 + E_{tot,e}. \tag{2.9}$$

Solution to the electronic and nuclear Shrödinger equations will be discussed in sections 2.1.2 and 2.3, respectively. The nuclei move in an effective potential which is the electronic energy (including nuclear-nuclear interaction) as a function of the internuclear distances.

2.1.2 Solution of the Electronic Time Independent Schrödinger Equation (TISE)

The energy obtained by solving the electronic problem provides a potential energy for nuclear motion. Thus, solving the electronic problem will naturally provide us with the framework to solve the nuclear Schrödinger equation. Accordingly, we will review the electronic problem first, focusing on the methods that are used in this work.

Hartree Fock Approximation

The Schrödinger eq. 2.1 does not make any account of relativity from which the spin is an important property of the electron. The spin may be introduced into the many-electron wave function as an ad hoc by multiplying the wave function with a spin function (spin up function or spin down function). The wave function for a single particle is called an orbital (labeled with i index). The wave function that describes the spatial distribution of an electron k is a spatial orbital ($\psi_i(r_k)$). Here r_k refers to the position coordinates of electron k. To describe the electron completely, it is necessary to specify its spin. A wave function that describes both the spatial distribution of an electron and its spin is called a spin orbital ($\chi_i(x_k)$). Here x refers to the spatial and spin coordinates of electron k. For a set of K orthonormal spatial orbitals, a set of $2K$ orthonormal spin orbitals can be constructed. The electronic Hamiltonian H_e in eq. 2.6 can be solved exactly for hydrogen. For atoms containing

many electrons, obtaining highly accurate wave functions is nontrivial. Calculations often rely on the Hartree-Fock method in which an approximate antisymmetric wave function, or Slater determinant, is constructed from one-electron functions and then optimized [33]. For an N-electron system, this determinant is given as:

$$\langle x_1, ..., x_N \mid \Psi_0 \rangle = (N!)^{\frac{-1}{2}} \begin{vmatrix} \chi_1(x_1) & \chi_2(x_1) & ... & \chi_N(x_1) \\ \chi_1(x_2) & \chi_2(x_2) & ... & \chi_N(x_2) \\ \vdots & \vdots & \vdots & \vdots \\ \chi_1(x_N) & \chi_2(x_N) & ... & \chi_N(x_N) \end{vmatrix}. \tag{2.10}$$

This wave function $|\Psi_0\rangle$ is called a Slater determinant with N electrons occupying N spin orbitals, $(\chi_1, \chi_2, ..., \chi_N)$. A configuration state function (CSF) is a linear combination of Slater determinants where the coefficients are determined from symmetry. Applying the antisymmetry principle to the wave function introduces the exchange correlations, which means that the motion of the electrons with parallel spins is correlated.

To deal with the Schrödinger equation, it is necessary to apply the *variational principle* that states, for a given system with time independent Hamiltonian operator $\hat{H}$ and the lowest-energy eigenvalue E_0, if $|\Psi\rangle$ is any ortho-normalized well-behaved function of the coordinates of the system that satisfies the boundary conditions of the problem, then

$$\langle \Psi \mid \hat{H} \mid \Psi \rangle \geq E_0. \tag{2.11}$$

The variational principle allows us to calculate an upper bound for the system ground-state energy $|\Psi_0\rangle$. Equality is achieved if the wave function is exact.

In ab-initio methods, the wave function is used to describe the electronic structure where the Hartree-Fock (HF) approximation is used as a starting point. HF theory is an approach to find an approximate solution to the electronic Schrödinger eq. 2.6. The HF approximation depends on the wave function as an essential quantity. The wave function in the HF method is a single CSF. Another important attribute of the HF method is that, orbitals are obtained by means of the variational principle. The variational flexibility in the wave function is invoked in the choice of spin orbitals. Minimizing the energy with respect to the choice of the spin orbitals gives an eigenvalue eq. 2.12. This equation is called the HF equation.

$$\hat{f}(x_i)\chi(x_i) = \epsilon_i \chi(x_i), \tag{2.12}$$

where ϵ_i is the energy of the i^{th} orbital and $\hat{f}(x_i)$ is an effective one electron operator, called the *Fock* operator, of the form

$$\hat{f}(x_i) = -\frac{1}{2}\nabla_i^2 - \sum_{A=1}^{M} \frac{Z_A}{R_{iA}} + \nu^{HF}(x_i). \tag{2.13}$$

Here R_{iA} is the distance between the electron i and the nucleus A. $\nu^{HF}(x_i)$ is the average potential experienced by each electron i due to presence of other $N-1$ electrons. The idea of the HF approximation is to replace the many electron problem by a one electron problem where the interacting electron-electron potential is approximated by an average non-interacting electron-electron potential. The average potential consists of two parts; the classical Coulomb potential, $\hat{J}_b(x_i)$, and a non-classical term called the exchange potential, $\hat{K}_b(x_i)$, which arise because of the antisymmetric nature of the wave function. For instance, for electron i, $\hat{f}(x_i)$ is written by [33]

$$\hat{f}(x_i) = \hat{h}(x_i) + \sum_{b}^{N} \hat{J}_b(x_i) - \sum_{b}^{N} \hat{K}_b(x_i), \tag{2.14}$$

where

$$\hat{h}(x_i) = \frac{1}{2}\nabla_i^2 - \sum_{A=1}^{M} \frac{Z_A}{R_{iA}}. \tag{2.15}$$

The one-electron Coulomb and exchange operators $\hat{J}_b(x_i)$ and $\hat{K}_b(x_i)$ operating on the orbital $\chi_a(x_i)$ are expressed as

$$\hat{J}_b(x_i) \mid \chi_a(x_i)\rangle = \left[\langle \chi_b(x_j) \mid \frac{1}{\hat{r}_{ij}} \mid \chi_b(x_j)\rangle\right] \mid \chi_a(x_i)\rangle, \tag{2.16}$$

$$\hat{K}_b(x_i) \mid \chi_a(x_i)\rangle = \left[\langle \chi_b(x_j) \mid \frac{1}{\hat{r}_{ij}} \mid \chi_a(x_j)\rangle\right] \mid \chi_b(x_i)\rangle. \tag{2.17}$$

Here, the indices a and b refer to the occupied spin orbitals of electrons i and j, respectively. The two-electron potential operator $\hat{r}_{ij}$ describes the interaction of electron i with electron j. Integration over all space and spin coordinates of electron j, x_j, yields an effective one-electron potential for electron i.
The Coulomb operator, $\hat{J}_b(x_i)$ can be inferred classically as the average local repulsion potential, which electron i experiences sitting in the spin orbital χ_a, arising from electron j occupying spin orbital χ_b. The exchange operator, $\hat{J}_b(x_i)$, on the other hand, has no classical interpretation; operating on $\chi_a(x_i)$ leads to exchange electron i to the spin orbital χ_b. Unlike the Coulomb operator, the exchange operator is a nonlocal operator because the energy contribution comes from a delocalized interaction between electron i and electron j. By summing over all electrons $b \neq a$ in eq. 2.14 , we obtain a total averaged potential acting on the electron in χ_a, arising from the $N-1$ electrons in the other spin orbitals.

Roothaan-Hall Equations

As it was shown in section 2.1.2, the many-electron Schrödinger eq. 2.13 can be approximated by an averaged one-electron problem. The HF equation is an integro-differential problem which may be solved numerically for atoms but there are no practical numerical procedures available for molecules. A way to overcome this problem is to convert the equation into a set of algebraic equations which can be solved using standard matrix techniques by expanding the set χ_i into as a linear combination of N pre-chosen basis functions (η_j):

$$\chi_i = \sum_{j=1}^{N} C_{ij}\eta_j. \tag{2.18}$$

The resulting Roothaan-HF [76] matrix equation may be written

$$FC = SC\epsilon. \tag{2.19}$$

Here F is the *Fock* matrix, which has the elements

$$F_{jk} = \langle \eta_j(r) \mid \hat{f}(r) \mid \eta_k(r) \rangle, \tag{2.20}$$

C is the expansion coefficients square matrix. S is the overlap matrix, which has the element

$$S_{jk} = \langle \eta_j(r) \mid \eta_k(r) \rangle. \tag{2.21}$$

ϵ is the diagonal matrix of the orbital energies ϵ_i.

The exact solution for the HF eq. 2.12 conducts with exact HF spin orbitals [33]. In practice, it is possible to solve for the exact integro-differential eq. 2.14 numerically for atoms. For molecules, one introduces a set of basis functions for expansion of the spin orbitals and solve a set of matrix equations, see section 2.1.2. As the basis set approach completeness, the obtained spin orbitals approach the exact HF spin orbitals. The Fock operator has a functional dependence, through the Coulomb and exchange operators, on the solution χ of the pseudo-eigenvalue eq. 2.12. Hence, the HF equations are nonlinear equations which need to be solved iteratively using the Self-Consistent-Field (SCF) method [33]. One usually employs the variational principle and solve the electronic problem iteratively, until convergence is reached. For this purpose, we start with a guess of the molecular orbitals and construct the Fock matrix. Then solve eq. 2.12 to find the HF orbitals and calculate new molecular orbitals. This process is repeated. And after a certain number of iterations, it is usually found that the orbitals do not change from one iteration to another. At

this point, we reach convergence. As a consequence of the variational principle, the HF energy is higher than the exact energy. The lowest energy can be obtained by the HF equation is referred to as the *Hartree Fock limit*. This limit is reached in the limit of a complete basis, see section 2.1.2.

In the restricted Hartree Fock description (RHF), the spatial orbitals are constrained to be identical for the spin up and spin down. A determinant with an even number of electrons where each spatial orbital is doubly occupied, is referred to as a close shell. A singly occupied RHF spatial orbital is referred to as an open shell. In an unrestricted Hartree Fock (UHF) description, the constraint of having identical spatial orbitals for different spins is released.

As the distance between the nuclei is increased towards infinity, the constraint of double occupied spin orbitals is inconsistent with breaking bonds to produce radicals. In order for a RHF determinant to dissociate correctly, an even number of electrons should break into two even-electrons fragments, each being in the lowest electronic state. There are only few covalently bonded systems which obey this requirement. The bad dissociation limit for a RHF wave function has several consequences, high activation energies, short equilibrium bond lengths, large dipole moment. On the other hand, the UHF wave function dissociates correctly but it is not a pure eigenfunction of the total spin operator [33]. Therefore it is not a pure spin state. This attribute is known as *spin contamination*. A UHF lowers the energy by introducing some electron correlation energy [77]. At the same time, it raises the energy by including higher energy spin states.
At some point on a bond-dissociation curve, the behavior of the RHF and UHF wave functions begins to differ. This point is called the RHF/UHF instability point. It is often with UHF, that a false minimum is generated just after the RHF/UHF instability point, on a bond-dissociation curve.

Basis Sets

As it was shown in section 2.1.2, the molecular orbitals (MO)s can be expanded into a set of pre-chosen basis functions (eq. 2.18). In practice, the basis set is limited to a finite set. However, the larger and more improved the basis sets, the greater the flexibility in the expansion in eq. 2.18 of the spin orbitals and the lower the expectation value of the energy. An approach to select the basis functions comes from knowledge to the solution of one-electron atomic orbitals which have the form [33, 78]

$$Y_{lm}(\theta, \varphi)e^{-\zeta r}Z_n(r). \tag{2.22}$$

Here Y_{lm} is the angular spherical harmonic function, $Z_n(r)$ is a polynomial in r, n is the principal quantum number , l is the angular quantum number, m is the magnetic quantum number, θ, φ and r are the spherical coordinates and ζ is the function exponent that determines how compact or diffuse the resulting function is. The previous formula shows that the one-electron atomic orbitals are product of radial term which consists of a decaying exponential in r and polynomial in r ($e^{-\zeta r}Z_n(r)$) and an angular term ($Y_{lm}(\theta,\varphi)$). Slater-type-Functions (STFs) were first used as basis functions [79]. They are characterized by an exponential factor and a monomial in r in their radial part. A Slater-type-Function has the form [33]

$$\eta^{STF}_{lmn,\zeta}(r,\theta,\varphi) = NY_{lm}(\theta,\varphi)r^{n-1}e^{-\zeta r}, \tag{2.23}$$

here N is the normalization constant. STFs are expensive to do multi-center two-electron integrals. Gaussian-type-Functions (GTFs) were introduced to overcome this problem [80]. GTSs can be written in terms of polar or Cartesian coordinates, and in the latter case, it is expressed as [33]

$$\eta^{GTF}_{l_x,l_y,l_z,\gamma}(x,y,z) = Nx^{l_x}y^{l_y}z^{l_z}e^{-\gamma r^2}, \tag{2.24}$$

where the sum of l_x, l_y and l_z determines the type of orbital such as $l = l_x + l_y + l_z$, x, y and z are the Cartesian coordinates and γ is the Gaussian function exponent parallel to ζ in STF. Due to the exponential dependence on r^2, a GTF has a zero slope at the nucleus while a STF has a discontinuous derivative. Thus, a GTF does not represent the proper behavior of the wave function near the nucleus. Another failure of the GTF is that it falls off too rapidly far from the nucleus compared with an STFs, and the tail of the wave function is consequently represented poorly. To achieve a certain accuracy, more GTFs are needed compared with STFs. However, the ease with which the integrals of the GTSs are calculated can compensate for increasing the number of basis functions. The ease with which the integrals are calculated is due to the use of "contractions". A contracted Gaussian basis function (CGF) has the form [33]

$$\eta^{CGF}_{l_xl_yl_z} = \sum_{k=1}^{K} C_k \eta^{GTF}_{l_xl_yl_z,\gamma_{kl}}. \tag{2.25}$$

Here, γ_{kl} and C_k are the contraction exponents and coefficients and K is the length of the contraction. Integrals involving such basis functions are diminished to sums of integrals involving the primitive Gaussian function so the basis function integrals will be calculated rapidly. Most molecular quantum-mechanical methods begin the calculations with the choice of basis sets. The use of proper basis set is an essential condition of the calculation. A minimal basis set is one that has a single basis function for each atomic orbital in its ground-state complete shell. It is the smallest

set that can be used and we cannot expect quantitative precision with such basis. An improvement in minimal basis calculation is achieved by using the STF-KG method, which uses a contraction of K primitive Gaussian functions (GTFs) for each basis function. The contraction coefficients and exponents are chosen so that the basis functions approximate Slater's functions. Increasing the value of K makes the CGFs approach the STF shape. A step forward on improving the basis set is to use a double-zeta basis sets that is obtained by replacing each basis function of a minimal basis set by two basis functions, differ in their orbital exponents (ζ). These two exponents are chosen such that one is slightly above and the other is slightly below the optimum exponent of the minimal basis sets. The SCF procedure will weigh these contributions according to whether the molecular environment required the effective orbital to be expanded or contracted. In the same manner, a triple zeta, quadruple zeta, ...etc. basis sets can be constructed. Since chemical bonding occurs between valence orbitals, it would be reasonable to double the valence orbitals only. Actually, doubling of the core functions would rarely be considered. A split-valence (SV) basis sets uses two basis functions for each valence atomic shell but only one basis function for each inner-shell atomic orbital. Basis sets can be improved also by adding functions of high angular momentum, polarization functions, since atomic orbitals are distorted, or polarized, upon a molecule formation. Such a common set is double-zeta plus polarization set (DZ + P or DZP) which adds, to a double zeta basis, a set of 3d functions on each first and second rows atom, and a set of three 2p functions on each hydrogen atom. An example is 6-31G(d,p) family of basis sets. These basis sets are split-valence polarized basis sets where the inner-shells are expanded into six primitive GTFs and the outer-shells are split into an expansion of three primitive GTFs and another primitive GTF. The contraction scheme for these basis is (11s4p1d/4s1p)/[4s2p1d/2s1p]. For first row atom (H), this contraction scheme leads to a contracted basis set of two s-type functions and one p-type polarization function, i.e. a [2s1p] contracted basis set, coming from a (4s1p) uncontracted basis set. This defines a (4s1p)/[2s1p] contraction. For atoms in the second row, this contraction scheme leads to a contracted basis set of three s-type functions (for 1s inner shell and 2s valence shell), four p-type functions and one d-type polarization function. The d-type function that is added here is a single set of uncontracted 3d primitive Gaussians. For computational convenience there are six 3d functions for each atom ($3d_{xx}$, $3d_{yy}$, $3d_{zz}$, $3d_{xy}$, $3d_{yz}$ and $3d_{zx}$). These six Cartesian Gaussians, are linear combinations of the usual five 3d functions ($3d_{xy}$, $3d_{x^2-y^2}$, $3d_{yz}$, $3d_{zx}$, $3d_{z^2}$) and a 3s function ($x^2 + y^2 + z^2$) [33]. Therefore, the 6-31G(d,p) basis includes one function of s-type symmetry. Thus the [4s2p1d] contracted basis set is coming from (11s4p1d) uncontracted basis set. This defines a (11s4p1d)/[4s2p1d] contraction. More on improving the basis sets, Dunning proposed the correlation consistent (cc) basis sets [81]. These basis sets are designed so that the functions contribute similar amount of correlation en-

ergy are grouped together when considering the mixture of s, p, d, ... etc. basis functions to use. Different sizes of correlation consistent polarized Valence Double/Triple/Quadruple/Quintuple/Sixtuple Zeta basis sets (cc-pVD/T/Q/5/6Z) are available in term of final number of contracted functions. These basis sets can be augmented by adding one diffuse function of each function type in use.

Excited States

The simplest description of an excited state is the orbital picture where one electron has been moved from an occupied to an unoccupied orbital. Excited states having different symmetries may be handled completely analogously to the ground state. A HF wave function may be obtained by a proper specification of the occupied orbitals, and the resulting wave function can be improved by adding electron correlation. Excited states having lower energy solutions of the same symmetry are somewhat more difficult to deal with because it is difficult to generate a HF type wave function for such states, as the variational optimization will collapse to the lowest energy solution of the given symmetry. The lowest level of theory for a qualitative description of excited states is thus a configuration interaction with only singly excited determinants [78]. There are, however, generally also quite low-lying states that essentially correspond to a double excitation, and those require the enclosure of at least the doubles as well as the singly excited determinants. A more balanced description requires multi-configuration self-consistent-field (MCSCF)-based methods where the orbitals are optimized for each particular state, or optimized for a suitable average of the states of interest (state-averaged MCSCF or MCSCF-SA). Such excited state MCSCF solutions correspond to saddle points in the parameter space for the wave function, and second-order optimization techniques are therefore almost compulsory. Excited states involve electrons that are more loosely bound than in the ground state. Thus they usually need basis sets with diffuse functions for a proper description, see section 2.1.2. In the sections 2.1.2 and 2.1.2, we will discuss some of these approaches.

Correlated Methods

The HF method has become a very useful tool for studying stable molecules around their equilibrium geometries. The HF method describes some degree of correlation of electrons with parallel spin that is called the exchange energy. However, electrons with different spins remain uncorrelated. The difference in energy between the HF

total energy and the exact total energy is called the *correlation energy* which lowers the total energy compared to the HF limit.
The correlation energy E_{corr} is defined as the energy difference between the exact energy E_{exact}, which is equivalent to E_e from eq. 2.6 within the bounds of the Born-Oppenheimer approximation, and the Hartree-Fock energy E_{HF}, eq. 2.12,

$$E_{corr} = E_{exact} - E_{HF}. \tag{2.26}$$

This missing energy is negative due to the Hartree-Fock energy defining an upper bound to the energy. Correlation energy can be divided into dynamical and non-dynamical. The dynamical correlation is due to the correlated motion of the electrons while the near-degeneracy or non-dynamical effects can be covered by the use of a few determinants or configurations. Near-degeneracy situations are featured in chemical systems that contain transition metals, excited states or in description of bond-dissociation. Many quantum chemical methods effort to recover this correlation energy by improving upon the Hartree-Fock approximation. Examples are configuration interaction and MCSCF methods which will be discussed in sections2.1.2 and 2.1.2, respectively.

Configuration Interaction A way to account for the correlation energy is to expand the exact electronic wave function in terms of a linear combination of Slater Determinants. When using K spin basis functions, a set of $2K$ spin orbitals can be produced from the HF description. The configuration of the N electrons is such that the lower energy spin orbitals are occupied and the higher energized $2K - N$ virtual orbitals are not, following a basic Aufbau principle.
Hence, a set of 2K spin orbitals that describe a single determinant ground-state wave function for the N electrons, can be produced.

$$\mid \Psi_0\rangle = \mid \chi_1\chi_2 \dots \chi_a\chi_b \dots \chi_N\rangle. \tag{2.27}$$

Many other determinants can be formed from the many different possible excitations of the electrons. Excited determinants can be described with respect to the HF determinant. Didactically, a singly excited determinant [33]

$$\mid \Psi_a^r\rangle = \mid \chi_1\chi_2 \dots \chi_r\chi_b \dots \chi_N\rangle, \tag{2.28}$$

is one in which a single electron is relocated from its occupied spin orbital a to one of the virtual spin orbitals r. And in the same manner a doubly excited determinant can be formed [33]

$$\mid \Psi_{ab}^{rs}\rangle = \mid \chi_1\chi_2 \dots \chi_r\chi_s \dots \chi_N\rangle, \tag{2.29}$$

where two electrons have been relocated from their original positions, a and b, to two virtual spin orbitals, r or s. This procedure continues until all N electrons have been promoted to various virtual states. The number of possible determinants is defined by the binomial coefficient $\binom{2K}{N}$ and are termed according to the number of electrons that have been promoted to virtual orbitals: Hartree-Fock ground state, singly, doubly, triply, ... N-tuply excited states. The full configuration interaction expansion of the ground-state wave function [33]

$$\mid \Psi\rangle = \mid \Psi_0\rangle + \sum_{ar} c_a^r \mid \Psi_a^r\rangle + \sum_{a>b,r>s} c_{ab}^{rs} \mid \Psi_{ab}^{rs}\rangle + \sum_{a>b>c,r>s>t} c_{abc}^{rst} \mid \Psi_{abc}^{rst}\rangle + \dots \quad (2.30)$$

is a sum of the unique possible configurations, organized above in terms of the N-electron determinants, and is exact for a given basis set. For large molecules a full configuration interaction calculation is computationally impossible. Therefore, the configuration interaction calculation is truncated. The most common truncation is configuration interaction with singly and doubly excitations, a (CISD) calculation [82, 83]. For large molecules a CISD calculation is not sufficient in describing the correlation energy and the calculations can incorporate further triplet and quadruplet excitations, again at the cost of computational effort. An extra flexibility in the goal of retrieving the correlation energy is obtained by allowing for the optimization of the molecular orbital coefficients and accounts for what is termed static or "near-degeneracy" correlation. This is the essence of the MCSCF method, section 2.1.2.

Multi-Configuration Self-Consistent-Field Methods A Multi-Reference Self-Consistent-Field method is an extension of single determinant methods. The MCSCF method can be considered as a configuration interaction where not only the coefficients in front of the determinants (eq. 2.30) are optimized by the variational principle, but the MOs used for constructing the determinants are also optimized. The MCSCF optimization is iterative like the SCF procedure (if the multi configuration is only one, it is simply HF). Since the number of MCSCF iterations required for achieving convergence tends to increase with the number of configurations included, the size of MCSCF wave functions that can be treated is somewhat smaller than for CI methods. The MCSCF wave function $|\Psi^{MCSCF}\rangle$ is a truncated configuration interaction expansion given by [78]

$$|\Psi^{MCSCF}\rangle = \sum_k C_k |\Psi_k\rangle, \quad (2.31)$$

where C_k is the configuration interaction expansion coefficient of the CSF Ψ_k. Each state function is composed of a set of molecular orbitals occupied by an α or β

spin electrons. In MCSCF, all coefficients C_{ij} in eq. 2.18 and the molecular orbital coefficients C_k for the atomic orbitals are optimized simultaneously. The MCSCF method is based on the variational principle, in which the energy is minimized by varying the C_k and orbital coefficients:

$$E^{MCSCF} = \frac{\langle \Psi^{MCSCF} \mid \hat{H} \mid \Psi^{MCSCF} \rangle}{\langle \Psi^{MCSCF} \mid \Psi^{MCSCF} \rangle}. \tag{2.32}$$

Here, E_{MCSCF} is expectation value of the $|\Psi^{MCSCF}\rangle$ wave function. The CSFs entering an MCSCF expansion are pure spin states, hence, MCSCF wave functions do not suffer from the problem of spin contamination. When deriving the HF equations only the variation of the energy with respect to an orbital variation was required to be zero, which is equivalent to the first derivative of the energy with respect to the MO expansion coefficients being equal to zero. MCSCF wave functions, are harder to converge than HF wave functions. Furthermore, there is no guarantee that the solution found by the SCF procedure is a minimum of the energy as a function of the MO coefficients. Therefore, MCSCF wave function optimizations are normally carried out by expanding the energy to second order in the variational parameters (orbital and configurational coefficients). To ensure that a minimum has been found, the matrix of second derivatives of the energy with respect to the MO coefficients can be calculated and diagonalized, with a minimum having only positive eigenvalues. The major problem with MCSCF methods is selecting which configurations are necessary to include for the property of interest.

Complete Active Space Self-consistent Field (CASSCF) One of the most popular approaches, to select which configurations are necessary to include, is the Complete Active Space Self-Consistent Field (CASSCF) method developed by Roos et al. [84]. In this method, the selection of configurations is done by partitioning the MOs into active and inactive ones. The active MOs will typically be some of the highest occupied and the lowest unoccupied MOs from a HF calculation as it is shown in Figure 2.1. The inactive MOs are doubly occupied or empty. Within the active MOs a full configuration interaction calculation is performed and all the proper CSFs are included in the MCSCF optimization. The MOs to include in the active space must be decided manually by considering the problem at hand and the computational expense. If several points on the PES are desired, the MCSCF active space should include all those orbitals that change along the PES considerably, or for which the electron correlation is likely to change. A common notation is CASSCF(n,m), which indicates that n electrons are distributed in all possible ways in m orbitals. CASSCF is a full configuration interaction calculation within the restricted complete active space. In this way, an active space defines the region

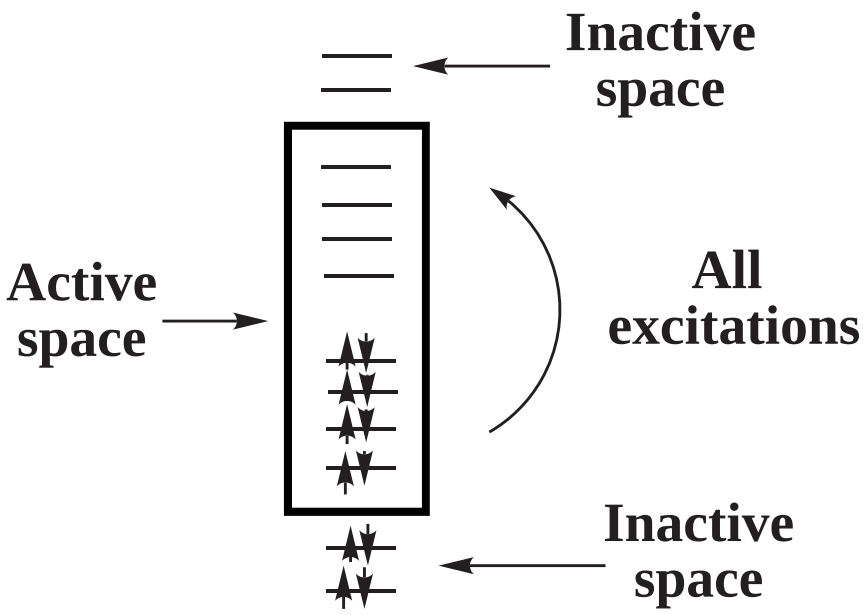

Figure 2.1: All the possible excitations within the active space define the configurations in a CASSCF calculation.

in which the electrons can form all configurations. Although this method reduces the effort of picking the CSFs, it is still not a black box. The proper orbitals that represent the molecular system and its properties must be selected by hand. There are few rules of thumb that may be of help in selecting an appropriate set of orbitals for the active space: (1) For each occupied orbital, there will be usually one corresponding virtual orbital. (2) Including all the valence orbitals, i.e. the space covered by a minimum basis set, leads to a wave function that can correctly describe all dissociation pathways. Unfortunately, a full valence CASSCF wave function rapidly becomes unmanageably large for realistic sized systems. (3) The orbital energies from an RHF calculation may be used for selecting the important orbitals. The highest occupied and lowest unoccupied are usually the most important orbitals to include in the active space since the smaller the orbital energy difference, the larger contribution to the correlation energy. (4) Using the concept of natural orbitals that diagonalize the density matrix so that the eigenvalues are the occupation numbers. Orbitals with occupation numbers significantly different from 0 or 2 (for a closed shell system) are usually those that are the most important to include in the active space.

A state average CASSCF (SA-CASSCF) calculation is used to obtain several

electronic excited states simultaneously for a given symmetry and spin, by minimizing the weighted sum of their energies. A drawback to the SA-CASSCF method is that the quality of any one state's wave function is lower than it will be if only one state is considered (CASSCF without state averaging). On the other hand, a virtue of a SA-CASSCF is that all states are expressed using the same MOs, thereby ensuring orthogonality (which is critical if, for example, transition dipoles between states are desired to be computed).

Non-dynamical or static correlation energy reflects the inadequacy of a single reference in describing a given molecular state, and is due to nearly degenerate states or rearrangement of electrons within partially filled shells. The MCSCF method is good for obtaining the static correlation by allowing for partially occupied orbitals and describes well values at dissociation.

In the research carried out in this thesis, the SA-CASSCF/cc-pVDZ level of theory was employed for the 4MCF [85] (Chapter 4) and CPDHP (Chapter 5) [86] systems while the CASSCF/cc-pVDZ level of theory was employed for the fulvene system [63, 87] (Chapter 3).

Solvation Effects

An important aspect of computational chemistry is to evaluate the effect of the environment, such as a solvent. Methods for evaluating the solvent effect may broadly be divided into two types: those describing the individual solvent molecules and those that treat the solvent as a continuous medium [88, 89, 90]. Combinations are also possible, for example by explicitly considering the first solvation shell and treating the rest by a continuum model. Solvation effects can be partitioned into two main groups depending on the type of property used to describe the solvent effect:

- Non-specific (long-range) solvation
  - Polarization
  - Dipole orientation
- Specific (short–range) solvation
  - Hydrogen bonds
  - van der Waals interactions

– Solvent shell structure
– Solvent-solute dynamics
– Charge transfer effects
– Hydrophobic effects (entropy effects).

The non-specific effects are primarily solvent polarization and orientation of the solvent electric multipole moments by the solute, where the most important effect is usually the dipole interaction. These effects cause a screening of charge interactions leading to the macroscopic dielectric constant being larger than 1. The microscopic interactions are primarily located in the first solvation shell, although the second solvation shell may also be important for multiple-charged ions. The microscopic interactions depend on the specific nature of the solvent molecule, such as the shape and the ability to form hydrogen bonds. In this study we employ the continuum solvation models discussed below.

Continuum Solvation Models. Continuum models [91] consider the solvent as a uniform polarizable medium with a dielectric constant ε, and with the solute M placed in a suitably shaped hole in the medium (see Figure 2.2) [92].

Creation of a hole in the medium costs energy (destabilization) while dispersion

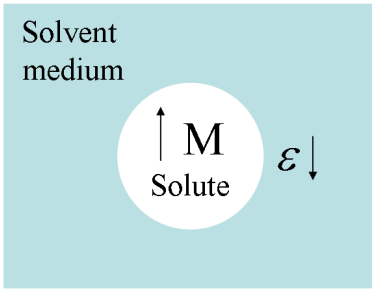

Figure 2.2: Reaction field model. The arrows indicate the solvent dipole moment induced by the solute.

interactions between the solvent and solute add a stabilization (approximately, this is the van der Waals energy between solvent and solute). In principle, there may be a repulsive component too, so the dispersion term is sometimes denoted dispersion/repulsion. The electric charge distribution of M will polarize the medium

(induce charge moments), which in turn acts back on the molecule and produce an electrostatic stabilization. Hence, the solvation (free) energy may be written as

$$\Delta G_{solvation} = \Delta G_{cavity} + \Delta G_{dispersion} + \Delta G_{electronic}, \tag{2.33}$$

where, $G_{solvation}$, ΔG_{cavity}, $\Delta G_{dispersion}$ and $\Delta G_{electronic}$ are the solvation, cavity, dispersion and electronic free energies, respectively. The influence between a molecule in solution (the solute) and its surrounding medium (the solvent) can most simply be described using the reaction field model. The basic assumption made in this model is that the solute is placed in a spherical cavity inside the solvent. The latter is described as a homogeneous, polarizable medium of constant dielectric constant. The solute dipole moment induces a dipole moment of opposite direction in the surrounding medium. Polarization of the medium in turn polarizes the charge distribution in the solvent. Treating this mutual polarization in a self consistent manner leads to the Onsager reaction field model. Reaction field models differ in five aspects:

1. How the size and shape of the hole are defined.
2. How the cavity/dispersion contribution is calculated.
3. How the charge distribution of M is represented.
4. How the solute M is described, either classical (force field) or quantum (semiempirical or ab initio).
5. How the dielectric medium is described.

The dielectric medium is normally taken to have a constant value of ε which is the only parameter characterizing the solvent. In other words, solvents having the same ε value (such as acetone, $\varepsilon = 20.7$, and 1-propanol, $\varepsilon = 20.1$, or benzene, $\varepsilon = 2.28$, and carbon tetrachloride, $\varepsilon = 2.24$) are thus treated equally. The simplest shape for the hole is a sphere or an ellipsoid. This has the advantage that the electrostatic interaction between M and the dielectric medium may be calculated analytically. Taking the atomic radius as a suitable factor (the cavity radius typical value is 1.2 $\mathring{A}$) multiplied by a van der Waals radius defines a van der Waals surface. Such a surface may have small pockets where no solvent molecules can enter and a more appropriate description may be defined as the surface detected by a spherical particle of a given radius (a typical radius of 1.4 $\mathring{A}$ to model a water molecule) rolling on the van der Waals surface. This is denoted as the Solvent Accessible Surface (SAS), and it is illustrated in Figure 2.3. Since an SAS is computationally more expensive

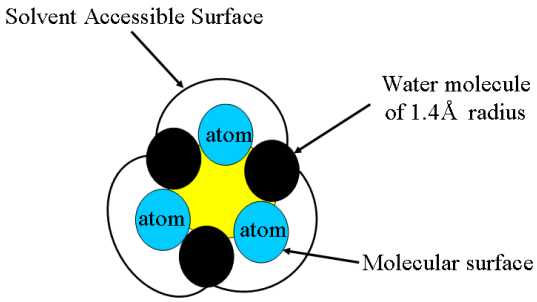

Figure 2.3: On a surface generated by overlapping van der Waals spheres there will be areas (marked in yellow) that are inaccessible to a solvent molecule (Solvent surface area). The blue spheres indicate the solute atoms and the black spheres indicate the water molecules rolling on the van der Waals surface.

than a van der Waals surface, and since the difference in accuracy is often small, a van der Waals surface is often used in practice. The energy required to create the cavity (entropy factors and loss of solvent-solvent van der Waals interactions), and the stabilization due to van der Waals interactions between the solute and solvent (which may also contain a small repulsive component), is usually assumed to be proportional to the surface area. The corresponding energy terms may be taken simply as being proportional to the total SAS area (a single proportionality constant), or parameterized by constants specific for each atom type with such parameters being determined by fitting to experimental solvation data. The electrostatic component of eq. 2.33 can be described at several different levels of approximation. In this thesis we use the Self-consistent reaction field (SCRF) model [93, 94]. In such a model, a classical description of the molecule M in Figure 2.2 can be a force field with partial atomic charges, while a quantum description involves calculation of the electronic wave function. The latter may be either with a semi-empirical model, such as AM1 [95] or PM3 [96], or with more sophisticated electronic structure methods, i.e. HF, DFT, MCSCF, etc. When a quantum description of M is employed, the calculated electric moments induce charges in the dielectric medium, which acts back on the molecule, causing the wave function to respond and therefore changing the electric moments, etc. Thus, the interaction with the solvent model must be calculated by an iterative procedure, leading to various SCRF models. The dipole in a spherical cavity is known as the Onsager model [93] which for a dipole moment of μ, leads to an energy stabilization given by [78] (using the international system of units)

$$\Delta G_{electronic} = -\frac{1}{2(4\pi\epsilon_0)}\hat{R}_F\mu, \tag{2.34}$$

where $\hat{R}_F$ is the reaction field operator which is proportional to the solute dipole moment [93, 97]:

$$\hat{R}_F = g\mu, \tag{2.35}$$

where g is the Onsager factor which gives the strength of the reaction field and depends upon the dielectric constant of the medium ε and the radius of the spherical cavity a:

$$g = \frac{2(\varepsilon - 1)}{(2\varepsilon + 1)a^3}. \tag{2.36}$$

Accordingly, eq. 2.34 can be written as [78]:

$$\Delta G_{electronic} = -\frac{\varepsilon - 1}{4\pi\epsilon_0(2\varepsilon + 1)}\frac{\mu^2}{a^3}. \tag{2.37}$$

The Onsager model represents the interaction energy of a solute in a spherical cavity embedded in a continuum dielectric by permitting the dipole of the solute to induce a dipole within the dielectric. The induced dipole in turn influences the dipole of the solute, so these dipoles are iterated to self-consistency. For spherical or ellipsoidal cavities this equation can be solved analytically, but for molecular shaped surfaces it must be done numerically.

In the quantum mechanical approach, the solvent effect is taken as an additional term in the Hamiltonian of the isolated molecule (solute) obtained from the system energy (assuming only a dipole interaction) [98]. At the HF level of theory, the $\hat{R}_F$ operator corresponds to the addition of an extra term to the Fock matrix elements [99] (written in atomic units)

$$\hat{f}_{ij} = \langle \chi_i \mid \hat{f} \mid \chi_j \rangle - \sigma g \mu \langle \chi_i \mid \mu \mid \chi_j \rangle, \tag{2.38}$$

or

$$\hat{f}_{ij} = \langle \chi_i \mid \hat{f} \mid \chi_j \rangle - \sigma g \langle \chi_i \mid \mu \mid \chi_j \rangle^2. \tag{2.39}$$

The parameter σ depends on the constraints of the variation. If normality of the wave function is the only constraint ($\langle \chi \mid \chi \rangle = 1$), then $\sigma = 1$.

In connection with electronic structure methods (i.e. a quantum description of M), the term SCRF is quite generic and it does not by itself indicate a specific model. Typically, however, the term is used for models where the cavity is either spherical or ellipsoidal, the charge distribution is represented as a multipole expansion, often terminated at quite low orders (for example only including the charge and dipole terms), and the cavity/dispersion contributions are neglected. Such a treatment can only be used for a qualitative estimate of the solvent effect, although relative values may be reasonably accurate if the molecules are polar (dominance of the

dipole electrostatic term) and sufficiently similar in size and shape (cancelation of the cavity/dispersion terms). Unfortunately, there is no consensus on how to choose the cavity radius. In some cases, the molecular volume is calculated from the experimental density of the solvent and the cavity radius is defined by equating the cavity volume to the molecular volume. Alternatively, the cavity size may be derived from the experimental dielectric constant and the calculated dipole moment and polarizability [100]. In any case, the main assumption of these models is that the molecule is roughly spherical or ellipsoidal which is only generally true for small compact molecules. More sophisticated models employ molecular shaped cavities [78]. The cavity is often defined based on van der Waals radii of the atoms in the molecule multiplied with an empirical scale factor. Alternatively, the molecular volume may be calculated directly from the electronic wave function. In this thesis we have investigated the effect of the solvent approximated using the SCRF theory in the framework of the Kirkwood and Onsager [93, 94] model for the CPDHP system [86] (Chapter 5). The electrostatic free energy calculations were carried out using the GAMESS [101] program suite using the cavity radius of calculated using the standard GAUSSIAN procedure [102].

2.2 Breakdown of the Born-Oppenheimer Approximation, Avoided Crossings and Conical Intersections

The Born-Oppenheimer approximation, discussed in section 2.1.1, is the keystone to the visualization of chemical processes. However, whereas the Born-Oppenheimer approximation is valid for the majority of chemical systems there are many important cases where the approximation breaks down [50, 57].

In such cases, the nuclear and electronic motions are coupled. This is very common in photochemistry. An important example of coupling between the nuclei and electrons, named vibronic coupling, is a conical intersection (CI) between at least two electronic states (see Figure 2.4). CIs offer a pathway for ultra-fast relaxation on the femtosecond time scale and have therefore important consequences for the dynamics of chemical reactions. A CI permits efficient non-adiabatic transitions between PESs.

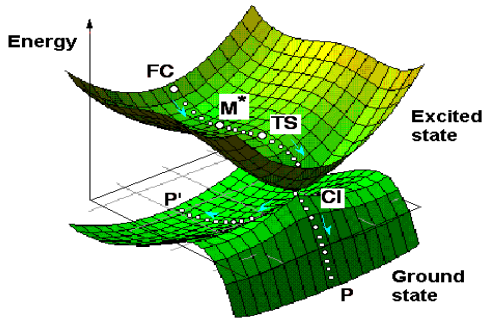

Figure 2.4: Ground and excited state potential energy surfaces touching at the conical intersection (CI). The minimum energy path connects the Franck-Condon (FC) point to the photo–products P and P'. M* is the excited state intermediate and TS is a transition state connecting M* to the CI.

2.2.1 Non-Adiabatic Coupling Matrix Terms (NACT)

For non Born-Oppenheimer process, more than one electronic state is important in the overall dynamics. To solve the Schrödinger equation for the total Hamiltonian describing the electronic plus nuclear motion in a certain system, the total wave function $|\Psi\rangle$ is expanded in the basis of i electronic states, see eq. 2.5. As it was stated in eq. 2.5, the total wave function consists of the electronic and nuclear parts, therefore:

$$\hat{H}|\Psi(r,R)\rangle = E_{tot}\sum_{e}|\Psi_e(r;R)\Psi_{eN}(R)\rangle, \tag{2.40}$$

where $\hat{H}$ in eq. 2.40 includes the kinetic nuclear energy as well as the nuclear repulsion, i.e.,

$$\hat{H} = \hat{T}_N + \hat{H}_e + \hat{V}_N, \tag{2.41}$$

where

$$\hat{T}_N = \sum_{A=1}^{M}\frac{-1}{2M_A}\nabla_A^2, \tag{2.42}$$

and E_{tot} is the total energy defined in eq. 2.8 and the operator ∇_A is a three-dimensional derivative with respect to nuclear coordinates. Applying the operator

∇_A^2 on the wave function $\Psi(r,R) = \Psi_e(r;R)\Psi_{eN}(R)$, gives

$$\nabla_A^2 \left[\Psi_e(r;R)\Psi_{eN}(R)\right] = \nabla_A \nabla_A \left[\Psi_e(r;R)\Psi_{eN}(R)\right], \quad (2.43)$$

$$= \nabla_A \left[\nabla_A \Psi_e(r;R)\Psi_{eN}(R)\right], \quad (2.44)$$

$$= \Psi_e(r;R)\ \nabla_A^2 \Psi_{eN}(R) + \Psi_{eN}(R)\ \nabla_A^2 \Psi_e(r;R) + 2\nabla_A \Psi_{eN}(R)\ \nabla_A \Psi_e(r;R). \quad (2.45)$$

By expanding the multi-state wave function $|\Psi(r,R)\rangle$ in terms of the electronic basis i, where the index e is replaced with i ($e \equiv i$):

$$|\Psi(r,R)\rangle = \sum_i \Psi_i(r;R)\Psi_{iN}(R), \quad (2.46)$$

and by inserting eq. 2.46 into eq. 2.1, projecting from the left by $\langle\Psi_j(r,R)|$ and integrating over the electronic coordinates leads to the set of coupled equations

$$\sum_i \hat{H}_{ji}(R)|\Psi_{iN}\rangle = \sum_i [\hat{T}_N + E_i(R) + \hat{V}_N(R)\delta_{ji} + \sum_A \frac{-1}{2M_A}\left[2T_{ji}^{(1)}\ \cdot \nabla_A\right] + \sum_A \frac{-1}{2M_A} T_{ji}^{(2)}]|\Psi_{iN}(R)\rangle. \quad (2.47)$$

In this coupled equation, E_i is the electronic energy for electronic state i obtained from solving the electronic Hamiltonian, and

$$T_{ji}^{(1)} = \langle \Psi_j \mid \nabla_A \Psi_i \rangle, \quad (2.48)$$

$$T_{ji}^{(2)} = \langle \Psi_j \mid \nabla_A^2 \Psi_i \rangle. \quad (2.49)$$

$T_{ji}^{(1)}$ and $T_{ji}^{(2)}$ represent non-adiabatic couplings of first and second order, respectively, between wave functions of different electronic states. Note that $T_{ji}^{(1)}$ is a vector while $T_{ji}^{(2)}$ is scalar. Since the electronic wave functions are normalized to the same value at all nuclear geometries,

$$\langle \Psi_j \mid \Psi_i \rangle = \delta_{ji}, \quad (2.50)$$

it follows that the matrix $T_{ji}^{(1)}$ is anti-Hermitian, that is

$$T_{ji}^{(1)} = -T_{ji}^{(1)^*}. \quad (2.51)$$

Eq. 2.47 can be rewritten as

$$[\hat{T}_N + \hat{V}_N(R)\delta_{ji} - E_j]\,|\Psi(R)_{jN}\rangle = \sum_i \Lambda_{ji}|\,\Psi(R)_{iN}\rangle, \quad (2.52)$$

where Λ_{ji} is the nonadiabatic coupling matrix:

$$\Lambda_{ji} = -\langle \Psi_j \mid T_N \mid \Psi_i \rangle + \sum_A \frac{-1}{2M_A} \langle \Psi_j \mid \nabla_A \mid \Psi_i \rangle \nabla_A. \tag{2.53}$$

The Born-Oppenheimer approximation discussed in section 2.1.1, involves assuming a value of zero for the non-adiabatic coupling terms (NACTs) Λ_{ji}. An approach to calculate the NACTS is discussed in the section 2.2.2.
Under that assumption, the nuclear and electronic wave functions are separable. However, spontaneous changes in electronic states, i.e. surface-to-surface crossing, are not permitted. Any model addressing such state-to-state crossing, must instead start from eq. 2.52. In the region of an avoided crossing or CIs, the adiabatic states change their character significantly, therefore, mixing between different states is the largest. As a consequence, one has to take into account simultaneous motion on several potential energy surfaces and the coupling elements between them. This is a difficult task since the calculation of the kinetic coupling elements will involve several nuclear degrees of freedom and the electronic Hamiltonian operator is not diagonal.

From now on, the results $|\Psi_i\rangle$ of the TISE, see eq. 2.47, will be called "adiabatic". A "diabatic" transformation of the adiabatic states replaces these off-diagonal kinetic energy terms by potential energy terms. A comparison between adiabatic and diabatic representations is discussed in the following section, 2.2.2. Sometimes, a diabatic transformation of the adiabatic states is called the adiabatic to diabatic transformation or diabatization which is discussed in section 2.2.2.

2.2.2 Adiabatic and Diabatic Representations

Direct solution of the Schrödinger equation with the total molecular Hamiltonian to study the motion of molecules is called quantum molecular dynamics. At some initial time a quantum mechanical system has an energy determined by the initial sate (and the Hamiltonian). Changing conditions modify the Hamiltonian as a function of time resulting in a final Hamiltonian at some later time. The system will evolve according to the time-dependent Schrödinger equation, to reach a final state (see section 2.4). In adiabatic dynamics, interatomic interactions are represented by single PESs (Born-Oppenheimer approximation). Non-adiabatic dynamics consists of taking the interaction between several coupled PESs corresponding to different electronic quantum states of the molecule. The coupling terms are called vibronic couplings or NACTs, see section 2.2.1. Vibronic coupling is large in the case of two

adiabatic PESs coming close to each other. This usually happens in the neighborhood of an avoided crossing of potential energy surfaces corresponding to distinct electronic states of the same spatial and spin symmetry. In this case the adiabatic or Born–Oppenheimer approximation fails and non-adiabatic terms (or the vibronic coupling terms) have to be taken into account.
The physical interpretation of the adiabatic representation is straightforward since the potentials and transition dipole moments are computed for fixed positions of the nuclei using approximate methods for the solution of the electronic Theory [103]. The kinetic couplings are only large around avoided crossings which mark the breakdown of the Born-Oppenheimer approximation which applies a strict separation of the electron and nuclear motion. In the diabatic case, the potentials and consequently the excitation energies differ from the adiabatic ones. Therefore, it is not clear how the diabatic excitation energies can be interpreted.

Nevertheless, the use of the potential couplings in the diabatic representation is inevitable in all cases where the kinetic couplings are very sharply peaked around avoided crossings causing numerical difficulties. These computational problems of the adiabatic representation can be avoided by transforming into the diabatic basis, where the kinetic couplings are replaced by potential coupling functions which are usually smooth [104].

Diabatization Scheme

The non-adiabatic or *diabatic* states, Ψ_i^d, are obtained from the adiabatic Ψ_i^{ad} ones by unitary transformation. For a two dimensional system with two crossing electronic states, the unitary transformation matrix $U(R)$ is given by [105]:

$$U(R) = \begin{pmatrix} \cos\alpha(R) & \sin\alpha(R) \\ -\sin\alpha(R) & \cos\alpha(R) \end{pmatrix}. \tag{2.54}$$

Here $\alpha(R)$ is the mixing angle between the states at the nuclear coordinates (R). In principle, this mixing can be obtained by integration of the non-adiabatic coupling matrix (NACM) elements, where [105]

$$\frac{\partial \alpha_{ij}}{\partial R} = \langle \Psi_i^{ad} \mid \frac{\partial}{\partial R} \mid \Psi_j^{ad} \rangle, \tag{2.55}$$

or

$$\alpha_{ij}(R) = \int \langle \Psi_i^{ad} \mid \frac{\partial}{\partial R} \mid \Psi_j^{ad} \rangle dR. \tag{2.56}$$

For two states system, the adiabatic Hamiltonian $\hat{H}^{ad}$ can be given by:

$$\hat{H}^{ad} = \begin{pmatrix} T_N & \Lambda_{ij} \\ \Lambda_{ji} & T_N \end{pmatrix} + \begin{pmatrix} V_i & 0 \\ 0 & V_j \end{pmatrix}. \tag{2.57}$$

The adiabatic Hamiltonian is transformed to a diabatic one H^d via a unitary transformation $U(R)$ defined in eq. 2.54:

$$H^d = U(R) H^{ad} U(R)^\dagger. \tag{2.58}$$

The transformation shall be such that

$$U(R) \begin{pmatrix} T_N & \Lambda_{ij} \\ \Lambda_{ji} & T_N \end{pmatrix} U(R)^\dagger \approx \begin{pmatrix} T_N & 0 \\ 0 & T_N \end{pmatrix} \tag{2.59}$$

and

$$U(R) \begin{pmatrix} V_i & 0 \\ 0 & V_j \end{pmatrix} U(R)^\dagger = \begin{pmatrix} W_{ii} & W_{ij} \\ W_{ji} & W_{jj} \end{pmatrix}. \tag{2.60}$$

Where W_{ii} and W_{jj} refer to the diabatic potentials of diabatic states i and j, respectively. W_{ij} refers to the diabatic coupling element. Thus, the diabatic Hamiltonian can be expressed as:

$$H^d = \begin{pmatrix} T_N & 0 \\ 0 & T_N \end{pmatrix} + \begin{pmatrix} W_{ii} & W_{ij} \\ W_{ji} & W_{jj} \end{pmatrix}. \tag{2.61}$$

The wave functions in the diabatic basis are obtained by:

$$\begin{pmatrix} \Psi_i^d \\ \Psi_j^d \end{pmatrix} = U(R) \begin{pmatrix} \Psi_i^{ad} \\ \Psi_j^{ad} \end{pmatrix}. \tag{2.62}$$

Off-diagonal elements in adiabatic equations 2.57 are nuclear kinetic energy terms. In eq. 2.61, the off-diagonal elements are potential terms. The diabatic potentials (W_{ij}) should be smooth so that the diabatic electronic wave functions change slowly along the avoided crossing and should converge to the adiabatic ones outside of the crossing area. Otherwise, a considerable coupling is obtained far from the crossing.

Pure diabatic states can only be obtained for diatomic systems but for polyatomic molecules, one searches for "quasi-diabatic" (or approximately diabatic) states with potential coupling. In this vein, a number of approximate schemes have been suggested which typically do not require the computation of all derivative couplings but rather aim at suitable properties to vary smoothly with the nuclear coordinates [106, 107, 108, 109]. In this thesis we used two approaches to calculate the NACTs.

In one of these approaches, the adiabatic states are approximately diabatized by minimizing the change of orbitals as well as the configuration interactions vectors (in SA-CASSCF calculations) as a function of the geometry [105]. This approach is discussed in section 2.2.2 and has been employed to calculate the NACTs for the 4MCF system (Chapter 4) as it is implemented in the MOLPRO software [52]. Another scheme that focusses on the singular derivative couplings alone, and utilize a linear coupling-diabatic potential matrix to define the adiabatic-diabatic transformation angle [110], has been employed for the fulvene system and is discussed in section 3.3 (Chapter 3). The idea of such method is to remove only the leading derivative coupling elements from the adiabatic basis (those which diverge at s CI) and the other coupling terms are neglected. The diverging coupling terms are removable by transforming to a suitable electronic basis. Such linear coupling approach is applied to the transformation angle only and not to the PESs themselves.

Calculation of Non-Adiabatic Coupling Matrix Elements

In this section, we introduce an approach to calculate the NACM elements (NACMEs) using the expansion coefficients of the configuration interaction wave function (configuration interaction vector). To achieve this purpose, one can use an approximation based on the analysis of the configuration interaction vectors [105]. The basic assumption in this method is that the configuration interaction vectors representing the diabatic states are approximately geometry independent, which implies that the change of the CASSCF orbitals as a function of geometry can be neglected. Using this method [105], the NACTs for CASSCF or configuration interaction wave functions can be compute for SA-CASSCF wave functions. The configuration interaction wave function, see eq. 2.31, of electronic state i can be expressed as

$$|\Psi_i^{MCSCF}\rangle = \sum_k C_{ik}|\Psi_k\rangle, \tag{2.63}$$

where the index i in $|\Psi_i^{MCSCF}\rangle$ and C_{ik} refers to electronic state i. Thus, eq. 2.48 can be written as:

$$\langle \Psi_j^{ad} \mid \frac{\partial}{\partial R} \mid \Psi_i^{ad} \rangle = \langle \sum_l C_{jl} \Psi_l^{ad} \mid \frac{\partial}{\partial R} \mid \sum_k C_{ik} \Psi_k^{ad} \rangle \quad (2.64)$$

$$= \sum_l \sum_k C_{jl} \left(\frac{\partial}{\partial R} C_{ik} \right) \underbrace{\langle \Psi_l^{ad} \mid \Psi_k^{ad} \rangle}_{\delta_{lk}} + \sum_l \sum_k C_{jl} C_{ik} \langle \Psi_l^{ad} \mid \frac{\partial}{\partial R} \mid \Psi_k^{ad} \rangle \quad (2.65)$$

$$= \underbrace{\sum_l C_{jl} \left(\frac{\partial}{\partial R} C_{il} \right)}_{C_{ji}-term} + \underbrace{\sum_l \sum_k C_{jl} C_{ik} \langle \Psi_l^{ad} \mid \frac{\partial}{\partial R} \mid \Psi_k^{ad} \rangle}_{MO_{ij}-term} \quad (2.66)$$

In eq. 2.66, the C_{ji}–term involves differentiation of the configuration interaction coefficients and the MO_{ij}–term contains derivatives of configurations or determinants [111]. The MO_{ij}–term leads to integrals of atomic orbitals, see eq.s 2.27 and 2.28.

Using the invariance of the CASSCF and multi reference configuration interaction energies with respect to unitary transformations, diabatic CASSCF orbitals can be generated by maximizing the overlap of CASSCF orbitals at a displaced geometry R' with the orbitals at the reference geometry R (Recalling that the configuration interaction vectors representing the diabatic states are approximately geometry independent). Consequently, the relative contributions of the orbitals and configuration interaction to the matrix elements of $T_{ji}^{(1)}$are modified: The MO_{ij}–term is minimized, and to a very good approximation the matrix elements of $T_{ji}^{(1)}$ could be obtained from the configuration interaction vectors (C_{kl}-term) alone. This can be achieved by maximizing the overlap of the active CASSCF orbitals with those of a reference geometry R, at which the wave functions are assumed to be diabatic.

The NACTS for the CASSCF wave function can be computed using the finite differences method [112]. In this procedure, one has to compute and store the wave functions at two (first-order algorithm) or three (second-order algorithm) slightly displaced geometries. First, the wave function is calculated at the reference geometry. Then it is calculated at the (positively) displaced geometry. This can be repeated at a (negatively) displaced geometry if the second-order (three-point) method is used. Then, the transition densities matrix computed from the configuration interaction vectors, at R and $R' = R \pm \Delta R$ between the states, is calculated:

$$\langle \Psi_i^d \mid \frac{\partial}{\partial R} \mid \Psi_j^d \rangle_R \simeq \frac{1}{2\Delta R} \langle \Psi_i^d (R + \Delta R) \mid \Psi_j^d (R - \Delta R) \rangle, \quad (2.67)$$

where ΔR is the small increment. The transformation matrix of the configuration interaction vectors between R and R', is chosen such that non-adiabatic coupling matrix elements $\langle \Psi_j^d \mid \frac{\partial}{\partial R} \mid \Psi_j^d \rangle$ are minimized for all the internal coordinates.

2.3 Solution of the Nuclear TISE

Having discussed some common methods for solving the electronic problem, we will now discuss the nuclear problem, see eq. 2.9. Recalling that the eigenvalues of the nuclear Hamiltonian are total energies, composed of both electronic and nuclear contributions; the nuclear eigenfunctions are functions of the nuclear coordinates which also serve as parametric variables of the electronic function (see section 2.1.1).

2.3.1 Fourier-Grid-Hamiltonian Method

After solving the electronic Schrödinger equation for different molecular geometries and constructing the PESs, the time independent nuclear Schrödinger equation must be solved for each electronic state i. The nuclear Schrödinger equation describes all degrees of freedom of the molecule: translations, rotations and vibrations. By changing the coordinate system from laboratory fixed coordinates to center of mass fixed coordinates the translational motion may be separated from the other degrees of freedom

$$\mid \Psi_N^i\rangle = \mid \Psi_{trans}^i\rangle \times \mid \Psi_\nu^i\rangle. \tag{2.68}$$

Hence, the solution of the nuclear Schrödinger equation in terms of internal coordinates is [113]

$$\hat{H} \mid \Psi_\nu^i\rangle = (\hat{T} + \hat{V}_i) \mid \Psi_\nu^i\rangle = E_i^\nu \mid \Psi_\nu^i\rangle. \tag{2.69}$$

This solution gives rotational-vibrational (rovibrational) eigenfunctions $\mid \Psi_\nu^i\rangle$ and eigenenergies E_ν^i of the nuclear framework. These eigenfunctions can be considered as an initial state for quantum dynamical calculations that solves the time-dependent nuclear Schrödinger equation. A numerical method called the Fourier Grid Hamiltonian (FGH) method is applied to solve the time-dependent nuclear Schrödinger equation [114, 115]. This method employs the vibrational Hamiltonian in generalized (internal) coordinates within a grid representation. The FGH method uses the fact that the kinetic energy operator $\hat{T}$ is diagonal in momentum space while the potential energy operator $\hat{V}$ is diagonal in position space. The Fourier transformation is used to transform the wave function from position space to momentum space and vice versa. In one dimensional motion of a single particle, the Hamiltonian $\hat{H}$ of a single particle of mass m and momentum $\hat{p}$ within a potential $V(\hat{x})$ is given by

$$\hat{H} = \hat{T} + V(\hat{x}) = \frac{\hat{p}^2}{2m} + V(\hat{x}). \tag{2.70}$$

Two basis sets are chosen in which the Hamilton operator can be represented to span a subspace of the Hilbert space. In position space the basis vectors are the

eigenvectors of the position operator $\hat{x}$

$$\hat{x} \mid x\rangle = x \mid x\rangle, \tag{2.71}$$

where the eigenvectors form an orthonormal basis so they satisfy:

$$\langle x \mid x'\rangle = \delta(x - x'), \tag{2.72}$$

$$\hat{I}_x = \int_{-\infty}^{\infty} dx \mid x\rangle\langle x \mid . \tag{2.73}$$

Therefore, the potential V is diagonal in position space

$$\langle x' \mid V(\hat{x}) \mid x\rangle = V(x)\delta(x - x'). \tag{2.74}$$

In momentum space the basis vectors are the eigen vectors of the momentum operator

$$\hat{p} \mid k\rangle = k\hbar \mid k\rangle, \tag{2.75}$$

which also form a complete orthonormal basis set

$$\langle k \mid k'\rangle = \delta(k - k'), \tag{2.76}$$

$$\hat{I}_k = \int_{-\infty}^{\infty} dk \mid k\rangle\langle k \mid . \tag{2.77}$$

In momentum space the kinetic energy operator is diagonal

$$\langle k' \mid \hat{T} \mid k\rangle = T_k\delta(k - k') = \frac{\hbar^2 k^2}{2m}\delta(k - k'). \tag{2.78}$$

The basis vectors of position space and of momentum space can be transmitted to each other by the following expression relation

$$\langle k \mid x\rangle = \frac{1}{\sqrt{2\pi}} e^{-ikx}. \tag{2.79}$$

Using this transformation and the completeness of the basis vectors of the momentum space, we can derive an expression for a matrix element of the Hamilton operator in position space

$$\begin{aligned}
\langle x \mid \hat{H} \mid x'\rangle &= \langle x \mid \hat{T} \mid x'\rangle + V(x)\delta(x - x') \\
&= \langle x| \left\{ \int_{-\infty}^{\infty} |k'\rangle\langle k'|dk' \right\} \hat{T} \left\{ \int_{-\infty}^{\infty} |k\rangle\langle k|dk \right\} |x'\rangle + V(x)\delta(x - x') \\
&= \int_{-\infty}^{\infty} \langle x|k\rangle \; T_k\langle k|x'\rangle dk + V(x)\delta(x - x') \\
&= \frac{1}{2\pi} \int_{-\infty}^{\infty} e^{ik(x-x')} T_k dk + V(x)\delta(x - x').
\end{aligned} \tag{2.80}$$

The continuous function x is replaced by a set of discrete grid points x_i. For a grid with N grid points, spaced by a fixed interval Δx, any grid point x_i can be found by

$$x_i = i\Delta x, \qquad i = 1, ..., N. \tag{2.81}$$

The eigenvectors of the discrete basis satisfy

$$\Delta x \langle x_i \mid x_j \rangle = \delta_{ij}, \tag{2.82}$$

$$\hat{I}_x = \sum_{i=1}^{N} \mid x_i \rangle \Delta x \langle x_i \mid . \tag{2.83}$$

Using this discrete basis in position space the matrix elements $\langle x_i \mid \hat{H} \mid x_j \rangle$ are given by

$$H_{ij} = \frac{1}{\Delta x} \left\{ \sum_{l=-N/2}^{N/2} \frac{e^{il2\pi(i-j)/N}}{N} \cdot T_l + V(x_i)\delta_{ij} \right\}, \tag{2.84}$$

where

$$T_l = \frac{\hbar^2}{2m} \cdot (l\Delta k)^2, \qquad \Delta k = \frac{2\pi}{N\Delta x}. \tag{2.85}$$

Diagonalizing the N $\times$ N matrix of the Hamilton operator 2.84 yields the eigenvectors and eigenvalues of H_{ij} on the chosen grid. However, there exist numerous, efficient algorithms for diagonalizing Hermitian matrices. The major drawback of the method is its grid size dependency where the size of the grid representation of the Hamilton matrix which has to be diagonalized for a system with N grid points is N^2. The most important technical limitation is the amount of memory where the complete matrix has to be kept during the calculation. An advantage of the FGH method is that the discrimination used for position space is also used for the following quantum dynamical calculations. Accordingly, the numerical error caused by the transformation from one finite reduced basis to another does not exist. The Fourier Grid Hamiltonian method [114, 115], whose principles are described in this section, is employed to solve equation 2.69 and obtain the initial rovibrational state in the position space of the fulvene (Chapter 3) and 4MCF (Chapter 4) systems investigated in this thesis. For the fulvene system, the vibrational eigenfunctions are calculated using the QMBOUND program implemented in the WAVEPACKET package [116]. In a similar manner, the FGH method was used to obtain the vibrational eigenfunctions for the 2D vibrational eigenfunctions of the ground state of the fulvene system using the QMBOUND program implemented in the WAVEPACKET package [116]. For the 4MCF system, the 2D ground state eigenfunction is obtained by first, calculating two ground state 1D eigenfunctions with the FGH method. Then, an initial 2D guess is prepared as the product of both 1D eigenfunctions. Finally, this guess is relaxed to a minimum by propagating it in imaginary time [117].

2.4 The Time-Dependent Schrödinger Equation

The solution of the time-independent nuclear Schrödinger equation yields the rovibrational eigenstates and eigen energies of the molecular system. To describe the time-dependent properties of the model system (its interaction with a time-dependent laser field) it is necessary to solve the time-dependent nuclear Schrödinger equation (TDSE). The resulting wave packet dynamics are obtained by solving the TDSE numerically as it will be discussed in section 2.4.2. The dynamics of the nuclear frame of a molecule is described by the time-dependent nuclear Schrödinger equation

$$i\hbar\frac{\partial}{\partial t} \mid \Psi(t)\rangle = \hat{H}(t) \mid \Psi(t)\rangle. \tag{2.86}$$

The wave function $|\Psi(t)\rangle$ is the total wave function for the system, which consists of a sum over all (orthonormal) electronic and nuclear wave functions:

$$|\Psi(r,R,t)\rangle = \sum_i \Psi_i(r;R)\Psi_{iN}(R,t), \tag{2.87}$$

where the nuclear quantum number N refers to the initial vibrational state. From this point on, only the variable t will be retained in the notation, and the coordinates r and R will be dropped for simplicity of notation. The time-dependent Hamiltonian consists of the total molecular Hamiltonian, see eq. 2.52, and a time-dependent potential energy term $\hat{V}^{ext}(t)$ arising from the interaction of the molecular dipole moment $\vec{\mu}$ with an external electromagnetic field $\vec{E}(t)$ [33]:

$$\hat{H}(t) = \hat{H} - \underbrace{\vec{\mu}\cdot\vec{E}(t)}_{\hat{V}^{ext}}. \tag{2.88}$$

The total dipole moment consists of the electronic and nuclear dipole moments, and it is given by

$$\vec{\mu} = \underbrace{\sum_{i=1}^{N}(-e)\vec{r}_i}_{\vec{\mu}_e} + \underbrace{\sum_{A=1}^{M}(Z_A e)\vec{R}_A}_{\vec{\mu}_N}, \tag{2.89}$$

where e is charge of electron, $\vec{r}_i$ are position vectors of the electrons, and $\vec{R}_A$ are position vectors of the nuclei. If we have more than one electronic state, the wave function $\mid \Psi(t)\rangle$ can be written as a vector and the Hamilton operator as a matrix (see eq. 2.86 and 2.52)

$$i\hbar\frac{\partial}{\partial t}\begin{pmatrix} \mid \Psi_{0N}(t)\rangle \\ \vdots \\ \mid \Psi_{nN}(t)\rangle \end{pmatrix} = \begin{pmatrix} \hat{H}_{00} & \dots & \hat{H}_{0n} \\ \vdots & \ddots & \vdots \\ \hat{H}_{n0} & \dots & \hat{H}_{nn} \end{pmatrix}\begin{pmatrix} \mid \Psi_{0N}(t)\rangle \\ \vdots \\ \mid \Psi_{nN}(t)\rangle \end{pmatrix}. \tag{2.90}$$

Here, the indexes $0, 1, ..., n$ denote the electronic states. The i^{th} time-dependent wave function describes the time evolution of the i^{th} electronic state. The matrix elements of the adiabatic Hamiltonian for two states system can then be written as

$$\hat{H}^{ad}(t) = \begin{pmatrix} \hat{T} + \hat{V}_0 - \Lambda_{00} - \vec{\mu}_{00}.\vec{E}(t) & -\Lambda_{01} - \vec{\mu}_{01} \cdot \vec{E}(t) \\ -\Lambda_{10} - \vec{\mu}_{01} \cdot \vec{E}(t) & \hat{T} + \hat{V}_1 - \Lambda_{11} - \vec{\mu}_{11}.\vec{E}(t) \end{pmatrix}. \tag{2.91}$$

The diagonal dipole moment terms correspond to permanent dipole moments, whereas the off-diagonal dipole terms correspond to transition dipole moment terms between different electronic states. The coupling between different electronic states results through the NACTs and the time-dependent electromagnetic field which stimulates transitions from one electronic state to another. The diagonal elements of the matrix of the external field cause transitions within the electronic states. That is to say, the excitation from one rovibrational state to another for adiabatic states. The off-diagonal elements cause transitions from one electronic state to another.
The matrix elements of the diabatic Hamiltonian for two states system can then be written as

$$\hat{H}^{d}(t) = \begin{pmatrix} \hat{T} + W_{00} - \vec{\mu}^{d}_{00}.\vec{E}(t) & W_{01} - \vec{\mu}^{d}_{01} \cdot \vec{E}(t) \\ W_{10} - \vec{\mu}^{d}_{01} \cdot \vec{E}(t) & \hat{T} + W_{11} - \vec{\mu}^{d}_{11}.\vec{E}(t) \end{pmatrix}. \tag{2.92}$$

Here, $\vec{\mu}^{d}_{ij}$ are the diabatic dipole moment elements obtained according to the unitary transformation matrix U defined in eq. 2.54:

$$U(R) \begin{pmatrix} \mu^{ad}_{00} & \mu^{ad}_{01} \\ \mu^{ad}_{10} & \mu^{ad}_{11} \end{pmatrix} U(R)^{\dagger} = \begin{pmatrix} \mu^{d}_{00} & \mu^{d}_{01} \\ \mu^{d}_{10} & \mu^{d}_{11} \end{pmatrix} \tag{2.93}$$

In order to adequately describe the coupled motion on two states we have to consider two nuclear wave packets. The time-evolution of the molecular system is then illustrated by the time-independent Schrödinger equation where the coupling is represented by the nondiagonal potential elements. Regardless of the number of implied electronic states the solution TDSE can be expressed in a general form using the time evolution operator $\hat{U}$ [118]:

$$\mid \Psi(t)\rangle = \hat{U}(t, t_0) \mid \Psi(t_0)\rangle. \tag{2.94}$$

The evolution operator propagates the wave function from time t_0 to time t. The TDSE equation must hold for any initial wave function, therefore, the evolution operator must satisfy the same equation. Accordingly, $\hat{U}(t, t_0)$ can be rewritten in an integral form:

$$\hat{U}(t, t_0) = \hat{1} - \frac{i}{\hbar} \int_{t_0}^{t} \hat{H}(t')\hat{U}(t', t_0)dt'. \tag{2.95}$$

This equation can be solved iteratively. Then the following expansion for the time evolution operator is derived [119]:

$$\hat{U}(t,t_0) = \hat{1} + \sum_{n=1}^{\infty} (-\frac{i}{\hbar})^n \int_{t_0}^{t} dt_n \int_{t_0}^{t_n} dt_{n-1} \ldots \int_{t_0}^{t_2} dt_1 \hat{H}(t_n)\hat{H}(t_n - 1)\ldots\hat{H}(t_1). \quad (2.96)$$

If the Hamilton operator is not explicitly a function of time the previous expression of the time evolution operator simplifies to:

$$\hat{U}(t,t_0) = e^{-\frac{i}{\hbar}\hat{H}(t-t_0)} \quad \text{for} \quad \hat{H} \neq \hat{H}(t). \quad (2.97)$$

In this case the system is conservative, i.e. the total energy of the molecule is constant.

2.4.1 Time Discretisation

The Hamiltonian operator is explicitly time-dependent since it includes a time-dependent perturbation that covers all interactions of the molecule with electromagnetic radiation (laser pulses). Practically, the time axis is discretised in adequately small segments Δt in which the Hamiltonian operator can be considered to be time-independent. Accordingly, the result of applying this time evolution operator to an initial wave function is the successive propagation of the function over a time interval of [119]

$$\mid \Psi(t)\rangle = \hat{U}(t,t_n)\hat{U}(t_n,t_{n-1})\ldots\hat{U}(t_1,t_0) \mid \Psi(t_0)\rangle, \quad (2.98)$$

Where each partial evolution operator is given as:

$$\hat{U}(t_i,t_{i-1}) = e^{-\frac{i}{\hbar}\hat{H}(t_i - t_{i-1})} = e^{-\frac{i}{\hbar}\hat{H}(t_i)\Delta t}, \quad (2.99)$$

with

$$t_i - t_{i-1} = \Delta t. \quad (2.100)$$

2.4.2 Propagation Schemes: the Split-Operator Method

Several numerical routines can be used to solve the time-dependent Schrödinger equation. Here, the focus will be on the split-operator method [120, 121] that has been used in this study. The total Hamilton operator is not diagonal in the grid

representation. This implies that the kinetic energy operator does not commute with the potential energy operator

$$[\hat{T}, \hat{V}] \neq 0. \tag{2.101}$$

Hence,the effect of the evolution operator cannot be directly calculated within this representation. Accordingly, the evolution operator cannot be split, generally, in the following way:

$$e^{-\frac{i}{\hbar}\hat{H}\Delta t} = e^{-\frac{i}{\hbar}(\hat{T}+\hat{V})\Delta t} \neq e^{-\frac{i}{\hbar}\hat{T}\Delta t} \cdot e^{-\frac{i}{\hbar}\hat{V}\Delta t}. \tag{2.102}$$

For very small time steps Δt, the following decomposition, in which the kinetic operator is split in two parts, is possible [121, 122, 123, 124]:

$$e^{-\frac{i}{\hbar}(\hat{T}+\hat{V})\Delta t} \approx e^{-\frac{i}{\hbar}\frac{\hat{T}}{2}\Delta t} \cdot e^{-\frac{i}{\hbar}\hat{V}\Delta t} \cdot e^{-\frac{i}{\hbar}\frac{\hat{T}}{2}\Delta t} + \mathcal{O}(\Delta \mathrm{t})^3. \tag{2.103}$$

This decomposition of the Hamilton operator is called split operator and involves a numerical error of third order $\mathcal{O}(\Delta t)^3$. The error of the calculation will be comparatively small if the time intervals are chosen sufficiently small. Such small time steps also result in an approximately time-independent Hamilton operator for the time-dependent electromagnetic field changes very slowly within a single time interval. The Split operator is unitary and conserves the norm. The time propagation of a wave function is done in several steps. First, the initial wave function on the grid at time t_0 (e.g. an eigenfunction of the system) is transformed from position space to momentum space via Fourier transformation, see section 2.3.1. Then, it is multiplied by $e^{-\frac{i}{\hbar}\frac{\hat{T}}{2}\Delta t}$ and accordingly, transformed back to position space. The next step would be multiplying by $e^{-\frac{i}{\hbar}\hat{V}\Delta t}$, transformed back to k-space and again multiplied by $e^{-\frac{i}{\hbar}\frac{\hat{T}}{2}\Delta t}$. Finally, the wave function is transformed once again to position space and a wave function $\mid \Psi_k(t_0 + \Delta t)\rangle$ propagated by Δt is achieved. Like so, the wave function is propagated step by step until a final time t_f. For two diabatic states system, the time evolution operator can be written as [125]:

$$exp\left[-\frac{i}{\hbar}\begin{pmatrix}\hat{T}_N + \hat{V}_0 & V_{01} \\ V_{10} & \hat{T}_N + \hat{V}_1\end{pmatrix}\Delta t\right] = exp\left[-\frac{i}{\hbar}\begin{pmatrix}\hat{T_N} & 0 \\ 0 & \hat{T}_N\end{pmatrix}\frac{\Delta t}{2}\right] exp\left[-\frac{i}{\hbar}\begin{pmatrix}\hat{V}_0 & V_{01} \\ V_{10} & \hat{V}_1\end{pmatrix}\Delta t\right]$$
$$\times exp\left[-\frac{i}{\hbar}\begin{pmatrix}\hat{T_N} & 0 \\ 0 & \hat{T}_N\end{pmatrix}\frac{\Delta t}{2}\right] + \mathcal{O}(\Delta \mathrm{t})^3. \tag{2.104}$$

In the diabatic representation the potential energy matrix in equation 2.104 is not diagonal which makes evaluating the imaginary matrix more difficult. However, one can work out this difficulty by transforming the non-diagonal potential matrix into a representation in which it is diagonal, and then transforming back after the

multiplication operation of the wave function is performed. For two electronic states this transformation can be done analytically [126]:

$$exp\left[-\frac{i}{\hbar}\begin{pmatrix} W_{00} & W_{01} \\ W_{10} & W_{11} \end{pmatrix}\Delta t\right] = U exp\left[-\frac{i}{\hbar}U^{\dagger}\begin{pmatrix} W_{00} & W_{01} \\ W_{10} & W_{11} \end{pmatrix}U\Delta t\right]U^{\dagger} = U\begin{pmatrix} e^{-\frac{i}{\hbar}\lambda_0\Delta t} & 0 \\ 0 & e^{-\frac{i}{\hbar}\lambda_1\Delta t} \end{pmatrix}U^{\dagger} \tag{2.105}$$

$$= exp\left[-\frac{i}{\hbar}(W_{00}+W_{11})\frac{\Delta t}{2}\right]\left[\cos(\sqrt{D}\frac{\Delta t}{2\hbar})\begin{pmatrix} 1 & 0 \\ 0 & 1 \end{pmatrix} + i\frac{\sin(\sqrt{D}\frac{\Delta t}{2\hbar})}{\sqrt{D}}\begin{pmatrix} W_{11}-W_{00} & -2W_{01} \\ -2W_{10} & W_{00}-W_{11} \end{pmatrix}\right]. \tag{2.106}$$

Here, $D = (W_{11} - W_{00})^2 + 4W_{01}^2$ and $\lambda_{0,1} = \frac{1}{2}(W_{11} + W_{00} \pm \sqrt{D})$ [125]. Since the potential matrix is coordinate dependent, the same applied for the unitary transformation matrix U, that diagonalizes it [126].

2.4.3 Time-Dependent Laser Field

The operator for the interaction of the molecule with the laser field is described in eq. 2.90 by the semi-classical dipole approximation [127]. In laboratory fixed coordinates, the magnetic dipole and the electric quadrupole are neglected, because they are about two orders of magnitude smaller than the electric dipole. Electromagnetic Field $\vec{E}(R,t)$ is used to control intra-molecular motion in general and it is given by the following expression:

$$\vec{E}(\vec{R},t) = \vec{\epsilon^p}\cdot\vec{E}^0\cdot s(t)\cdot\frac{e^{i(\vec{k}\vec{R}-\omega t)}+e^{-i(\vec{k}\vec{R}-\omega t)}}{2}. \tag{2.107}$$

here $\vec{E}^0$ is the amplitude of the field with the carrier frequency ω, $\vec{\epsilon^p}$ the polarization vector, $\vec{k}$ the wave vector, and $s(t)$ the shape function which describes the envelope of the laser pulse. The term $e^{i\vec{k}R}$ can be expanded in the Taylor series:

$$e^{i\vec{k}\vec{R}} \approx 1 + i\vec{k}\vec{R} + \dots. \tag{2.108}$$

This Taylor series can be truncated after the first term since all the molecules considered throughout this study are of dimensions not larger than $6\mathring{A}$ while the laser pulses cover a range of wavelengths starting from at least $100\mathring{A}$. Accordingly, an expression for a position-independent field is obtained

$$\vec{E}(t) = \vec{\epsilon^p}\cdot\vec{E}^0\cdot s(t)\cdot\frac{e^{i\omega t}+e^{-i\omega t}}{2}. \tag{2.109}$$

Using the Euler formula and combining the polarization vector with the amplitude, this equation simplifies to:

$$\vec{E}(t) = \vec{E}^0 \cdot s(t)cos(\omega t). \tag{2.110}$$

The shape function $s(t)$ used in this study is given by [128]:

$$s(t) = sin^2\left(\frac{\pi(t-t_d)}{t_p}\right), \quad \text{for} \quad t_d \leq t \leq t_d + t_p \tag{2.111}$$

where t_p is the pulse duration and t_d is the starting time, also called delay time, of the current laser pulse in a laser pulse sequence. In the following section, the methods of laser pulse control applied in this study, is introduced.

2.4.4 Analytical Laser Pulses

Analytical laser pulses are well defined laser fields with analytical shape functions which are functioning as either a pump pulse to excite population from one energetically low lying state to another state higher in energy or as a dump pulse causing a stimulated emission back to an energetically lower state. Pump-dump schemes using analytical laser pulses developed by Paramonov and coworkers [36] and Tannor and Rice [129, 130] are a common approach to laser pulse control of a quantum dynamical system. Before a suitable laser pulse sequence is constructed it is necessary to develop an efficient reaction mechanism that leads the system selectively from a initial state via one or more transition states to the final state. The laser pulses should be designed such that all transitions are selective. That is to say, they only transfer population from the initial state to the desired state without exciting population to other states, and effective, in the sense that the desired amount of population is excited/de-excited. An analytical laser pulse is usually of the form defined in equation. 2.110. For a sequence of linearly polarized laser pulses with sin^2-shape function the following expression is obtained:

$$\vec{E}_i(t) = \vec{E}_i^0 \cdot sin^2\left(\frac{\pi(t-t_{di})}{t_{pi}}\right) \cdot \cos(\omega_i(t-t_{di}) + \rho_i) \tag{2.112}$$
$$for\ t_{di} \leq t \leq t_{di} + t_{pi}.$$

Here $\vec{E}_i^0$ is the amplitude of the laser field, ρ_i the time-independent phase, t_{pi} is the pulse duration, t_{di} the starting time and ω_i the frequency of the pulse i. For an initial

guess of an suitable laser pulse it is important to know the transition frequency ω_i, that is the energy gap between the affected states. Still, the optimal laser frequency is usually detuned to some extent from the exact transition frequency. This is originated by the interaction of the electric field with the diagonal elements of the transition dipole matrix μ_{ij}. While the off-diagonal terms cause transitions between different states, the diagonal terms result in a shift of the energy of the levels. The energy levels will shift by a different amount causing a change in the energy difference of states compared with the system without laser field. Consequently, the optimal laser pulse frequency has to be found by detuning ω_i until a acceptable result is obtained. The choice of a suitable time duration of the laser pulse is fairly affected by the uncertainty principle. If the laser pulse is on the one hand too short, then states different from the desired ones might also be affected. If the laser pulse is on the other hand relatively long, then the effectiveness of the laser control is destroyed by competing effects like intra-molecular vibrational redistribution (IVR) that may take place. For a complete transition of the population in a two-level system from state $|\Psi_i\rangle$ to state $|\Psi_j\rangle$ (population inversion) a so-called π-pulse is most effective [131]. In terms of the area theorem (see ref. [132]) population inversion in a two-level system is obtained if the area A under the pulse envelope, multiplied by the transition dipole matrix element μ_{ij}, and divided by Planck's constant, becomes equal to an odd multiple of π:

$$A = \int_0^{t_p} \Omega(t)dt = \frac{\vec{\mu}_{ij}}{\hbar} \int_0^{t_p} |\vec{E}_i^0| s(t)dt = (2N+1) \cdot \pi \quad with \quad N = 0, 1, \ldots \quad (2.113)$$

here $\Omega(t)$ is the so-called Rabi frequency given by:

$$\Omega(t) = \frac{\vec{\mu}_{ij}\vec{E}(t)}{\hbar}. \quad (2.114)$$

The Rabi frequency for a given atomic transition in a given light field gives the strength of the coupling between the light and the transition. Then, the amplitude of the laser pulse $\vec{E}_i^0$ depends on its duration and on the transition dipole matrix elements $\vec{\mu}_{ij}$. This is an approximation for a two-level system, but it can be extended to multi-level system using supposed generalized π-pulses [133]. Nevertheless, even a simple π-pulse is very suitable for generating an initial guess for a laser pulse in a multi-level system. For sin^2-shaped laser pulses their amplitude is then approximated by

$$|\vec{E}_i^0| \approx \frac{2\pi.\hbar}{|\vec{\mu}_{ij}|.t_p}. \quad (2.115)$$

Eventually the laser pulse parameters must be optimized (in this study, manually). A precondition for using analytical laser pulses is that a good insight into the quantum system is mandatory. Transition dipole matrix elements $\vec{\mu}_{ij}$ must be analyzed to

get the most effective transition and many different laser pulse parameters must be optimized. Frequently, it is a huge challenge to design a proper reaction mechanism that in due course yields full control over the molecular system. Still, analyzing the system and designing mechanisms for effective transitions give a very good understanding of how control is accomplished. The knowledge gained from these studies can be used by e.g. experimentalists to design a desired laser pulse sequence to reach an intended state.

2.4.5 Properties of the Electric Field

In quantum dynamical simulations, the electric field is typically designed to perform a special task, for example initiating a ro-vibrational or electronic transition. Studying wave packet dynamics, or the dynamics of non-stationary states, is useful to understand the time-dependent evolution of a quantum mechanical system where radiation, either in the form of continuous wave (cw) or short pulses, can be applied to create the wave packet(s) [134]. In this section, different electric field properties will be discussed.

Intensity

The maximum intensity of the light, I_{max}, is related to the field strength through

$$I_{max} = \epsilon_0 c \max |\vec{E}(t)|^2 = \epsilon_0 c (|\vec{E}^0|)^2, \tag{2.116}$$

here ϵ_0 is the permittivity constant and c is the speed of light [135]. Maximum laser field intensities in quantum dynamical simulations are kept below the so-called Keldysh limit, typically $I_{max} < 10^{13} W/cm^2$ [136], to avoid undesired ionization processes. The duration t_p of a laser pulse and the spectral width $\Delta\omega$ are related through a Fourier transform. Generally, the time and frequency components of light build what is called a Fourier pair [137]:

$$f(t) = \frac{1}{\sqrt{2\pi}} \int_{-\infty}^{+\infty} \mathcal{F}(\omega) \mathrm{e}^{\mathrm{i}\omega \mathrm{t}} \mathrm{d}\omega, \qquad \mathcal{F}(\omega) = \frac{1}{\sqrt{2\pi}} \int_{-\infty}^{+\infty} f(\mathrm{t}) \mathrm{e}^{-\mathrm{i}\omega \mathrm{t}} \mathrm{dt}, \tag{2.117}$$

here $f(t)$ is the function describing the electric field in the time domain ($\equiv E(t)$), and $\mathcal{F}(\omega)$ is the function describing the electric field in the frequency domain. The duration Δt and spectral width $\Delta\omega$ are related by Heisenberg's uncertainty principle,

$$\Delta t \Delta \omega \geq \frac{1}{2}, \tag{2.118}$$

here the equality in equation. 2.118 is only reached with time and spectral envelopes of Gaussian form where the pulse is called Fourier-transform limited [137] and is the shortest pulse possible. However, pulses need not be Fourier-transform limited.

Few-cycle Pulses

Few-cycle pulses are laser pulses whose envelope varies on a time scale comparable to that of the electromagnetic field itself [138]. The frequency of the radiation thus dictates the duration of the few-cycle pulse, depending on how many optical cycles are contained within the pulse envelope. Therefore, for a given number of cycles, the duration of a few-cycle IR pulse will necessarily be longer than that of a UV pulse. Current mode-locking techniques are able to deliver $\sim$ 4 fs pulses in the visible spectral region with only a single cycle [139]. As a consequence of Maxwell's equations on electromagnetism in the electric dipole approximation, freely propagating electromagnetic pulse must integrate to zero, [140, 141]:

$$\int_0^{t_p} \vec{E}(t) dt = 0 \tag{2.119}$$

2.4.6 Autocorrelation Function

The autocorrelation function is often considered to monitor the evolution of the time-dependent wave function. Autocorrelation function $Au(t)$ [50] a function that measures the overlap of the initial wave function with the time-dependent wave function at any time

$$Au(t) = \langle \Psi(t_0) \mid \Psi(t) \rangle. \tag{2.120}$$

The modulus of the autocorrelation function, is a real number whose value ranges from 0 to 1 for initially normalized wave functions. In general, the autocorrelation function is time-dependent. However, in the unique case in which the initial function $\mid \Psi(t_0) \rangle$ is itself an eigenstate of the Hamiltonian with energy E, then the autocorrelation function is just

$$Au(t) = \langle \Psi(t_0) \mid \Psi(t) \rangle = e^{-iE(t-t_0)/\hbar}. \tag{2.121}$$

Chapter 3

Photoinduced Quantum Dynamics of Fulvene

Fulvene is known to have CIs between the ground and first excited electronic states, S_0 and S_1, respectively [58, 59, 60]. It has been shown that CIs exist along the seam for all torsion angles, connecting the CI at planar structure with the CI at twisted configuration [61, 62]. The last CI is associated with cis−trans isomerization and has been located by means of the Longuet-Higgins method [60]. In this chapter, we investigate the photoinduced nonadiabatic dynamics of fulvene by a combination of quantum chemical ab initio calculations and quantum dynamical simulations. We will explore the quantum dynamics of the corresponding photoexcited nuclear wavepacket on the model ground and first excited electronic states potential energy surfaces of fulvene. Therefore, a three-dimensional model Hamiltonian for the cis−trans-isomerization of fulvene was constructed. The parameters for the adiabatic model PES are obtained from quantum chemical ab-initio data. Then the adiabatic states are transformed to "quasidiabatic" states with potential coupling. Unlike strictly diabatic ones, quasidiabatic states, may be defined as states in which the derivative coupling does not vanish completely, but remains "small". In this chapter, we will first introduce the model system describing the isomerization of fulvene and review the localization of the CI [60]. Then, we derive the diabatic PES from the adiabatic ones. Finally, we will discuss the propagation of photo-excited nuclear wavepacket on the coupled surfaces and the corresponding ultrafast non-radiative decay caused by the CIs. We will use the fulvene molecule as a model to carry out 2D dynamics simulations for two different models, one using symmetric and anti-symmetric allylic stretch modes and one using torsion and anti-symmetric allylic stretch mode, using a model Hamiltonian with linear coupling. This chap-

ter aims to learn something general on radiationless decay due to non-adiabatic vibrations and torsional motion.

3.1 Background: Localization of the CI of Fulvene

The conical intersection (CI) between the S_0 and S_1 states for the system of interest here was located using an approach based on the sign change theorem of Longuet-Higgins [25, 29, 30, 59, 142, 143]. In Ref. [60] this method was extended to describe qualitatively and quantitatively the properties of the fulvene conical intersections between the S_0 and S_1 states where the different reaction coordinates connecting the cis-trans isomers on the ground state surfaces and responsible for the main nuclear motions causing the curves to cross were considered. It has been shown that the CI between the S_0 and S_1 electronic states of fulvene involves torsion of the terminal CH_2 group as well as the anti-symmetric allylic stretch [144, 145, 146]. Rotation of the terminal CH_2 group connects two different biradical transition states (TSs): TS_1 is an ethylene-like transition state with two electrons localized on the two orthogonal p - atomic orbitals (p-AOs) where a rotation tolerates reaching both reactant and product. In TS_2 one electron is delocalized on the allyl fragment. The resulting planar biradical has B_2 symmetry and lies on the first electronically excited state (it is a critical point). An anti-symmetric b_1 vibration must be added in order to break the C_2 rotational symmetry around the C-C exocyclic bond. This mechanism clarifies the computational observation that the reaction minimal energy path which connects TS_2 (B_1) with the reactant and the product, consists of structures with C_1 symmetry rather than C_2. Consequently, the reaction coordinate via TS_2 includes main contributions of three different natural coordinates: torsion, exocyclic C-C stretch and anti-symmetric allylic stretch. In contrast, the TS_1 reaction coordinate includes only the first two. Accordingly, two coordinates can be defined for this system: Q_1 that connects the two minima (main contribution from the torsion coordinates) and Q_2 coordinate that is entirely localized in the cyclopentadienyl radical and connects the two transition states as it is shown in Figure 3.1. These coordinates (Q_1 and Q_2) define the branching space of the CI:

$$Q_1 = Q_{TS_1} + Q_{TS_2} \approx \text{torsion} + \text{exocyclic C-C stretch} \tag{3.1}$$

$$Q_2 = Q_{TS_1} - Q_{TS_2} \approx \text{anti-symmetric allylic stretch} \tag{3.2}$$

Here, Q_{TS_1} and Q_{TS_2} are the reaction coordianets via TS_1 and TS_2, respectively. The previous assembly ends in a reactant$-TS_1-$Product$-TS_2-$Reactant loop. A

four-dimensional model would include these four cooridnates. We restrict ourselves to a 3D Hamiltonian consisiting of the torsion (ϕ), symmetric and anti-symmetric allylic stretches (q_s and q_a, respectively). The coordinates used in this study to investigate the non-adiabatic vibrations and torsional motion is shown in Figure 3.2.

The adiabatic ground and excited ab-initio potential energy surfaces for fulvene

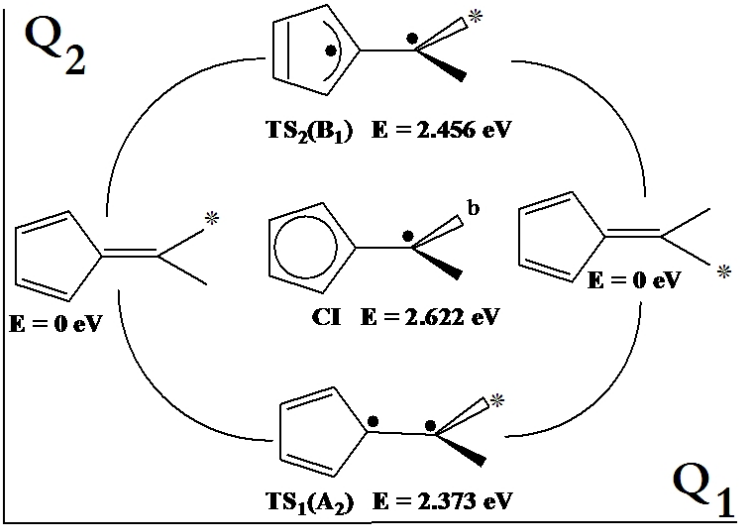

Figure 3.1: Fulvene loop. This figure is adapted from Ref. [60]. The asterisk (*) labels the relative position of the atoms changed upon rotation around the C=C bond.

have been calculated by O. Deeb [63, 87] where the adiabatic PESs $V_0(\phi, q_a, q_s)$ and $V_1(\phi, q_a, q_s)$ are calculated using the GAMESS program suite [147] using the complete active space self-consistent field CASSCF method [148] with the cc-pVDZ basis set [149, 150]. A relatively small active space was used, as done in previous studies [151, 152]. Only the six π electrons in the three double bonds were included in six orbitals (three bonding and three antibonding). The active space was chosen for sufficient calculations of the twisted CI. The CASSCF(6,6) active space includes only π and π^* orbitals in planar geometry (Figure 3.3). This active space is sufficient for the calculations of structures without breaking the σ bonding. To properly describe longer C–C bonds that would be stretched at dissociation, it is required to include the σ and σ^* orbitals in the active space. However, this is not a goal in this study. Calculations of the PESs were made assuming C_{2v} or C_2 symmetry for all proper species if applicable, otherwise C_1 symmetry was used. Two-dimensional cut of the PESs for $q_a = 0$ is shown in Figure 3.4. The minima of the electronic ground state at the Franck-Condon regions are located at a planar configuration of fulvene with C_{2v} symmetry corresponding to $\phi = \pm\pi/2$. It is interesting to notice that the steepest

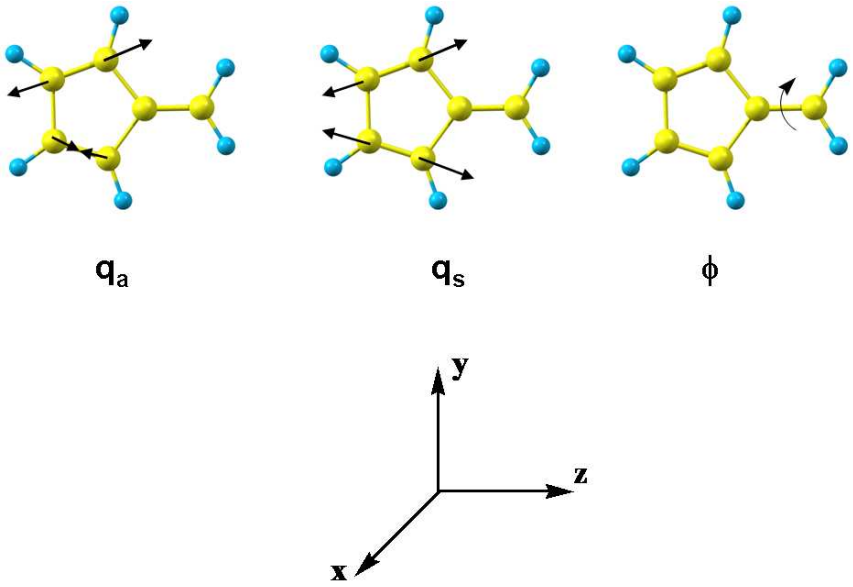

Figure 3.2: Different CI coordinates for fulvene.

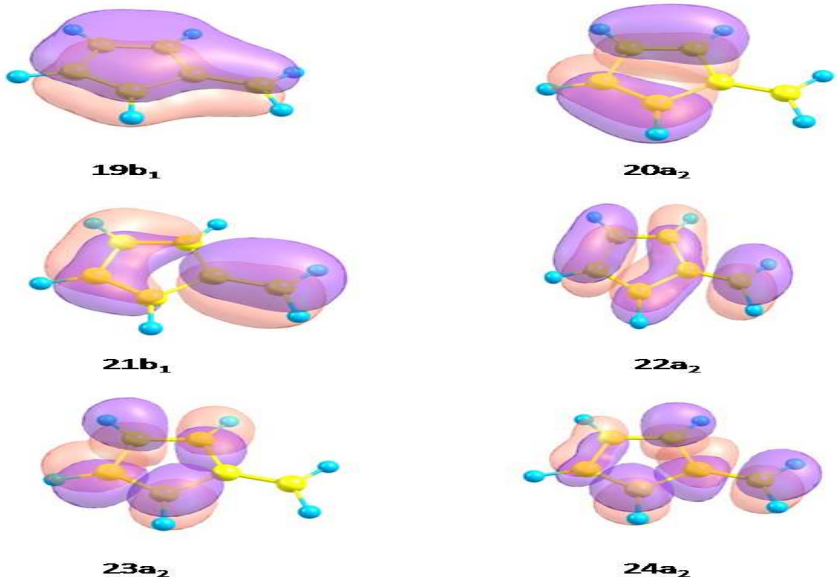

Figure 3.3: Active space used in CASSCF(6,6)cc-pVDZ calculations.

slope of the PES $V_0(\phi, q_a, q_s)$ in the Franck-Condon regions is along the coordinate q_s. The crossings of the potentials lead to a seam of the CI which starts at $\phi = -\pi$ and q_s=1.47 $\mathring{A}$ and maintains to $\phi = 0$ and π.

3.2 A Three-Dimensional Model Potential for the Cis−Trans Isomerization of Fulvene

As a first approach to build the model potentials, we start with the nuclear Hamiltonian in the adiabatic representation,

$$\hat{H}^{ad} = \begin{pmatrix} T_N + \Lambda_{11} & \Lambda_{10} \\ \Lambda_{01} & T_N + \Lambda_{00} \end{pmatrix} + \begin{pmatrix} V_1 & 0 \\ 0 & V_0 \end{pmatrix}, \tag{3.3}$$

where Λ_{10} are the adiabatic (kinetic) couplings between the potential energy surfaces V_1 and V_0. The kinetic energy operator is given by (see appendix in Ref. [63]):

$$\hat{T}_N = -\frac{\hbar^2}{2I_r}\frac{\partial^2}{\partial\phi^2} - \frac{\hbar^2}{2m_r}\left(\frac{\partial^2}{\partial q_a^2} + \frac{\partial^2}{\partial q_s^2}\right). \tag{3.4}$$

Where I_r is the reduced moment of inertia, $\hbar = \frac{h}{2\pi}$, where h is Planck's constant, q_a and q_s describe the anti-symmetric and symmetric allylic stretch, ϕ is the torsion angle and m_r, (where $m_r = m_C + m_H$) is the effective mass relevant for nuclear vibrations in q_a and q_s direction.

The adiabatic potential energy surfaces are modeled by

$$V_{0/1} = \frac{1}{2}(V_e + V_g) \pm \frac{1}{2}\sqrt{(V_e - V_g)^2 + \lambda^2 q_a^2}, \tag{3.5}$$

where λ is the coupling strength, V_g and V_e are the potential energy functions of the ground and first excited states, respectively.

$$\begin{aligned} V_g &= \frac{v_0}{2}\left[1 + \cos(2\phi)\right] + \frac{1}{2}m_r\omega_{ag}^2 q_a^2 + \frac{1}{2}m_r\omega_{sg}^2 q_s^2 \\ V_e &= E_1 - \frac{v_1}{2}\left[1 + \cos(2\phi)\right] + \frac{1}{2}m_r\omega_{ae}^2 q_a^2 + \frac{1}{2}m_r\omega_{se}^2 (q_s - q_{s0})^2, \end{aligned} \tag{3.6}$$

Here, v_0 and v_1 are parameters of the ground and first excited state model PESs (V_g and V_e, respectively). ω_{ag} and ω_{sg} are the frequencies of the ground state and ω_{ae} and ω_{se} are the frequencies of the excited state and E_1 is the energy difference between the

Table 3.1: Parameters used to obtain the model adiabatic potential energy surfaces.

Parameter	**Value**
I_r	$1.711 m_H \text{Å}^2$
m_r	$13u$
v_0	2.09eV
v_1	0.26eV
E_1	2.93eV
$\omega_{ag}/2\pi$	2921 cm^{-1}
$\omega_{ae}/2\pi$	7012 cm^{-1}
$\omega_{sg}/2\pi$	1459 cm^{-1}
$\omega_{se}/2\pi$	1540 cm^{-1}
$t_{vib(\omega_{ag})}$	11.4 fs
$t_{vib(\omega_{ae})}$	47.6 fs
$t_{vib(\omega_{sg})}$	22.9 fs
$t_{vib(\omega_{se})}$	21.6 fs
q_{s0}	0.1Å.
$q_{s,eq}$	2.76Å.

ground and excited states potentials at the equilibrium geometry. The parameters used for building the model adiabatic potential energy surfaces for fulvene are shown in Table 3.1. These parameters are obtained from ab-initio calculations carried out by O. Deeb (see section 3.1).

The two surfaces V_0 and V_1 cross if $q_a = 0$ (see Figure 3.4). The seam of the conical intersection is defined by

$$V_e(q_a = 0) - V_g(q_a = 0) = 0 \tag{3.7}$$

It follows from eq.(3.6) that the conical intersection is located at

$$q_{sci}(\phi) = a\left(1 - \sqrt{1-b}\right), \tag{3.8}$$

with the abbreviations

$$\begin{aligned} a &= q_{s0}\frac{\omega_{se}^2}{\omega_{se}^2 - \omega_{sg}^2} \\ b &= \frac{2(\omega_{se}^2 - \omega_{sg}^2)}{\omega_{se}^4 m_r q_{s0}^2}\left[V_e(\phi, q_a = 0, q_s = 0) - V_g(\phi, q_a = 0, q_s = 0)\right]. \end{aligned} \tag{3.9}$$

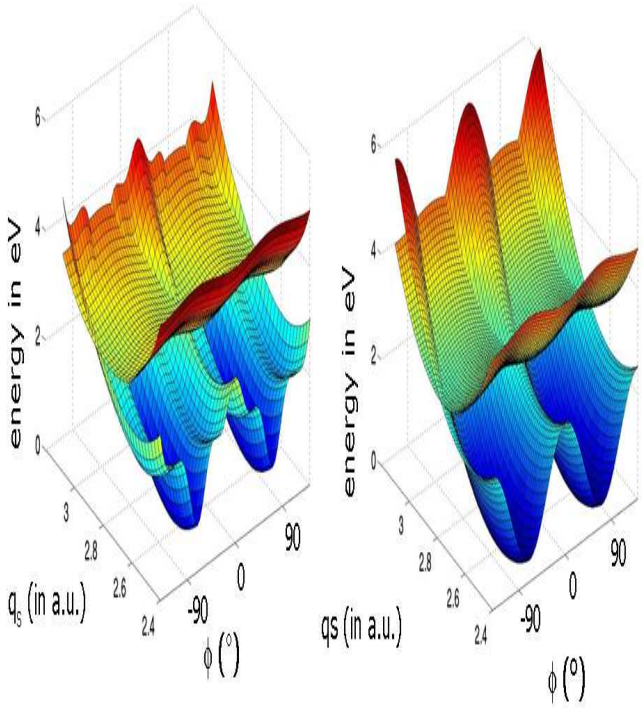

Figure 3.4: Two-dimensional adiabatic potential energy surfaces for the symmetric allylic stretch (q_s) and torsion (ϕ) for $q_a = 0$. The figure to the right is the one obtained from the ab initio calculations (1.33 $\mathring{A} \leq q_s \leq$ 1.64 $\mathring{A}$) and the figure to the lift shows the model PES.

Figure 3.5 shows the seam of the conical intersection (eq. 3.8) q_{sci} as a function of the torsion angle ϕ (green curve). This figure shows that the second solution of eq. 3.7 (blue curve) is not relevant for the cis−trans-isomerization of fulvene because the energy of that second seam of a conical interaction is too high as Figure 3.4 and 3.5 show.

3.3 Transformation to Diabatic Basis.

Kinetic coupling between energetically well separated adiabatic electronic states can be neglected. When the energy gap between the two electronic states is small, such as close to a conical intersection, the Born-Oppenheimer approximation is not valid any more and the kinetic coupling becomes infinite. The fact that fulvene has

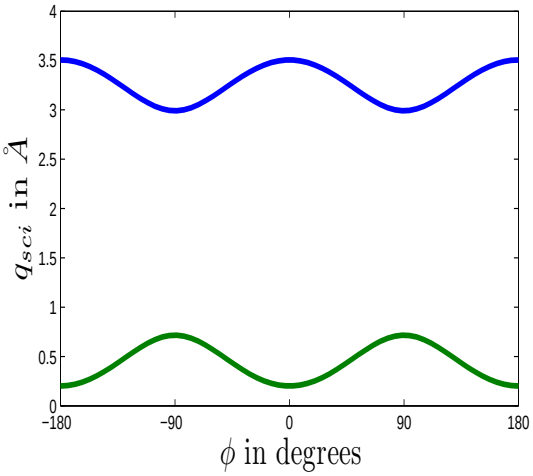

Figure 3.5: Seam of the conical intersection for the torsion and symmetric allylic stretch coordinates. The energetically relevant seam is the green curve.

a CI between the S_0 and S_1 states implies that the nonadiabatic coupling terms in the Hamiltonian between the adiabatic electronic states, which determine the efficiency of the ultrafast radiationless decay between the electronic states, cannot be neglected. A transformation to the so-called diabatic basis, removes the singularities in the kinetic coupling term Λ_{10} and Λ_{01}. In order to transform the adiabatic Hamiltonian $\hat{H}^{ad}$ to a diabatic one $\hat{H}^{d}$, we introduce a unitary transformation such that

$$\hat{H}^{d} = U H^{ad} U^{\dagger}, \tag{3.10}$$

with

$$U = \begin{pmatrix} \cos\alpha & -\sin\alpha \\ \sin\alpha & \cos\alpha \end{pmatrix}, \tag{3.11}$$

where $\alpha = \alpha(\phi, q_a, q_s)$ is the adiabatic-diabatic mixing angle. The transformation shall be such that

$$U \begin{pmatrix} T_N + \Lambda_{11} & \Lambda_{10} \\ \Lambda_{01} & T_N + \Lambda_{00} \end{pmatrix} U^{\dagger} \approx \begin{pmatrix} T_N & 0 \\ 0 & T_N \end{pmatrix} \tag{3.12}$$

As a consequence, the potential matrix is no longer diagonal. The coupling between the electronic states now appears in form of the potential coupling terms $W_{01} = W_{10}$ in

$$U \begin{pmatrix} V_1 & 0 \\ 0 & V_0 \end{pmatrix} U^{\dagger} = \begin{pmatrix} W_{11} & W_{10} \\ W_{01} & W_{00} \end{pmatrix}. \tag{3.13}$$

The potential couplings are smooth functions of the coordinate and do not have singularities. In general, the kinetic coupling term have to be calculated via ab initio methods in order to find the transformation matrix U. To avoid the tedious ab initio calculations, one often assumes linear model potential couplings [153]. The form of the model Hamiltonian in eq. 3.5 suggests that one can assume

$$W_{10} = W_{01} = \frac{1}{2}\lambda q_a \tag{3.14}$$

(Where, λ is the coupling constant) and

$$W_{00} = V_e \text{ and } W_{11} = V_g \tag{3.15}$$

It is also possible to extract quasi-diabatic potentials from the adiabatic potentials without knowing the coupling terms [110, 153, 154]. Here, we demonstrate the construction of quasi-diabatic potentials using the model potentials in eq. 3.5. Following Refs. [59, 153, 154], the matrix elements of the quasi-diabatic potentials are defined as

$$\begin{aligned} W_{11} &= \frac{1}{2}(V_1 + V_0) + d \\ W_{00} &= \frac{1}{2}(V_1 + V_0) - d \\ W_{01} = W_{10} &= o_f \end{aligned} \tag{3.16}$$

Where W_{11} and W_{00} refer to the higher and lower diabatic potentials, respectively. W_{01} refers to the diabatic coupling element. The potential coupling elements $W_{01} = W_{10}$ are smooth functions of the nuclear coordinates and vanish at the CI. They are linear functions close to the CI of the nuclear coordinates. Fulvene has a symmetry allowed CI between the ground electronic state of A symmetry in C_2 (gerada symmetry) and the first excited electronic state of B symmetry (ungerada symmetry). The torsion angle ϕ and symmetric allylic stretch q_s transform as A in C_2, and the anti-symmetric allylic stretch q_a transforms as B. Therefore, the linear off-diagonal terms W_{10} are nonzero only for q_a, while the linear diagonal terms contain only ϕ and q_s (see Ref. [155]). From eqs. 3.11 and 3.13, it follows that

$$\tan 2\alpha = \frac{2W_{10}}{W_{00} - W_{11}} \tag{3.17}$$

or

$$\Delta V = \frac{1}{2}(V_1 - V_0) = \sqrt{o_f^2 + d^2}. \tag{3.18}$$

To construct the diabatic potentials, we consider cuts of the PES with constant torsion angle. Explicitly $V_0(q_a, q_s; \phi)$ and $V_1(q_a, q_s; \phi)$ with the torsion angle ϕ as a

parameter. The CI is localized at $q_a = 0$ and $q_s = q_{ci}(\phi)$. The function q_{ci} describes the seam of the CI. Therefore, to determine the functions $o(\phi, q_a, q_s)$ and $d(\phi, q_a, q_s)$, we fix the coordinate ϕ and make the coordinate transformation (see Table 3.2)

$$\tilde{q_s} = q_s - q_{sci}(\phi). \tag{3.19}$$

with q_{sci} defined in eq. 3.8. Now, the conical intersection is located at $q_a = 0$ and $q_{sci}(\phi) = 0$ for every angle ϕ and

$$o_f(\phi, q_a = 0, \tilde{q_s}(\phi) = 0) = d(\phi, q_a = 0, \tilde{q_s}(\phi) = 0) = 0. \tag{3.20}$$

Table 3.2: Parameters used to diabatize the model adiabatic potential energy surfaces.

Parameter	**Description**
d	Diagonal element of the matrix of coupling potential (W)
o_f	Coupling element of the matrix of coupling potential (W)
λ	Coupling constant
κ	Potential energy gradient (tuning mode)
$\tilde{\lambda}$	Effective coupling
$\tilde{q_s}$	Shifted symmetric allylic stretch coordinates

Next, we expand ΔV, d and o_f (see Table 3.2) around $q_a = 0$ and $\tilde{q_s}(\phi) = 0$ up to first order. Since the ground and excited electronic state of fulvene are of different symmetry, the off-diagonal term o_f depends only on the anti-symmetric coordinate q_a and the diagonal term d depends only on the symmetric coordinate q_s. In Ref [110], it was found that for symmetry alllowed conical intersections, different symmetries of the electronic states, gives anti-symmetric off-diagonal terms (o_f) and symmetric diagonal terms. Thus, it suffices to determine the difference $(V_0 - V_1)$ of the adiabatic PESs as a function of each coordinates q_a and $\tilde{q_s}$. To determine the coupling constants, eq. (3.18) then leads, in first order, to [110]:

$$\begin{aligned}
\tilde{\lambda} &= \frac{\partial o_f}{\partial q_a}|_{q_a=0,\tilde{q_s}=0} = \frac{\partial \Delta V}{\partial q_a}|_{q_a=0,\tilde{q_s}=0} \\
\kappa &= \frac{\partial d}{\partial \tilde{q_s}}|_{q_a=0,\tilde{q_s}=0} = \frac{\partial \Delta V}{\partial \tilde{q_s}}|_{q_a=0,\tilde{q_s}=0},
\end{aligned}$$

with

$$\tilde{\lambda} = \frac{\partial \Delta V(\tilde{q_s} = 0)}{\partial q_a}|_{q_a=0} = \frac{1}{2}|\lambda| \tag{3.21}$$

and

$$\kappa = \frac{\partial \Delta V(q_a = 0)}{\partial \tilde{q_s}}|_{\tilde{q_s}=0} = \frac{1}{2} m_r(\omega_{se}^2 - \omega_{sg}^2) q_{sci}(\phi) - \frac{1}{2} m_r \omega_{se}^2 q_{s0}. \tag{3.22}$$

Where κ is the tuning parameter.
Therefore,

$$\begin{aligned} o_f &= \tilde{\lambda} q_a = \frac{1}{2}|\lambda| q_a \\ d &= \kappa \tilde{q_s}. \end{aligned} \tag{3.23}$$

The previous eqs. illustrate that, for symmetry allowed conical intersection, the coupling constants are the gradients of the difference $(V_0 - V_1)/2$ which determines the lifting of the degeneracy in the direction of either mode. According to Ref. [110], the diabatic potential matrix can then be written as:

$$W_{11} = \frac{1}{2}(V_1 + V_0) + \frac{1}{2}(V_1 - V_0)\frac{2\kappa \tilde{q_s}}{\sqrt{4\kappa^2 \tilde{q_s}^2 + \lambda^2 q_a^2}} \tag{3.24}$$

$$W_{00} = \frac{1}{2}(V_1 + V_0) - \frac{1}{2}(V_1 - V_0)\frac{2\kappa \tilde{q_s}}{\sqrt{4\kappa^2 \tilde{q_s}^2 + \lambda^2 q_a^2}} \tag{3.25}$$

$$W_{01} = \frac{1}{2}(V_1 - V_0)\frac{\lambda q_a}{\sqrt{4\kappa^2 \tilde{q_s}^2 + \lambda^2 q_a^2}}. \tag{3.26}$$

Finally, the matrix elements read

$$W_{11} = \frac{1}{2}(V_e + V_g) + \kappa[q_s - q_{sci}]\sqrt{\frac{\lambda^2 q_a^2 + (V_e - V_g)^2}{\lambda^2 q_a^2 + 4\kappa^2 (q_s - q_{sci})^2}} \tag{3.27}$$

$$W_{00} = \frac{1}{2}(V_e + V_g) - \kappa[q_s - q_{sci}]\sqrt{\frac{\lambda^2 q_a^2 + (V_e - V_g)^2}{\lambda^2 q_a^2 + 4\kappa^2 (q_s - q_{sci})^2}} \tag{3.28}$$

$$W_{01} = \frac{1}{2}\lambda q_a \sqrt{\frac{\lambda^2 q_a^2 + (V_e - V_g)^2}{\lambda^2 q_a^2 + 4\kappa^2 (q_s - q_{sci})^2}}, \tag{3.29}$$

where the potential energy surfaces V_g and V_e are given in eq. 3.6, the seam of the conical intersection, $q_{sci} = q_{sci}(\phi)$ is defined in eq. 3.8, and κ is given by eq. 3.22.

Figure 3.6 shows the adiabatic and diabatic potential energy surfaces as a function of the torsion angle ϕ and the anti-symmetric allylic stretch q_a for different values of q_s. In, figures 3.6 (a, b and c) we choose $q_s = q_{sci}(\phi = 0)$. In this case, the two adiabatic surfaces touch each other at the point $\phi = 0$, $q_a = 0$ (and, since the potential is periodic in ϕ, also at $\phi = -\pi$, $q_a = 0$ and $\phi = \pi$, $q_a = 0$). The coupling strength λ in all figures has the value of 16.2 eV/$\mathring{A}$ and the tuning parameter κ has the value of -5.2 eV/$\mathring{A}$.

3.4 Wavepacket Dynamics

In this section, we investigate the dynamics of nuclear wavepacket evolving on the potential energy surfaces induced by a z-polarized ultrashort laser pulse. The molecule is assumed to be preoriented with respect to the z-axis and considered to be in its vibrational and rotational ground state. The fulvene molecule is assumed to be initially localized in one potential well. A short laser pulse then excites the ground vibrational state of the electronic ground state to the electronic excited state potential energy surface and initiates the cis−trans isomerization. Such laser pulse is assumed to be short enough to induce a vertical transition, *i.e.* the excited state wavepacket is a copy of the ground vibrational state wave function. Because the initial wave function is quite distant from the CI, the interaction with the laser pulse is approximately the same in the adiabatic and diabatic representations. The initial nuclear wave function in the diabatic basis is then given by

$$\Psi^d(t=0) = \begin{pmatrix} \psi_1^d(t=0) \\ \psi_0^d(t=0) \end{pmatrix}, \tag{3.30}$$

where $\psi_0^d(t=0)$ and $\psi_1^d(t=0)$ are the diabatic wave functions at t=0. At this time (t=0), $\psi_0^d = 0$. The eigenvalues and eigenfunctions of the (uncoupled) ground electronic state V_g are calculated by numerically solving the time-independent Schrödinger eq. (see section 2.1.2) using the program package WAVEPACKET [116]. For the propagation of the wavepacket on the coupled diabatic surfaces we use the split-operator method, as implemented in the package WAVEPACKET [116]. We propagate the wave function on the diabatic PES according to

$$i\hbar\frac{\partial}{\partial t}\Psi^d = \left[\begin{pmatrix} T_N & 0 \\ 0 & T_N \end{pmatrix} + \begin{pmatrix} W_{11} & W_{10} \\ W_{01} & W_{00} \end{pmatrix}\right]\Psi^d, \tag{3.31}$$

In the following, we summarize the results of two sets of simulations for two-dimensional potential energy surfaces. First, we consider only the symmetric and anti-symmetric allylic stretch. Next, we consider torsion and anti-symmetric allylic stretch and simulate the wavepacket dynamics for cuts of $V_{1/0}$ for different values of $\tilde{q}_s$. The results of the two sets of simulations are shown and discussed in the following subsections. In all simulations the reduced torsional moment of inertia is 1.711 $m_H\mathring{A}^2$, the reduced mass for the torsion and for symmetric and anti-symmetric ring deformation parts of the kinetic energy operator is 6.28 and 13 u, respectively.

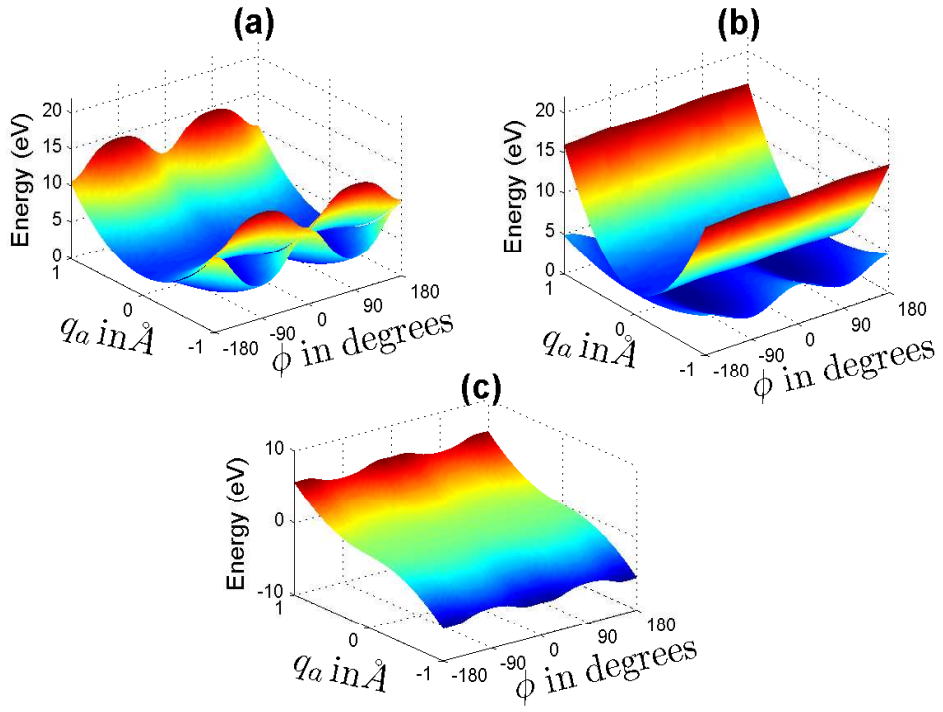

Figure 3.6: Two-dimensional potential energy surfaces for $q_s = q_{sci}(\phi = 0)$. The adiabatic potential energy surfaces $V_{1/0}$ are shown in (b). Figure (a) shows W_{11} and W_{00} for $q_s = q_{sci}(\phi = 0)$. The potential coupling W_{01} is shown in (c), ($\lambda = 16.2$ eV/Å).

3.4.1 Symmetric and Anti-symmetric Allylic Stretch Coordinates

Figure 3.7 sketches the dynamics assumed to take place along the $\tilde{q}_s$ coordinate. Here we investigate the efficiency and time scale of the radiationless decay for a two-dimensional potential consisting of the two vibrational modes q_a and $\tilde{q}_s$. Figure 3.8 shows the adiabatic and diabatic potential energy surfaces as a function of q_a and q_s for $\phi = 0$. The two potentials have a conical intersection at $q_a = \tilde{q}_s = 0$ as it can be seen in Figure 3.8(b). We start with simulating the wavepacket dynamics on the surfaces in Figure 3.8(a)-(c). In the following, we simulate the nuclear dynamics induced by a z-polarized ultrashort laser pulse. The preoriented molecules are assumed to be in their ground state with respect to q_a and $\tilde{q}_s$ coordinates. Moreover, they are located initially in their vibrational ground states. The symmetric

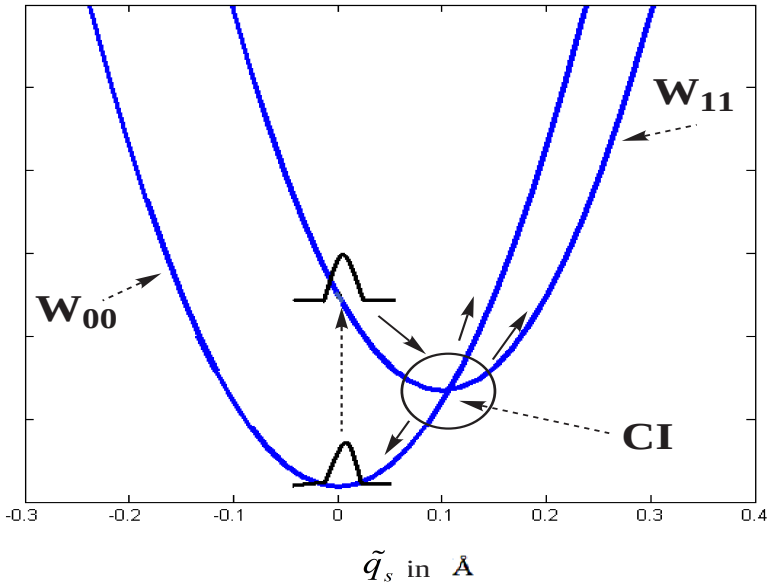

Figure 3.7: Sketch of one-dimensional scenario of the wavepacket dynamics along $\tilde{q}_s$ coordinates.

and anti-symmetric eigenfunctions are practically degenerate. We assume that the initial state is localized at $\tilde{q}_s$=0, i.e. is a superposition of the lowest symmetric and anti-symmetric ground state. For propagation of the wavepacket, the following parameters are used: simulations were carried out on a grid of 32 and 64 points ranging from -0.6 $\mathring{A}$ to 0.6 $\mathring{A}$ for the anti-symmetric allylic stretch (q_a) and from -1.5 $\mathring{A}$ to 1.0 $\mathring{A}$ for the symmetric allylic stretch ($\tilde{q}_s$) coordinates. The time steps for propagation were $t = 0.01$ fs. To investigate the accuracy of the grid, many simulations with different grid points for the two coordinates were carried out. The minimum number of grid points needed to describe the behavior of the wavepacket in the symmetric and anti-symmetric allylic stretch coordinates is 64 grid points. The effects of the conical intersection on the population of the two diabatic electronic states can also be seen in Figure 3.9. The red and green curves in this figure show the population of the ground and excited diabatic states, respectively. The population P^i_ν for the diabatic potential i is then defined by:

$$P^i = \int\int \mid \psi^d_i(q_a, \tilde{q}_s) \mid^2 dq_a d\tilde{q}_s \quad , i = 0, 1 \tag{3.32}$$

This figure shows, that at t $\approx$ 20 fs, more than 60% of the initial wavepacket decayed to the ground state. Repeated crossing of the conical intersection leads to an

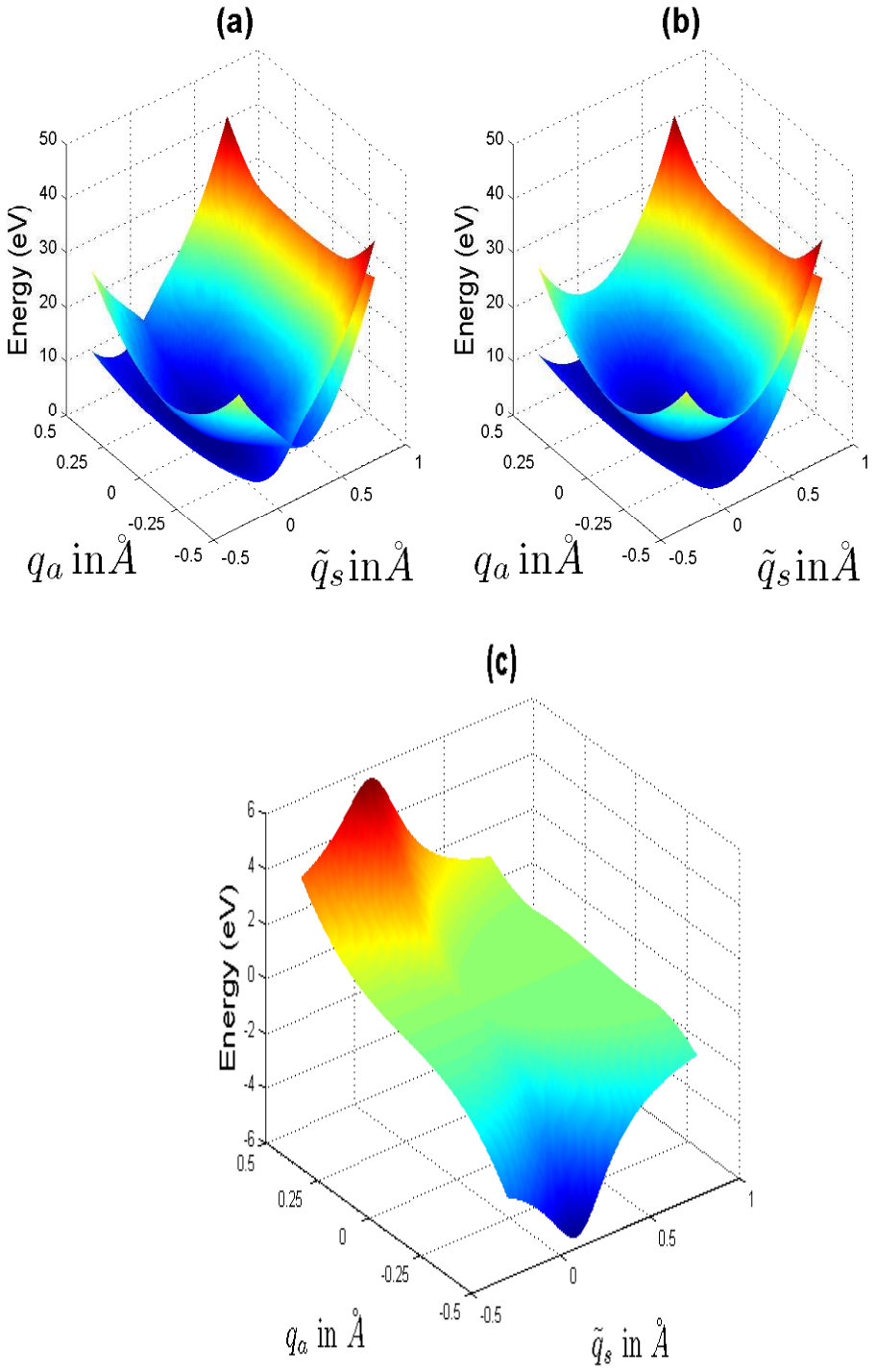

Figure 3.8: Two-dimensional potential energy surfaces for symmetric and anti-symmetric allylic stretch coordinates. Figure (a) shows W_{11} and W_{00}. The adiabatic potential energy surfaces are shown in (b) and the potential coupling W_{01} is shown in (c).

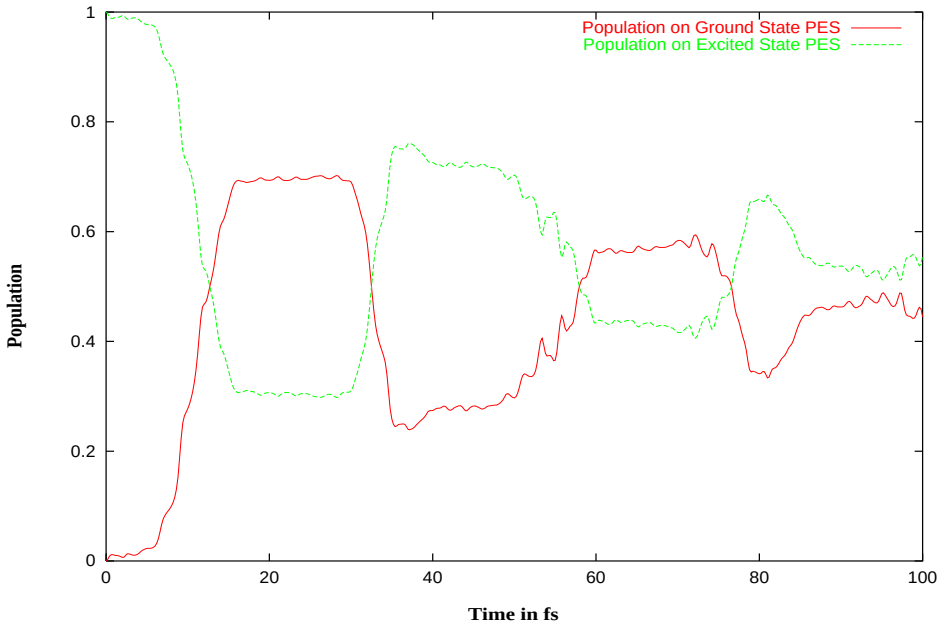

Figure 3.9: Population of the diabatic states. The red and green curves indicate the time dependence of the diabatic and adiabatic wave functions propagated on the ground and excited electronic with 64 grid points for the symmetric and anti-symmetric allylic stretch coordinates ($\lambda = 10.8$ eV/$\mathring{A}$).

oscillation of the population between the two electronic states. One can distinguish between periods where the wavepacket is almost not affected by the coupling (e.g $t \leq 5$ fs and 20 fs $\leq t \leq 30$ fs), and periods with extensive population transfer (e.g 10 fs $\leq t \leq 20$ fs). Comparison with Figure 3.11 shows that the wavepacket is passing the conical intersection during those periods. Since the wavepacket at more delocalized at later times ($t \leq 40$ fs), those features become less clear. Figure 3.10 shows the autocorrelation function

$$Au(t) = |\langle \Psi(0)|\Psi(t)\rangle|^2 \tag{3.33}$$

which also displays the time-evolution of the excited state wave function. As this figure illustrates, a radiationless decay occurs after $\approx$ 10-15 fs. It also shows that the autocorrelation function has peaks every $\approx$ 20 fs which is the vibrational period for the motion along $\tilde{q}_a$ and q_s coordinate (see Table 3.1). In fact, the motion of the wavepacket is mainly along the $\tilde{q}_s$ coordinates with vibrational period of $t_{vib} = \frac{2\pi}{\omega_{se}}$. A stepwise population transfer can be observed whenever the wavepacket crosses the CI region. Figure 3.11 shows snapshots of the time evolution for the vibrational ground state wave function, on the ground and excited electronic state PESs for

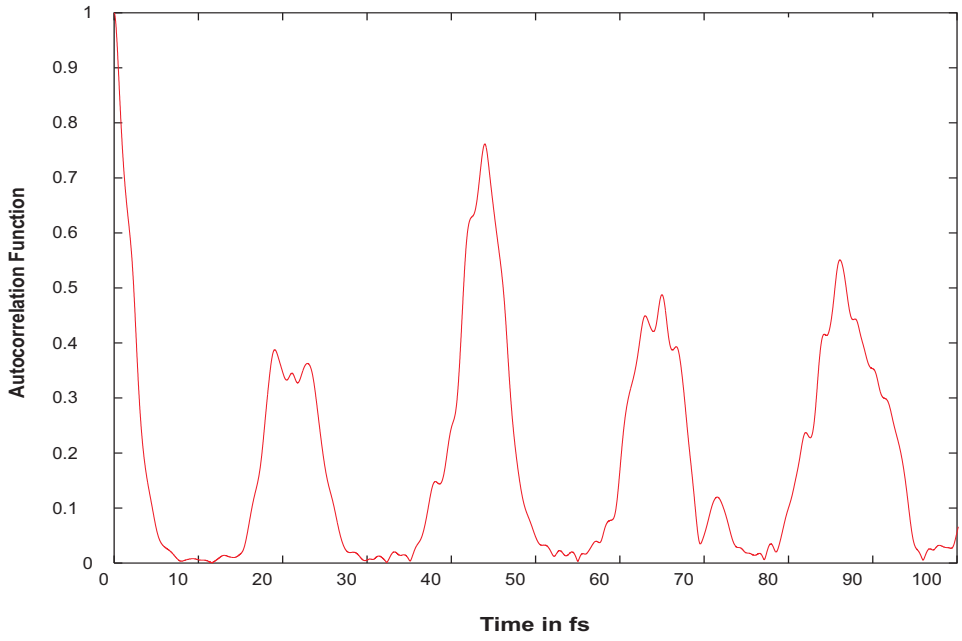

Figure 3.10: The autocorrelation function of the diabatic states with 64 grid points for the symmetric and anti-symmetric allylic stretch coordinates ($\lambda = 10.8$ eV $/\mathring{A}$).

$\lambda = 10.8$ eV$/\mathring{A}$.

Initially, the wavepacket is localized at $\tilde{q}_s$=0 $\mathring{A}$ and q_a =0. The amplitude of the wavepacket at the ground electronic state PES is zero. The wavepacket on the excited PES starts moving towards the conical intersection. The wave function on the ground state PES has a node for the anti-symmetric allylic stretch $q_a = 0$. This can be explained by the fact that the diabatic coupling W_{01} is zero for $q_a = 0$. As the excited state wavepacket approaches the conical intersection ($t = 10$ fs), considerably more population is transferred to the ground state. After $t = 20$ fs, the wavepacket passed the conical intersection for another time. Now, only the central part of the initial wave function remains on the excited PES. The last row in Figure 3.11 show the wavepacket at $t = 43$ fs. Here we can see that part of the ground state wave function is transferred back to the excited PES. During the whole evolution the wavepacket remains in the conical intersection region and tends to be more localized on the excited state PES while it is spread more on the ground state PES around the CI region. Note that here, we have used arbitrary value of the coupling parameter λ for the model potential. A more accurate description of the wavepacket dynamics of fulvene requires the determination of λ from quantum chemical ab initio data (see Ref. [63]).

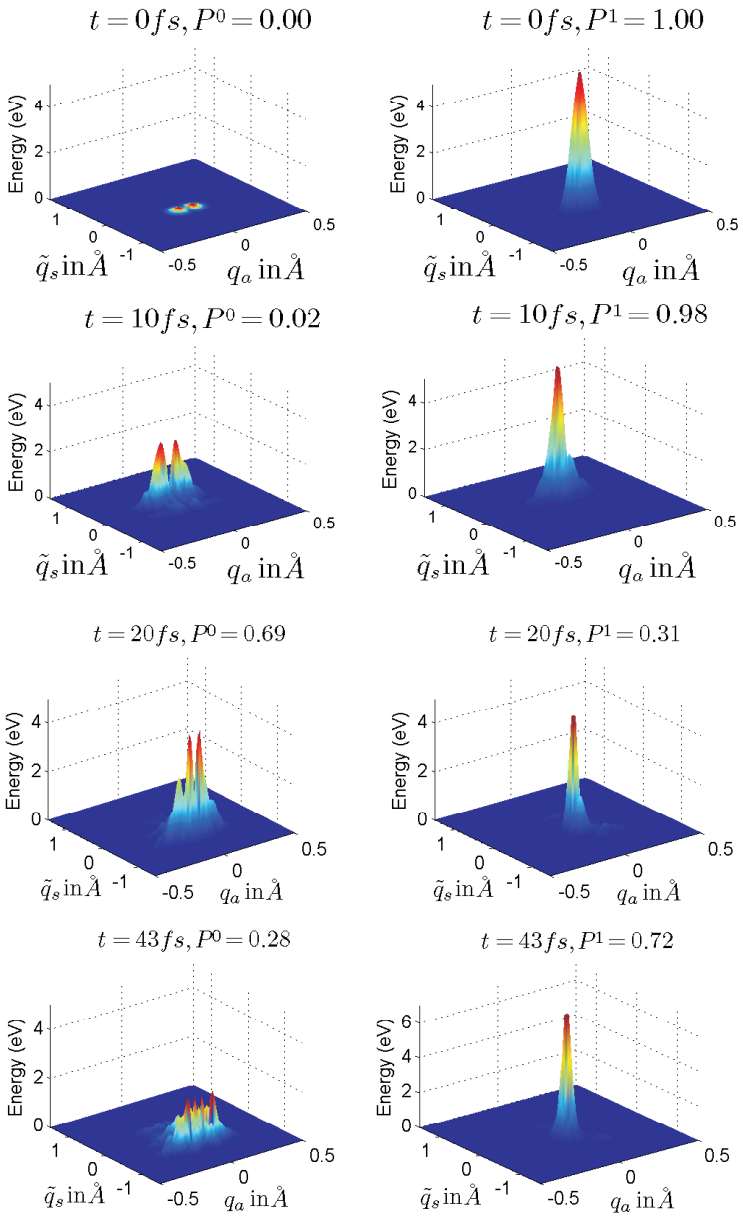

Figure 3.11: Snapshots of the time evolution of the diabatic wave functions on the electronic ground and excited states potential energy surfaces with 64 grid points for the symmetric and anti-symmetric allylic stretch coordinates ($\lambda = 10.8$ eV/$\mathring{A}$).

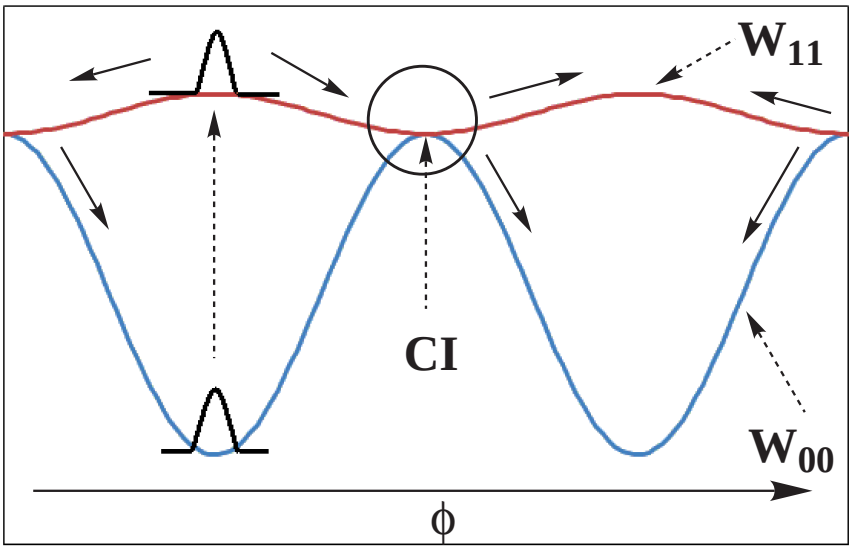

Figure 3.12: Sketch of one-dimensional scenario of the wavepacket dynamics along the torsion (ϕ) coordinates

.

3.4.2 Torsion and Anti-symmetric Allylic Stretch Coordinates

Figure 3.12 sketches the dynamics assumed to take place along the ϕ coordinates.

Here we investigate the efficiency and time scale of the radiationless decay for a two-dimensional potential consisting of the two vibrational modes q_a and ϕ. The potential energy surfaces as a function of the torsion angle ϕ and the anti-symmetric allylic stretch q_a for different values of $\tilde{q}_s$ are shown in Figure 3.6. In Figures 3.6(a)-(c), $\tilde{q}_s$ is chosen such that the potential energy surfaces just touch at $\phi = 0$. For propagation of the wavepacket, the following parameters are used: simulations were carried out on a grid of 32, 64, 128 and 256 points ranging from -π to π for the torsion coordinates. For the anti-symmetric allylic stretch coordinates, grids of 32, 64 and 128 points ranging from -0.5 $\mathring{A}$ to 0.5 $\mathring{A}$ were used. The time steps for the propagation were $t = 0.01$ fs. We start with simulating the wavepacket dynamics on the surfaces in Figure 3.6(a)-(c).

In the following, we simulate the nuclear dynamics induced by a z-polarized ultrashort laser pulse. The preoriented molecules are assumed to be in their ground state with respect to anti-symmetric allylic stretch (q_a) and torsion (ϕ) coordinates. Moreover, they are located initially in their vibrational ground states. Since fulvene has a CH_2 group with two identical protons, the adiabatic electronic ground state has two equivalent minima at ϕ=-90 and ϕ=90 degrees (see Figure 3.6(a),(b)). The lowest adiabatic eigenfunctions are a doublet of symmetric and antisymmetric functions. The symmetric and anti-symmetric eigenfunctions are practically degenerate. We assume that the initial state is localized in the left potential well at ϕ=$-90°$, i.e. is a superposition of the lowest symmetric and anti-symmetric ground torsional state. The 2D rovibrational eigenfunctions were obtained using the FGH method, see section 2.3.1, using the QMBOUND program implemented in the WAVEPACKET package [116]. To find the size of the grid necessary to obtain reliable results for

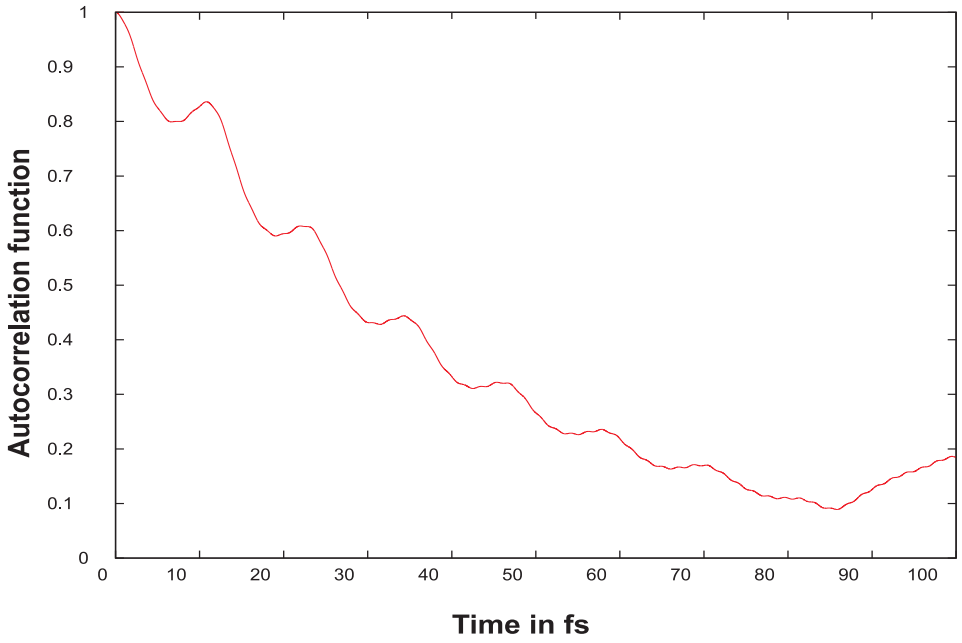

Figure 3.13: The autocorrelation function of the diabatic states propagated on the torsion and anti-symmetric allylic stretch coordinates. The calculations were carried out on a grid of 128 points for each coordinate ($\lambda = 16.2$ eV/$\mathring{A}$).

the wavepacket dynamics, a grid convergence test was carried out. The largest grid we have tried so far was 128 $\times$ 128 points and 256 $\times$ 64 points for torsion and anti-symmetric allylic stretch coordinates, respectively. Simulations with different grids showed that for times until 100 fs, a grid with 128 $\times$ 128 points is sufficient, longer time evolution requires larger grid. In this report, we will report the results

for the calculcarried out using the finer grid (128 × 128 points for the torsion and anti-symmetric allylic stretch coordinates). Figure 3.13 show an overall decay of autocorrelation function during the first 100 fs related to torsional motion. Figure

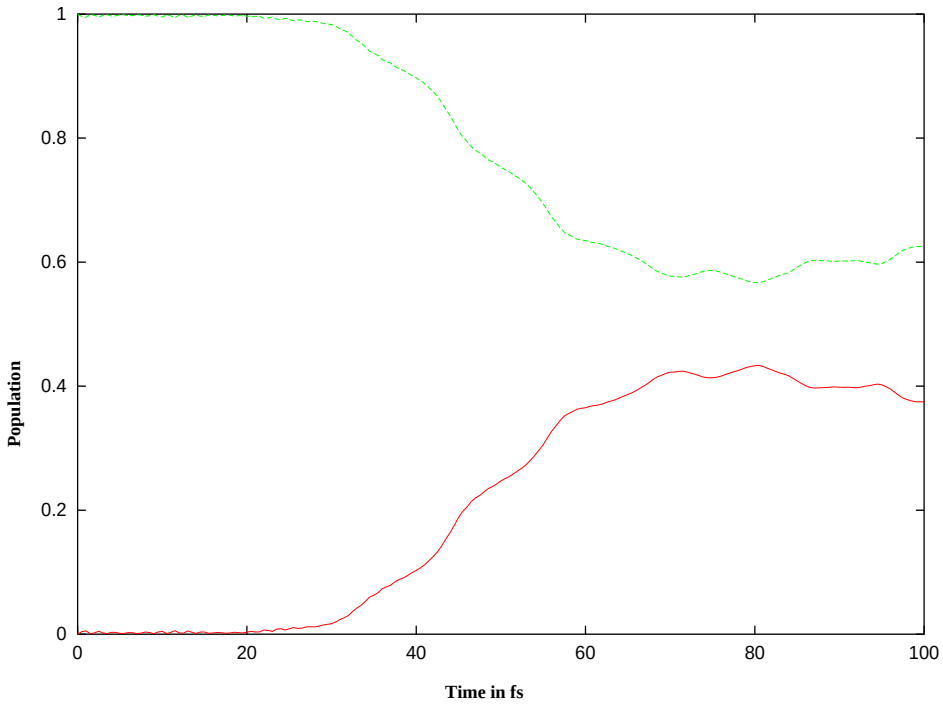

Figure 3.14: The population of the time evolution of the diabatic states propagated on the torsion and anti-symmetric allylic stretching coordinates with a grid of 128 points for each coordinates (λ = 16.2 eV/$\mathring{A}$ and ϕ = 0°). The green curve indicates the time dependence of the diabatic states propagated on the excited electronic states while the red curve indicates the time dependence of the diabatic states propagated on the ground electronic states.

3.14 shows population of the states on the ground and excited states PESs for $\tilde{q}_s = 0$ and a grid of 128 points for each of q_a and ϕ coordinates. From this figure, one can distinguish between periods where the wavepacket is almost not affected by the coupling ($t \leq$ 20 fs and 70 $\leq$ t $\leq$ 80 fs), and periods with large population transfer(40 $\leq$ t $\leq$ 70 fs). The wavepacket is passing the conical intersection during those periods. In the period between (70 $\leq$ t $\leq$ 90) fs, the wavepacket becomes more or less equally partitioned between the two PESs. This figure shows that a radiationless decay takes place after t $\approx$ 50 fs. Since the CI is located at ϕ=0 and the initial wavepacket is positioned at ϕ=-π/2, the previous finding shows that a torsion of the CH_2 group by 45 degrees needs approximately 50 fs. Accordingly, the radiationless

decay due to torsion is slower than the radiationless decay related to vibrational motion shown in the previous section. Figure 3.15 shows snapshots of the time-evolution of the diabatic wave functions, carried out on a grid of 128 × 128 points and ϕ=0. The wavepacket moves slower on this coordinates system than it does on the symmetric and anti-symmetric allylic stretch coordinates. The amplitude of the wavepacket at the ground state PES is zero. The wavepacket on the excited state PES starts moving along the torsion coordinates until ($t = 7fs$). Actually, the motion observed at initial times is only broadening of excited state wavepacket along torsional coordinate till t ≈ 30 fs. During this period, the wavepacket tends to be more localized on the excited state PES. At times t > 30 fs, a radiationless decay takes place mainly at the CI region, where ϕ=0 and 180 degrees, which leads to the transformation of the wavepacket to the ground state. After t ≈ 30 fs, the wavepacket is also broadening along q_a coordinates. After crossing the conical intersection region, larger parts of the wavepacket are transferred to the ground state PES and the wavepacket tends to be more delocalized on both PESs. One can notice the node of ground state wavepacket at q_a=0 where the potential W_{01} is close to the CI ($W_{01} \approx \lambda \times q_a = 0$ for q_a=0) which leads to the observed node.

Simulations with a grid of 512 points for the torsion coordinates and 64 points for the anti-symmetric allylic stretch coordinates should be considered. Furthermore, using larger grid for the anti-symmetric allylic stretch coordinates should also be considered. The next step on improving the grid would be to use a grid of 256 points for the torsion coordinates and 128 points for the anti-symmetric allylic stretch coordinates. However, moving to a larger grids with the *qmbound* program, is time consuming and may be one should consider finding the wave functions for the different PES using another method.

3.5 Summary of these Simulations and Outlook

Radiationless decay due to vibration along symmetric allylic stretching coordinates, which takes place after t ≈ 10-15 fs, is much faster than the radiationless decay along the torsion coordinates that takes place after t ≈ 50 fs. These results have been confirmed in later studies on more accurate three dimensional ab-initio PES where it was been shown that after vertical excitation, the fast radiationless decay along the symmetric allylic stretching coordinates prevents the slower torsion of the CH_2 group (see Ref [63]). Recently, some dynamical studies has been carried out on the fulvene molecule [63, 64, 65]. The authors in Ref. [63, 64, 65] proposed a wavepacket interferometric scheme for the separation of different nuclear spin iso-

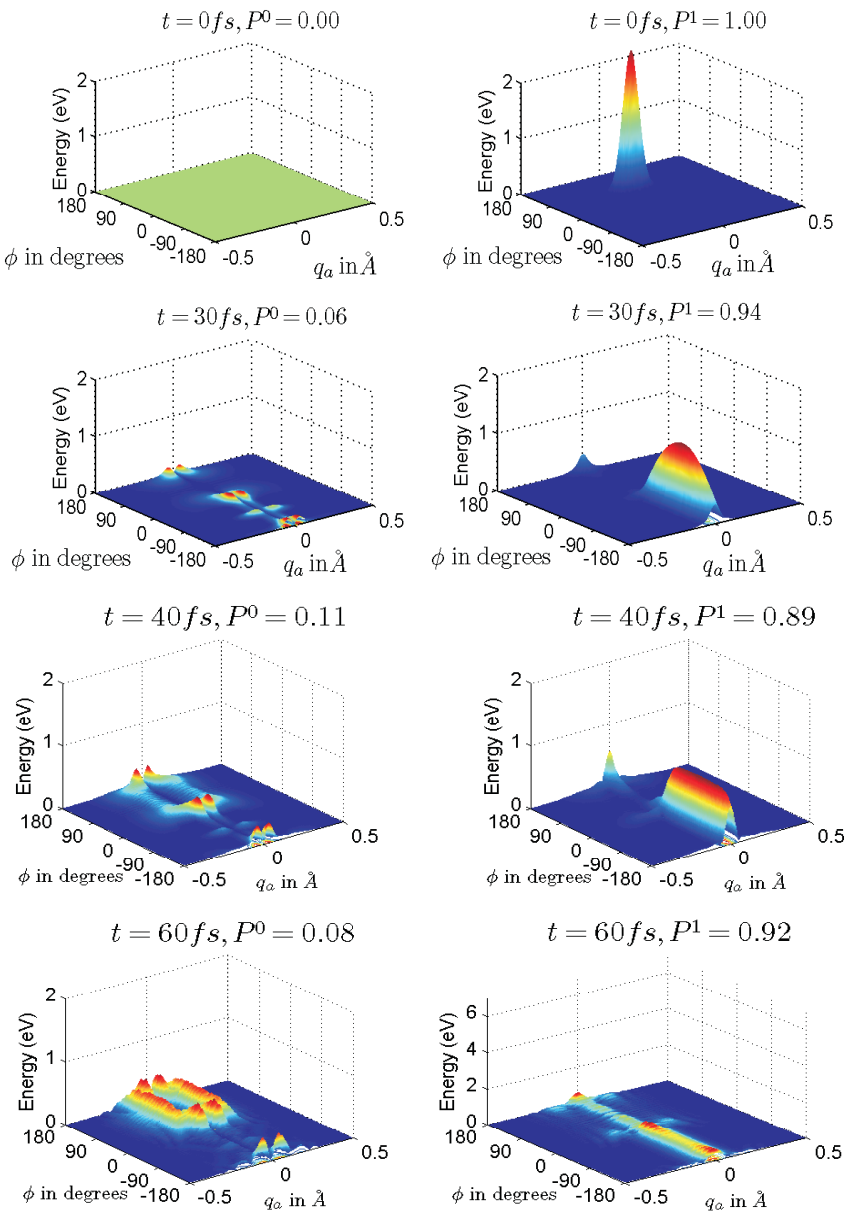

Figure 3.15: Snapshots of the time evolution of the diabatic wave functions on the electronic ground and excited states potential energy surfaces with 128 grid points for the torsion and anti-symmetric allylic stretch coordinates ($\phi = 0°$ and $\lambda = 16.2$ eV/Å).

mers. They have investigated the separation of model para- and ortho-fulvene where they used simple Gaussian pulses. The authors applied wavepacket interferometry, making use of the difference in wavepacket dynamics of the two isomers to affect separation. Furthermore, they have pointed to, the conceptually interesting but barely investigated up to now, the symmetry-induced coupling of torsion and nuclear spin modes of molecules where they have used the fulvene molecule as a model.

Chapter 4

Photoinduced Quantum Dynamics in 4-(methyl-cyclohexylidene)-Fluoromethane (4MCF)

In this chapter the torsional dynamics around the C=C bond competing against HF photodissociation dynamics are explored for the molecule 4-(methyl-cyclohexylidene)-Fluoromethane (4MCF). The chapter starts with an introduction and follows with a discussion of a quantum chemical two-dimensional PESs (2D-PES) that include the twisting and HF-elimination coordinates. Later, the dynamics of rotation and dissociation are demonstrated on non-adiabatically coupled PESs. Finally, an outlook for control is given.

4.1 Background

Molecules consisting of the same number and types of atoms with the same connectivity between the atoms can form stereo isomers, i.e. isomers that differ from each other by the spatial distribution of their atoms. If two stereo isomers are mirror images of each other then they are called enantiomers. Such isomers have the same physical properties except for the fact that they rotate the direction of the polarization of light by the same angle but in opposite directions. A molecule that is not

superimposable on its mirror image is *chiral*. A Chiral center, which is a most commonly a carbon atom with four different substituent, is a necessary and sufficient condition for the existence of enantiomers [156]. The feature that is most often the cause of chirality in molecules is the presence of an asymmetric carbon atom [156]. If any atom or group on the asymmetric carbon is on the right side, that asymmetric carbon is called as "R"; if any atom or group is on the left side, the asymmetric carbon is designated as "S" [156]. The 4MCF molecule is a fluoroethylene derivative with two R/S enantiomers connected by a torsion around the C=C double bond as it is shown in Figure 4.1. The opposite enantiomer can be formed by exchanging the substituents either on the terminal carbon of the ethylene group or on the ring carbon atom at the 4-position. In this thesis, we are concerned with obtaining the respective opposite chiral form obtained from exchanging the hydrogen and fluorine atoms by rotation around the C=C double bond, see Figure 4.1. For this ability, the 4MCF was proposed as a model system for a light-induced chiral molecular switch or a molecular rotor [24, 69, 70]. All these devices are originated from the posibility of 4MCF to switch between the R/S enantiomers efficiently, triggered by a specific laser or sequence of laser pulses especially designed for this purpose.

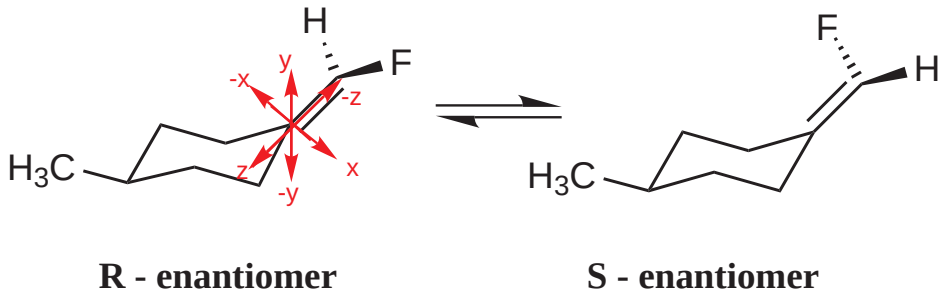

Figure 4.1: The R/S isomerization of 4MCF molecule. The arrows show the orientation of the 4MCF in the space fixed coordinate system.

In ethylene, several CIs which involve the torsion around the double bond allow for a very fast relaxation from the lowest bright electronic excited state (of $\pi\pi^*$ character) to the ground state [157, 158, 159]. A CI between the S_1 (V state) and S_0 (N state) exist at a twisted geometry with pyramidalization at one of the carbon atoms. It has been indicated that this twisted pyramidalized geometry is the main channel for deactivation to the ground state [160]. Besides isomerization, ethylene as well as ethylene derivatives, can undergo photoinduced dissociation. It has been observed experimentally that both atomic and molecular hydrogen are

eliminated in ethylene after irradiation [161, 162]. In the same way, elimination of halogen derivatives has been detected in difluoroethylenes [163, 164, 165] or vinyl chloride [166, 167]. Photodissociation dynamics in ethylene [168], fluoroethylene [169, 170], difluoroethylenes [171, 172, 173] and vinyl chloride [174, 175] have also been investigated theoretically. Analogous to the degeneracy points found for fluo-

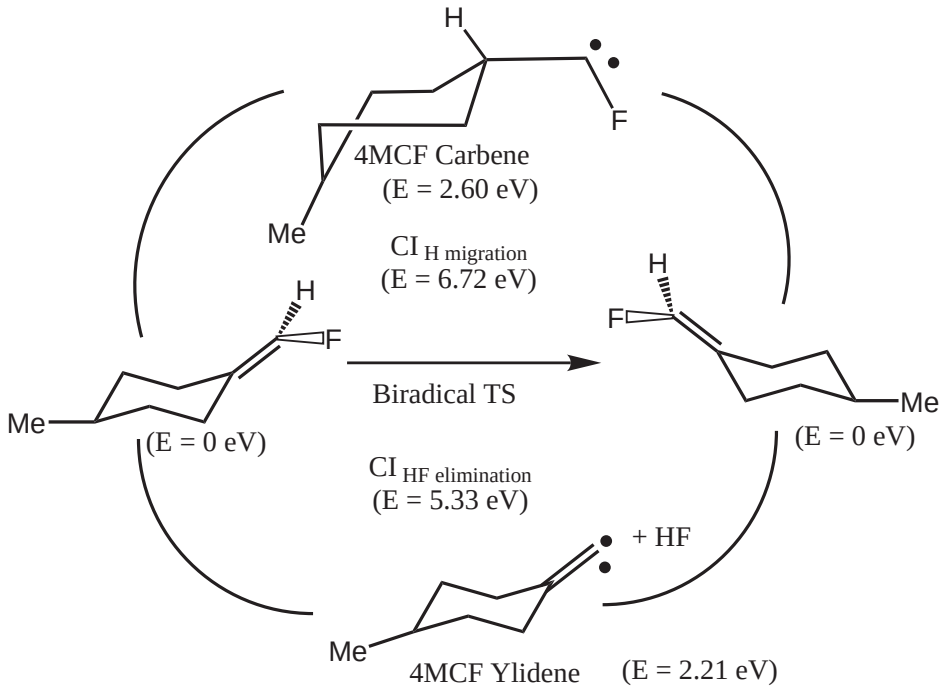

Figure 4.2: 4MCF loops, adapted from Ref. [68].

roethylene [66], CIs involving torsion, pyramidalization, and H-atom migration have been reported for 4MCF [67]. Additionally, a new CI associated with the elimination of HF has also been located in 4MCF [68] via applying the LH loop method [25, 29, 30, 142, 143] and using a large active space (CASSCF(12,12)/cc-pVDZ), including 12 electrons in 12 orbitals (the $\pi\pi^*$ orbital pair and 5 σ pairs orbitals). In Ref. [68], the phase inverting LH loops containing CIs [26] are constructed for the 4MCF system by using reaction coordinates, see Figure 4.2. One loop is analogous to that enclosing the well-known ethylene CI for H-migration. Its anchors are the two isomers obtained upon torsion by 180° around the C=C double bond and the carbene formed by H-atom migration [160, 176]. A second CI, of noticeably lower energy, was found by replacing the carbene by the HF elimination products (see Figure 4.2). Therefore, the second CI is potentially more important in the photochemistry of this type of molecules. The two CIs mentioned above are discussed in

detail in Ref. [68].

There, it is argued that the energy of the HF-elimination CI is expected to be lowered in polar solvents because of the large dipole moment at geometries near the CI, whereas the energy of the covalent-type CI (associated with torsion and H-migration loop) should not be strongly affected by the solvent. In [68] it was concluded that in liquid solutions, irradiation should yield generally the chiral isomer upon C=C rotation. However, in gas phase passage through the new CI is supposed to lead to dissociation. In this case, the predicted main product is the strongly vibrationally and rotationally excited HF molecule. On the other hand, crossing through the covalent CI is not expected to yield HF as a main product. Thus, the two CIs may be distinguished by the nature of the products obtained in the gas phase. So far, dynamical studies on 4MCF have only considered the torsion and pyramidalization coordinates [24, 69, 70]. To eventually use the 4MCF as molecular rotor, HF elimination is a non-desired competing mechanism that should obviously be avoided. This study considers explicitly the torsional dynamics around the C=C bond along with the competing HF photodissociation dynamics in gas phase.

4.2 Definition of the Model System

The orientation of the 4MCF molecule is shown in Figure 4.1. The 4MCF molecule is oriented such that the C=C double bond lies along the z-axis and the F and the H atom lie in the xz-plane. The molecule has a chiral axis defined by the C=C double bond. The C_2 atom is at the origin of coordinates while C_1 lies in negative z-direction.

4.2.1 Reaction Coordinates

When treating polyatomic molecules and chemical reactions, it is particularly common to make the choice of coordinates so as to simplify the mathematical formulation of the Hamiltonian [177]. In such model coordinates, the position coordinates (x, y and z) are replaced by their relative positions, with respect to some fixed point, (Δx, Δy and Δz) and by the vector to their center of masses. The two competing reactions that are investigated in this study for the 4MCF are the photoisomerization around the double bond producing the R/S enantiomers and the photodissociation of HF. Figure 4.2 shows the two CIs mediating both reactions. Both CIs are twisted

around the C_1=C_2 at 90°. In Ref. [68], it was observed that the HF-elimination CI has a relatively long C–F bond. To describe the photoisomerization and photodissociation reactions, a simple model consisting of two reaction coordinates was used to build the PES. In this model, the molecule is assumed to be pre-oriented as shown in Figure 4.1. In building the PESs, all degrees of freedom of the molecule are

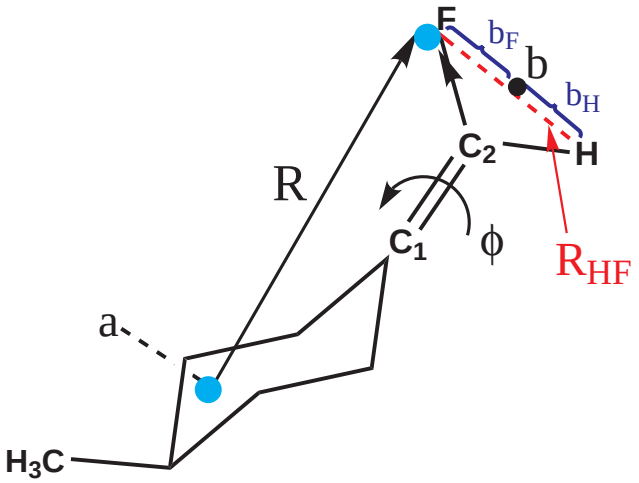

Figure 4.3: Twisted minimum geometry of 4MCF (ϕ = 90°, R=3.4 $\mathring{A}$) with the parameters used to define the photoisomerization and photodissociation reactions coordinates. ϕ is the torsional angle. The vector R is defined from the center of mass of the hydrocarbon moiety "a" to the center of mass of the HF fragment (indicated by blue circles). The point "b" indicates the intersection of the line connecting H and F atoms (the R_{HF} distance) with the z-axis.

kept frozen except the coordinates responsible for the isomerization and dissociation reactions to take place, these are:

1. The torsion angle (ϕ) that describes the rotational motion around the C=C double bond. For $\phi = 0°$, H and F lie in the xz-plane and the molecule has C_s symmetry. This is also true for $\phi = 180°$.

2. The distance (R) between the center of mass of the hydrocarbon fragment and the center of mass of the HF fragment, see Figure 4.3. The dissociation motion can be represented by the $\vec{R}$ vector that connects the center of masses of the HF fragment, which is almost located at the much heavier F atom, and the center of mass of the hydrocarbon part, located inside the hydrocarbon ring.

It should be noticed that the distance between H and F atoms is expected to decrease as the HF fragment dissociates away from C_2 forming the HF molecule. However, in this study, this is neglected as a first approach. Such approximation has the advantage of facilitating the calculations and making the model Hamiltonian simpler. Accordingly, the scenario described is the rotation of the HF fragment around the C=C double bond (rotation coordinate) while simultaneously moving away from the hydrocarbon fragment in the direction of the vector $\vec{R}$ (dissociation coordinate). The rotation of HF fragment around the C=C double bond affects only the coordinates of the H and F atoms. The change in the Cartesian coordinates as a result of changing the torsion angle (ϕ) can be described by the following equations:

$$x_F = -x_{F0}\cos(\phi), \tag{4.1}$$
$$y_F = -x_{F0}\sin(\phi), \tag{4.2}$$
$$x_H = -x_{H0}\cos(\phi), \tag{4.3}$$
$$y_H = -x_{H0}\sin(\phi). \tag{4.4}$$

Here, x_H, x_F, y_H and y_F are the x and y coordinates of the H and F atoms as they change with the torsion angle ϕ, respectively. x_{H0}, x_{F0}, y_{H0} and y_{F0} are the coordinates of the H and F atoms at the twisted minimum geometry (ϕ=90°, R = 3.5 $\mathring{A}$), see Figure 4.3. In the latter figure, the point b is pointing to the intersection of the line connecting the H and F atoms (the R_{HF} distance) with the z-axis. The distance b_H and b_F in 4.3 are the distances between b and each of H and F atoms, respectively. The $b_F(q)$, $b_H(q)$ and R_{HF}(q) distances are represented by the following three-dimensional vectors:

$$\vec{b}_F(q) = F(q) - b(q), \tag{4.5}$$
$$\vec{b}_H(q) = H(q) - b(q), \tag{4.6}$$
$$\vec{R}_{HF}(q) = F(q) - H(q), \tag{4.7}$$

The vector $\vec{R}$ is defined as

$$\vec{R}(q) = F(q) - a(q), \tag{4.8}$$
$$\tag{4.9}$$

where (q) indicates the cartesian coordinates in the x, y and z directions, $F(q)$ and $H(q)$ are the coordinates of the F and H atoms and $a(q)$ indicates the coordinates of the center of mass of the hydrocarbon-fragment.

As the HF fragment rotates around the C=C double bond, the length of the vector $\vec{R}(q)$ changes with ϕ (for a fixed distance R). Introducing a unitary vector $u\vec{R}(q)$ ensures that the vector $\vec{R}(q)$ is kept normalized relative to its value at the

twisted minimum geometry ($\phi = 90°$, R = 3.5 $\mathring{A}$). Then, the change in the coordinates of the H and F atoms due to dissociation along the vector $\vec{R}(q)$ ($H_d(q)$ and $F_d(q)$, respectively) is given by

$$H_d(q) = H(q) + u\vec{R}(q)\ (|R|\ -\ |R_0|)\,, \tag{4.10}$$

$$F_d(q) = F(q) + u\vec{R}(q)\ (|R|\ -\ |R_0|)\,, \tag{4.11}$$

where $|R_0|$ is the length of the vector $\vec{R}(q)$ at the twisted minimum geometry (ϕ=90°, R=3.5 $\mathring{A}$) and $|R|$ is the length of the vector $\vec{R}(q)$ at a given R distance and torsion angle ϕ.

4.2.2 Computational Details

The CI of the HF elimination reaction was found by Haas et al [68] using C_s symmetry and the CASSCF(12,12)/ccpVDZ level of theory, as implemented in the GAMESS program suite [101]. Figure 4.4 illustrates the active space used in these calculations, which consist of π and π^* orbitals on the double bond in addition to the σ and σ^* orbitals of the C–C, C–H, C–F and H–F bonds. The ground/excited state energy gap of the CI for this geometry is 0.154 kJ/mol. The most important geometrical parameters of this CI are shown in Figure 4.5(a). Because GAMESS software has no facilities to calculate the nonadiabatic coupling terms, the 2D-PES for 4MCF photodissociation was calculated using MOLPRO software [52] which has such facilities.

The PESs should contain the geometry of reactants, products and the HF-elimination CI. Since the CI is the most sensitive geometry for changes in the wave function, the CI geometry was chosen as the starting geometry for determining the active space in first place. Finding a suitable active space is an essential step. Since we could not obtain an active space analogous to that used for locating the CI and the stationary points in the 4MCF loop employed by Haas et al [68] a systematic search for an analogous appropriate active space was carried out. Several trials were made to achieve this purpose. We started using a CASSCF(8,9) that includes p-orbitals on C and F, s-orbital on H, π and π^* orbitals on the double bond, in addition to σ and σ^* orbitals to describe C-H, C-F and H-F bonds. This active space is illustrated in Figure 4.6. Using this active space the energy gap between the ground and excited states (ΔE), for the geometry shown in Figure 4.5(a) is 0.170 kJ/mol. Using larger active space does not decrease this value. Next, some

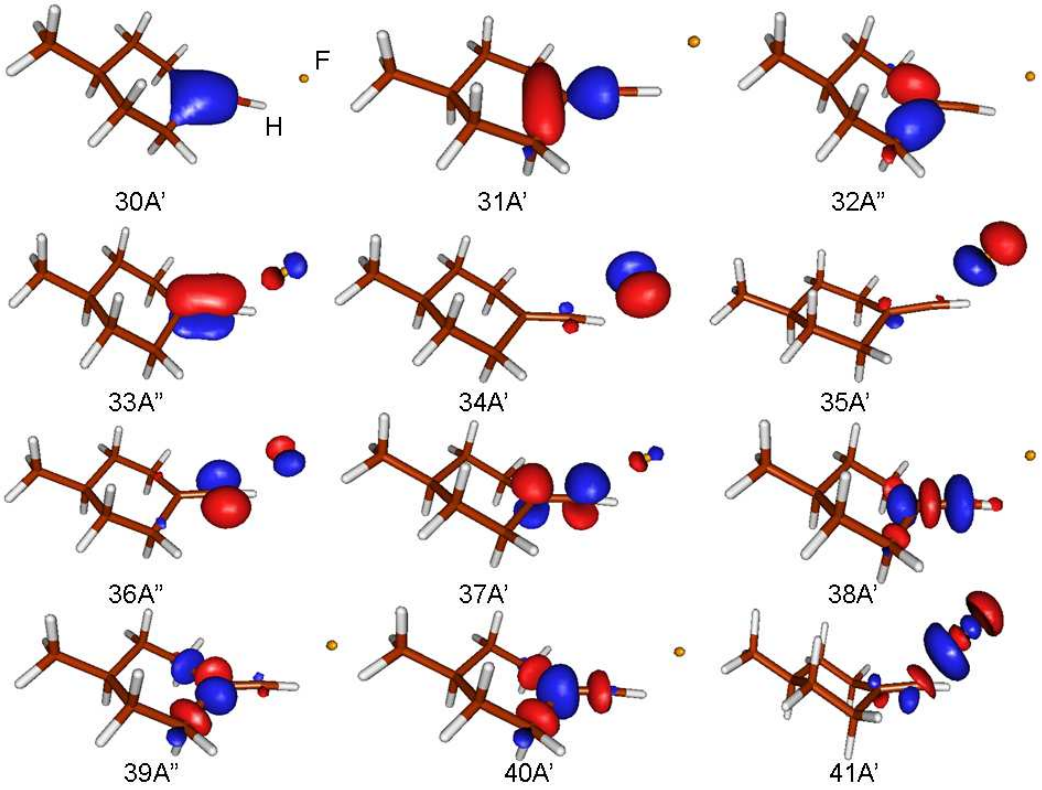

Figure 4.4: Active space from GAMESS - CASSCF(12,12)/cc-pVDZ. The position of the H and F atoms are sketched on 30A' orbital.

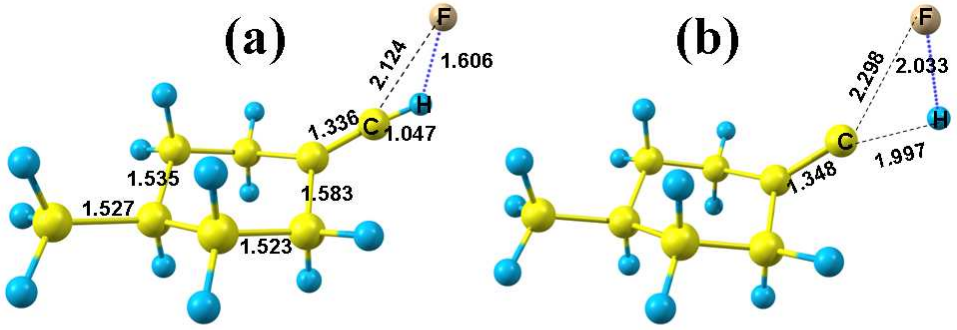

Figure 4.5: Important geometrical parameters of the CI obtained from (a) GAMESS and (b) MOLPRO calculations at the indicated level of theory. ΔE indicates the energy gap between the ground and excited states (S_0 and S_1, respectively). Bond lengths and distances are given in $\mathring{A}$.

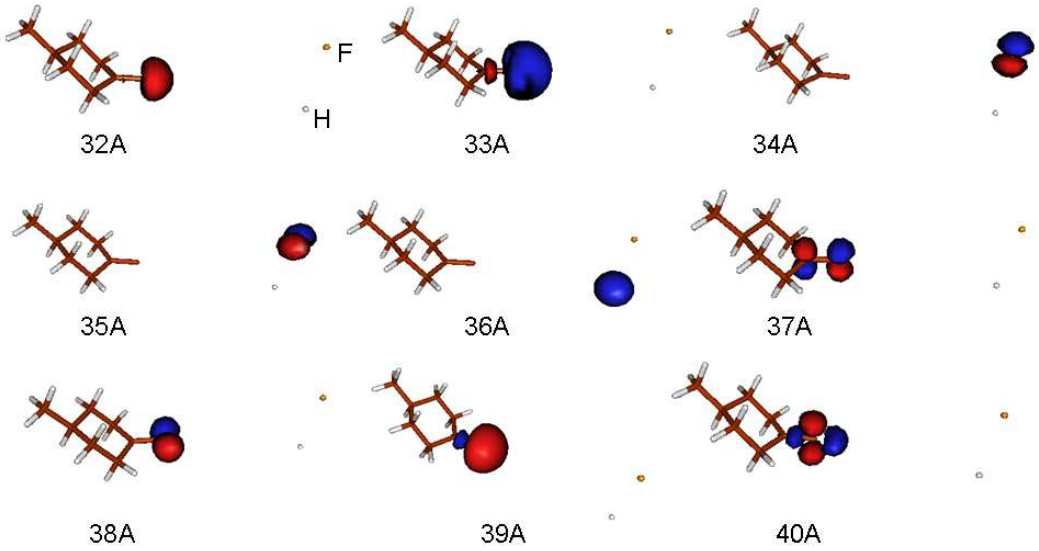

Figure 4.6: Active space from MOLPRO - CASSCF(8,9)/cc-pVDZ. The position of the H and F atoms is sketched on the 32A orbital.

changes to the starting geometry are done to improve the active space. For such purpose, we started from the twisted minimum geometry ($\phi = 90°$, R=3.5$\mathring{A}$) and then used R distance of 6.0 $\mathring{A}$ to obtain the active space suitable to describe the 4MCF Ylidene and *separated* HF moiety. Next, the R distance was decreased in a series of successive calculations to $5.5, 5.0, 4.9, 4.7\mathring{A}$ ending at the R distance of the CI ($4.6\mathring{A}$). The values of ϕ angle was kept equal to that of the CI geometry (90°) in all the previous calculations. The final geometry obtained from these series of the calculations is shown in Figure 4.5(b). In this geometry, the R_{HF} distance was equal to that of the minimum geometry ($\phi = 0°$, R=3.5 $\mathring{A}$). As the HF and hydrocarbon fragments approach each other, the orbitals in the active space changed to reflect this enhanced bonding characteristic. Then, the number of orbitals was decreased to eight orbitals instead of nine. Figure 4.7 shows that the p and s atomic orbitals on the H and F atoms (orbitals 34A, 35A and 36A in Figure 4.6), are now combined in bonding orbitals for the H–F, C-H and C–F bonds (see Figure 4.7, orbitals 34A, 36A and 38A). The relatively smaller CASSCF(8,8), illustrated in Figure 4.7, will reduce the cost of building the PESs. Therefore, it will be used to carry out the rest of the calculations. The energy gap of the CI geometry (ΔE) obtained using this (8,8) active space is 0.096 kJ/mol, see Figure 4.5(b), indicating that this final wave function can describe appropriately the CI.

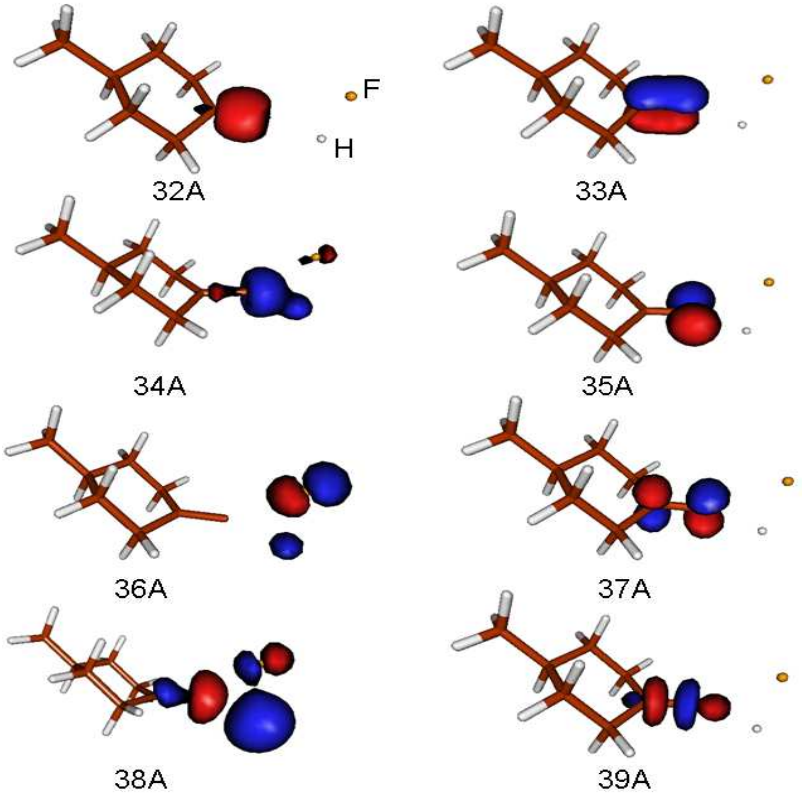

Figure 4.7: Active space from MOLPRO - CASSCF(8,8)/cc-pVDZ. The position of the H and F atoms is sketched on the 32A orbital.

4.3 Quantum Chemical Results

The present study is the first step towards investigating the dynamics of the 4MCF R/S photo-reaction, with particular focus on the competition between the R/S photo-isomerization and photo-dissociation. Additionally, we want to investigate the role of the conical intersection in preferring one path over the other. This section describes the 2D-PES and kinetic coupling terms between the adiabatic potentials. Starting from the geometry of the twisted structure of 4MCF with the HF fragment rotated by 90° around the double bond, a grid of points is calculated along the two coordinates of interest: ϕ and R. The R_{HF} distance and other coordinates of the molecular frame are kept frozen at the equilibrium geometry of 4MCF obtained at B3LYP/cc–pVTZ level of theory [24], see section 4.2, using the Gaussian 03 suite of programs [178]. In this twisted orientation the molecule has local C_s symmetry along the xz-plane, whereas in the rest of the grid the molecule has C_1 symmetry.

For simplicity, our model is restricted to the first electronic excited state of $\pi\pi^*$ character and the ground state. Each of the two 2D-PESs are created from 22 single point calculations ranging from $\phi = 90°$ to $\phi = -90°$, and 13 points between $R = 2.5\mathring{A}$ to $R = 6.0\mathring{A}$. To have more points around the CIs and the equilibrium structure, the spacing between the points is inhomogeneous.

Figure 4.8 shows the 1D-PES at $6.0\mathring{A}$ along ϕ. This figure indicates that at the

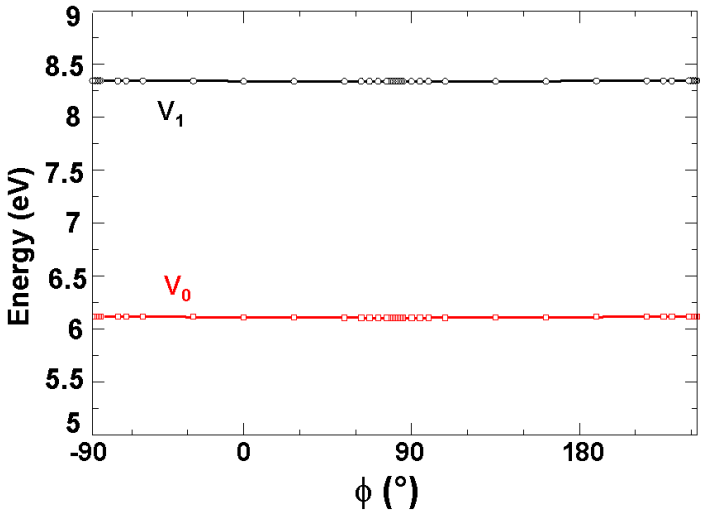

Figure 4.8: 1D-PES at $6.0\mathring{A}$.

dissociation limit, the two PESs do not cross. This implies that if HF rotates after dissociation, it stays on one PES without passing to the other potential. An additional point at $R = 50\mathring{A}$ has been added to the grid to assure the correct asymptotic behavior at the dissociation limit. Then, a total of $22 \times 14 = 308$ single point calculations were carried out. Since the PESs are cyclic in ϕ and symmetric with respect to $\phi = 90°$, a total of $43 \times 14 = 602$ ab initio points were obtained after mirroring. Then, the PESs were cubic splined to a grid of $1024 \times 512 = 524288$ points, obtaining the final PESs ranging from $\phi = -90°$ to $\phi = 270°$, and from $R = 2.5\mathring{A}$ to $R = 6.0\mathring{A}$.

The single point calculations were performed using the SA-CASSCF method, with equal weights for both states. Such wave functions are denoted as $|\Psi_0\rangle$ and $|\Psi_1\rangle$ for the ground and first excited state, respectively. The basis set used is the double zeta basis set cc-pVDZ [147]. The active space includes eight electrons in eight orbitals, namely the π_{CC}, σ_{CH}, σ_{CF}, σ_{CC} and their anti-bonding orbitals shown in Figure 4.7. The two PESs are non-adiabatically coupled with corresponding first order NACTs (or kinetic couplings) with respect to R and ϕ (${T_{01}}^{R^{(1)}}$ and ${T_{01}}^{\phi^{(1)}}$,

respectively), given by

$$T_{01}{}^{R^{(1)}} = \langle \Psi_0^{ad} \mid \frac{\partial}{\partial R} \Psi_1^{ad} \rangle, \tag{4.12}$$

$$T_{01}{}^{\phi^{(1)}} = \langle \Psi_0^{ad} \mid \frac{\partial}{\partial \phi} \Psi_1^{ad} \rangle. \tag{4.13}$$

Eqs. 4.12 and 4.13 are calculated at the same level of theory as the PES using a finite difference method (see section 2.2.1). The calculations were performed using the MOLPRO program package [52].
In the first derivative, defined in eqs. 4.12 and 4.13, the diagonal elements are zero by definition ($T_{00}{}^{R^{(1)}} = 0$, $T_{11}{}^{R^{(1)}} = 0$, $T_{00}{}^{\phi^{(1)}} = 0$ and $T_{11}{}^{\phi^{(1)}} = 0$). The second order NACTS, see eq. 2.49, with respect to R and ϕ are given by

$$T_{01}{}^{R^{(2)}} = \langle \Psi_0^{ad} \mid \frac{\partial^2}{\partial R^2} \Psi_1^{ad} \rangle, \tag{4.14}$$

$$T_{01}{}^{\phi^{(2)}} = \langle \Psi_0^{ad} \mid \frac{\partial^2}{\partial \phi^2} \Psi_1^{ad} \rangle. \tag{4.15}$$

The second order kinetic coupling defined in eqs. 4.14 and 4.15 is much smaller than the first order one, and therefore they can be ignored.

4.3.1 Potential Energy, Dipole and Transition Dipole Surfaces

1D cuts along ϕ and R coordinates of the adiabatic PESs and their corresponding kinetic couplings are shown in Figure 4.9.

Figure 4.9(a) shows that the ground state potential V_0 is symmetric and cyclic with two equivalent minima at ϕ=0° and ϕ=180° corresponding to the R and S enantiomers, respectively. A potential barrier at $\phi = \pm 90°$ of ≈ 3.4 eV separates well these minima and guarantees that a single enantiomer is stable at room temperature without racemizing. The electronic excited state has its minima at $\phi = \pm 90°$ which indicates the existence of CIs, as it is characteristic for olefinic systems at a twisted geometry around the C=C bond [67]. However, the gap between ground and excited states PESs at $\phi = 90°$ is 2 eV. This energy gap is reduced with R, until R= 4.6$\mathring{A}$ where a crossing between both states takes place, as it is shown in Figure 4.9(b). This point matches the position of the HF-elimination CI within this unrelaxed grid. Even though the gap between the maximum of the ground state PES and the minimum of the excited states PES is large at $\phi = 90°$ and R = 3.5$\mathring{A}$, a non-zero

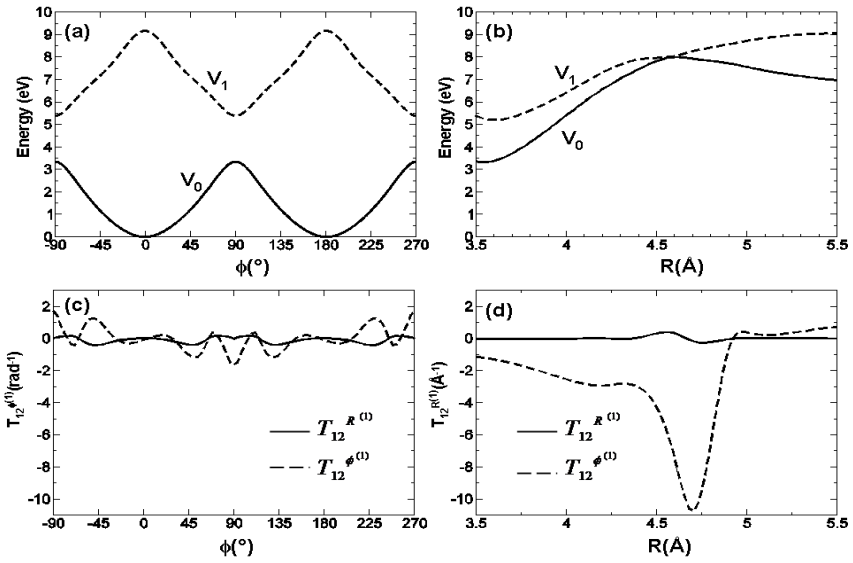

Figure 4.9: Adiabatic 1D-PES and corresponding kinetic couplings calculated at the CASSCF(8,8)/cc-pVDZ level of theory. (a) Unrelaxed adiabatic electronic ground (V_0 in solid) and first singlet excited (V_1 in dotted) states along ϕ for $R = 3.5\mathring{A}$. (b) Dito along R for $\phi = 90°$. (c)-(d) Non-adiabatic (or kinetic) couplings along ϕ and R, respectively. The units in (c)-(d) are given in rad^{-1} and $\mathring{A}^{-1}$ for the kinetic coupling along ϕ and R, respectively.

kinetic coupling of ${T_{01}}^{\phi^{(1)}} = -1.7\ rad^{-1}$ is obtained. This is shown in Figure 4.9(c), meaning that this point is an avoided crossing belonging to the HF-dissociation CI [67]. The large kinetic coupling of ${T_{01}}^{\phi^{(1)}} = -10.7\ rad^{-1}$ at $R = 4.6\mathring{A}$ (see Figure 4.9(c)) confirms that this point is part of the HF-elimination CI. The negligible coupling elements $T_{01}^{R\ (1)}$ (see Figure 4.9(d)) along both coordinates substantiates the approximation used in the diabatization procedure, see section 4.3.2.

The adiabatic 2D-PESs shown in Figure 4.10(a)-(b) contain two conical intersections. The first is the HF-elimination CI mentioned above, local at $R = 4.7\mathring{A}$ and $\phi = 90°$. The other CI is observed at $R = 4.6\mathring{A}$ and $\phi = -90°$. This CI has even a smaller ΔE than the former one 0.045 kJ/mol and has also a higher kinetic coupling (-15.178 rad^{-1}).

The adiabatic dipole moment $\vec{\mu}$ as a function of ϕ and R is calculated at the same level of theory as the PES. Figure 4.11 shows the components of the dipole moment μ_{00}^x, μ_{00}^y and μ_{00}^z of the electronic ground state along ϕ . It is important that μ_{00}^x is anti-symmetric with respect to $\phi = 0°$ while μ_{00}^y and μ_{00}^z are symmetric. The

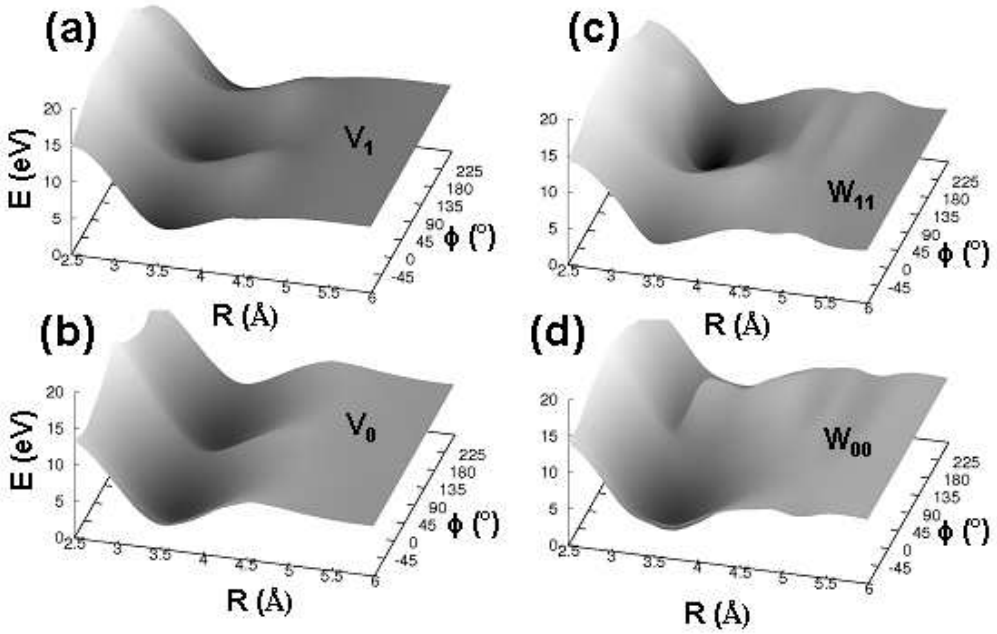

Figure 4.10: 2D adiabatic and diabatic PESs calculated at the CASSCF(8,8)/cc-pVDZ level of theory. Unrelaxed adiabatic electronic ground state (V_0), first adiabatic singlet excited state (V_1), diabatic electronic (W_{00}) and (W_{11}) states along ϕ and R coordinates.

components of the adiabatic electronic transition dipole moments μ_{01}^x, μ_{01}^y and μ_{01}^z along ϕ are shown in Figure 4.12. This figure shows that μ_{01}^x is the anti-symmetric component where μ_{01}^y and μ_{01}^z are symmetric with respect to $\phi = 0°$.

4.3.2 Diabatization

To investigate the photo-dissociation and photo-isomerization dynamics of 4MCF, the nuclear time-dependent Schrödinger equation (TDSE), eq. 2.86 should be solved. As it was discussed in section 2.2.1, the total Hamiltonian is given by eq. 2.52 and 2.53. The total Hamiltonian of the system investigated in this study includes the kinetic energy operator of the nuclei, the adiabatic potentials and the kinetic couplings between the electronic adiabatic states. The kinetic energy operator of the nuclei is described by the rotational moment of inertia (I_r) of HF fragment, with respect to the rotation axis around C=C double , and the dissociation coordinates.

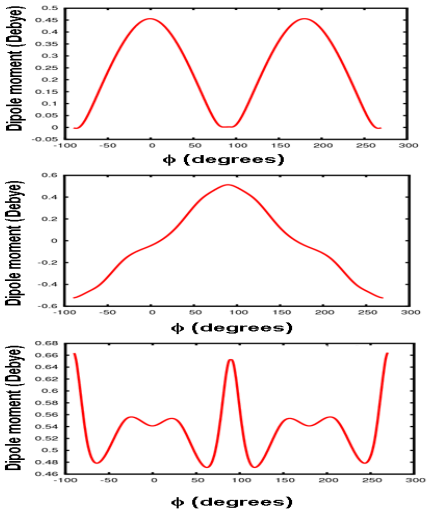

Figure 4.11: Components of the adiabatic dipole moment along ϕ of the electronic ground state as obtained from CASSCF(8,8) calculations for R=3.5 $\mathring{A}$. The upper, middle and bottom plots represent the components of the dipole moment in x, y and z directions, respectively.

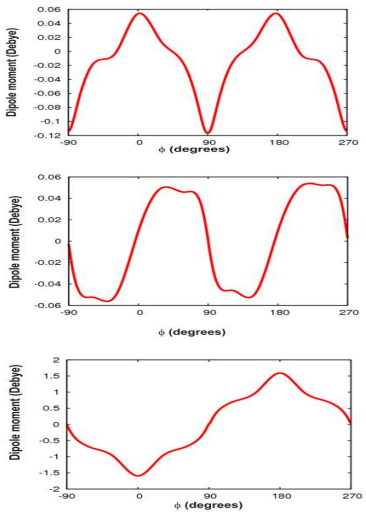

Figure 4.12: Components of the adiabatic transition dipole moment along ϕ of the electronic ground state as obtained from CASSCF(8,8) calculations for R=3.5 $\mathring{A}$. The upper, middle and bottom plots represent the components of the dipole moment in x, y and z directions, respectively.

In the adiabatic presentation, the 2D model adiabatic Hamiltonian $\hat{H}^{ad}$ is given by

$$\hat{H}^{ad}_{ij} = -\frac{\hbar^2}{2m_r}\left(\frac{\partial^2}{\partial R^2} + {T_{ij}}^{R^{(2)}} + 2{T_{ij}}^{R^{(1)}}\frac{\partial}{\partial R}\right) - \frac{\hbar^2}{2I_r}\left(\frac{\partial^2}{\partial \phi^2} + {T_{ij}}^{\phi^{(2)}} + 2{T_{ij}}^{\phi^{(1)}}\frac{\partial}{\partial \phi}\right) + V_i. \tag{4.16}$$

Here, m_r is the reduced mass between the HF and the rest of the molecule, V_i are the adiabatic PESs for the electronic ground and first excited state, ${T_{ij}}^{R/\phi^{(1)}}$ and ${T_{ij}}^{R/\phi^{(2)}}$ represents the first and the second derivatives of the electronic wave function Ψ_i with respect to the nuclear coordinates R and ϕ, respectively. By definition ${T_{ii}}^{R/\phi^{(1)}} = 0$. The second derivative terms are given in eqs. 4.15 and 4.14.

Describing nuclear dynamics in the presence of NACTs is a challenging task. Near CIs the NACTs between the two states have a pole property [57] and the kinetic coupling elements become a singularity at the CI itself. Representing and treating such changes and even singularities is a challenging numerical task. Much effort has been dedicated to find physically meaningful diabatic representations [57, 51, 41]. In this study, the diabatic potentials W are derived directly by transforming the adiabatic ones V as (see eq. 2.60)

$$W_{ij} = U^{\dagger}_{ji} V_{ii} U_{ij}, \tag{4.17}$$

where U_{ij} is a unitary transformation matrix discussed in section 2.2.2 and obtained using eq. 2.54. The mixing angle for each point, defined by R_i and ϕ_i, is the integral over the corresponding non-adiabatic or kinetic couplings. For the 4MCF system, the mixing angle between adiabatic states, see eq. 2.54 and 2.56 in section 2.2.2, is given by:

$$\frac{\partial \alpha_{ij}}{\partial R} = \langle \Psi^{ad}_i \mid \frac{\partial}{\partial R} \mid \Psi^{ad}_i \rangle \tag{4.18}$$

and

$$\frac{\partial \alpha_{ij}}{\partial \phi} = \langle \Psi^{ad}_i \mid \frac{\partial}{\partial \phi} \mid \Psi^{ad}_i \rangle. \tag{4.19}$$

The mixing angle should satisfy the two eqs. (4.18 and 4.19) at the same time.

While calculating the mixing angle α, care must be taken that the diabatic wave functions at 0° and 360° are the same. Accordingly, the path in ϕ has to be well defined such that [57]:

$$\oint_{\phi} {T_{ij}}^{\phi^{(1)}} d\phi = n\pi. \tag{4.20}$$

To obey such condition, α_R is defined for the 4MCF system such that:

$$\alpha_R(R_i, \phi_i) = \int_{\phi_0}^{\phi_i} {T_{01}}^{\phi^{(1)}}, \tag{4.21}$$

here, ${T_{01}}^{\phi^{(1)}}$ represents the coupling between the ground $|\Psi_0^{ad}\rangle$ and excited state $|\Psi_1^{ad}\rangle$. For symmetry reasons, $\alpha_R(R_i, \phi_i)$ must be equal between 0° and 180° and between 180° and 360°. Hence, an approximation to solve this first-order differential equation for the total mixing angle ($\alpha(R_i, \phi_i)$), see Ref. [57], is:

$$\alpha(R_i, \phi_i) = \alpha_R + \int_{R_0}^{R_i} {T_{01}}^{R^{(1)}}(R, \phi_0) dR, \tag{4.22}$$

where R_0 and ϕ_0 are the points where the adiabatic and diabatic PES are forced to be identical. For the 4MCF model, these points are defined at the equilibrium coordinates ($R = 3.5\mathring{A}$ and $\phi = 0°$). As said before, $T^{R^{(1)}}_{01}$ is small and hardly changes along ϕ (see Figure 4.9).

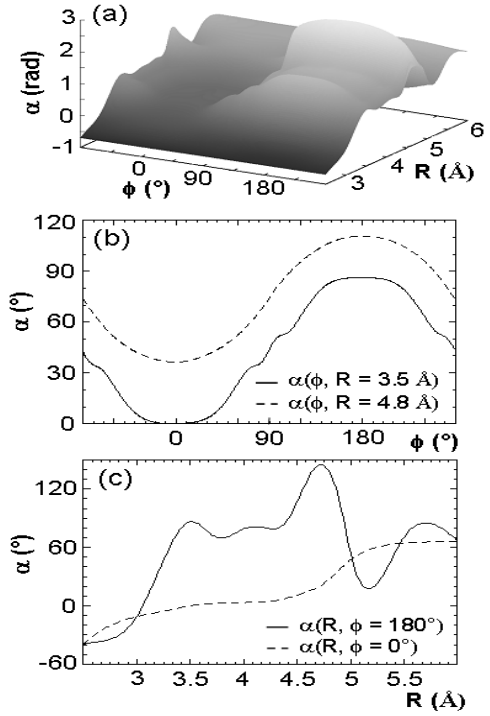

Figure 4.13: Mixing angle (a), 1D cuts for $R = 3.5\mathring{A}$ (solid) and $4.8\mathring{A}$ (dashed) (b) and 1D cuts for $\phi = 180°$ (solid) and 0° (dashed) (c).

Following the approximation implemented in eq. 4.22, first we will perform 1D diabatization along ϕ. Therefore, the unitary transformation matrix U was chosen to

be identity at $\phi_0 = 0$ and $R_0 = 3.5\mathring{A}$. The cyclic condition was achieved by manually forcing the mixing angle α (see eq. 2.56) in U to be zero after the integration over 360°.

Since the 1D adiabatic V_0 and V_1 potentials are symmetric and cyclic along the torsion coordinate, the corresponding 1D diabatic ones W_{00} and W_{11} are also expected to be symmetric and cyclic. The two diabatic states are symmetric only if the mixing angle reaches a multiple of π or $\pi/2$ at its maximum [57]. In fact, this ideal condition is not necessarily maintained in this case because the system is not an ideal two-level system due to mixing of higher excited states with the S_1 state.

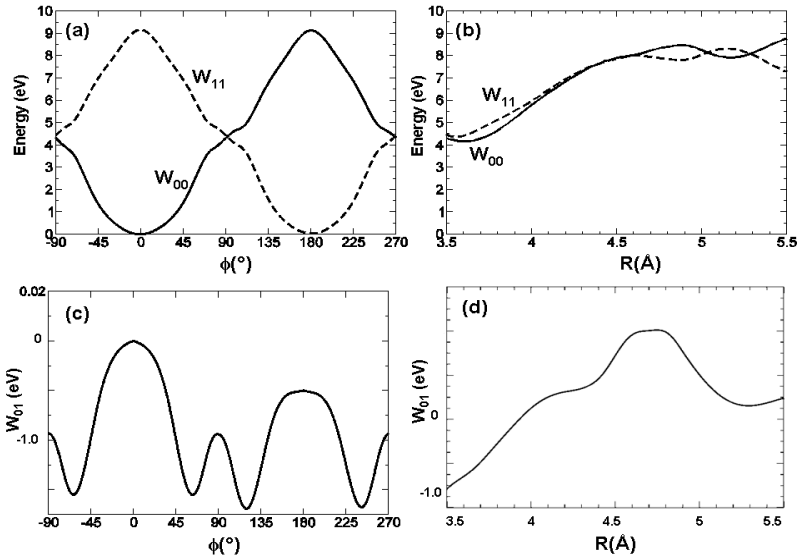

Figure 4.14: Diabatic 1D-PES and corresponding potential couplings calculated at the CASSCF(8,8)/cc-pVDZ level of theory. (a)-(b) Diabatic electronic W_{00} (solid) and W_{11} (dotted) states along ϕ for $R = 3.5\mathring{A}$, and R for $\phi = 90°$, respectively. (c)-(d) Potential couplings along ϕ and R, respectively.

After calculating the mixing angle between the states, one can diabatize the PESs and dipole moment. The 1D diabatic potentials and associated potential couplings are shown in Figure 4.14(a)-(d) and (c)-(d),respectively. Figure 4.10 shows the corresponding adiabatic, (a)-(b), and diabatic, (c)-(d), 2D PES along ϕ and R. Figure 4.10 shows that the adiabatic and diabatic PES are cyclic in ϕ. The adiabatic PES are symmetric (by construction) but the diabatic ones are not. The source of this asymmetry can be found in Figure 4.13 (a), which shows the mixing angle along both coordinates, where it can be realized that the topology is not ideal everywhere. In Figure 4.13 (b) and (c) two 1D cuts of the mixing angle α are shown at $R = 3.5\mathring{A}$

and 4.8$\mathring{A}$ and at $\phi = 0°$ and 180°, respectively. Even though the trend of the mixing angle along ϕ is as to be expected; nevertheless, for $R = 3.5\mathring{A}$ the difference between α at $\phi = 0°$ and 180° is close to $\pi/2$, for $R = 4.8\mathring{A}$ it is not (Figure 4.13 (b)). The difference between the mixing angle in R for $\phi = 0°$ and 180° is neither constant, nor equal to $\pi/2$ as it can be seen more clearly in Figure 4.13 (c). The deviations of the mixing angle α are caused by some artificial configuration mixing of the $\pi\pi^*$ transition with the $\pi\sigma^*$ one as it was discovered upon investigating the electronic wave function for the geometry of $R = 4.9\mathring{A}$ and $\phi = 0°$ as an example (see figure 4.15). This Figure shows orbitals 35A, 36A and 37A which are involved in the dominant excitations in the active space. The most dominant excitation occur from the HOMO (orbital 35A) to the LUMO (orbital 36A) with configuration interaction coefficients of 0.55 and 0.15 for the S_0 and S_1 states, respectively. Another important excitation occurs from the HOMO to orbital 37A with configuration interaction coefficients of 0.05 and 0.36 for the S_0 and S_1 states, respectively. However, there is no $\pi\pi^*$ excitations in the active space for the geometry of $R = 4.9\mathring{A}$ and $\phi = 0°$. On the other hand, it was found that the most dominant excitation in the active space shown in Figure 4.7, for the CI geometry shown in Figure 4.5(b), occurs from the HOMO (orbital 35A) to orbital 37A (π^*_{CC}) with configuration interaction coefficients of 0.57 and 0.01 and for the S_0 and S_1 states, respectively, upon one electron excitation. A configuration coefficients of 0.01 and 0.53 were obtained for the S_0 and S_1 states, respectively upon two electrons excitation to orbital 37A (π^*_{CC}).

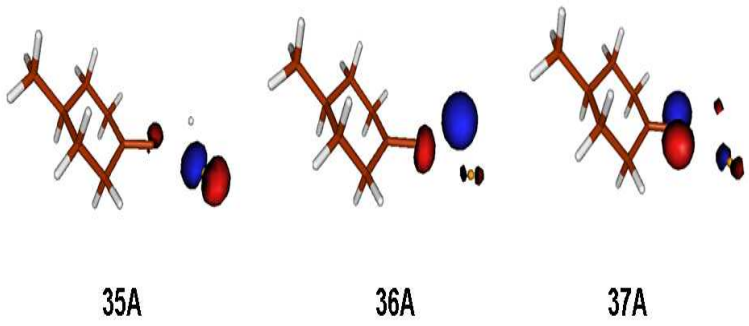

Figure 4.15: Molecular orbitals for the geometry of R = 4.9 $\mathring{A}$ and $\phi = 0°$ showing the configuration mixing of the $\pi\pi^*$ transition with the $\pi\sigma^*$.

Figure 4.16 shows the components of the 1D diabatic dipole moment, see eq. 2.93, along ϕ.

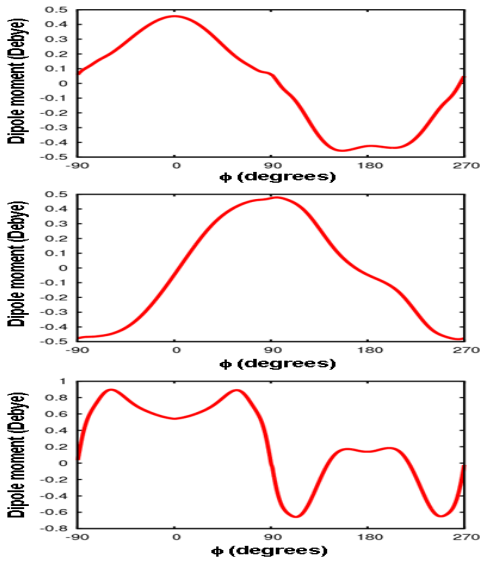

Figure 4.16: Components of the diabatic dipole moment along ϕ of the electronic ground state for R=3.5 $\mathring{A}$. The upper, middle and bottom plots represent the components of the dipole moment in x, y and z directions, respectively.

4.4 Photo-dissociation Dynamics Results

The topology of the PES is of great importance in investigating the reaction dynamics, that is to say, if the wave packet is prevented from passing the crossing region, the HF would be rotating while it is connected to the hydrocarbon fragment. On the other hand, if the wave packet passes the crossing region, the HF would dissociate and rotates as a separate HF molecule; such motion could be measured experimentally. As it was shown in the previous section, the topology of the PESs promises an interesting reaction dynamics; the dissociation is more favorable in the planar conformation and there is a huge barrier (ca. 3.4 eV) to reach the twisted geometry in the S_0 state. This implies that the only way to dissociate the HF molecule is a two-step mechanism consisting in rotation to arrive to the CI and transfer population to the ground state and then, after a exchange of kinetic energy between the two coordinates, the dissociation can occur. For didactic purposes, first we will analyze the non-adiabatic isomerization dynamics alone. This is done using the 1D diabatic potential energy profiles along torsion at the minimum $R = 3.5\mathring{A}$ supposing δ-pulse laser as it is discussed in section 4.4.2. Then, we will investigate the dynamics on 2D PESs of the torsion and dissociation coordinates supposing δ-pulse laser as discussed in section 4.4.3.

4.4.1 One-Dimensional Hamiltonian and its Torsional Eigenstates

The one dimensional model adiabatic Hamiltonian operator $\hat{H}^{ad}$ of 4MCF describing the torsional motion of F and H around the space fixed z-axis is given for each electronic state by:

$$\hat{H}^{ad} = -\frac{\hbar^2}{2I_r}\left(\frac{\partial^2}{\partial\phi^2} + T_{ij}{}^{\phi\phi(2)} + 2T_{ij}{}^{\phi(1)}\frac{\partial}{\partial\phi}\right) + V_i(\phi). \tag{4.23}$$

Here, I_r is the moment of inertia defined as

$$I_r = m_F\, b_F^2 + m_H\, b_H^2, \tag{4.24}$$

where m_F and m_r are the masses of the F and H atoms, respectively and b_F and b_H are the distances of the respective atom to the b point, as sketched in Figure 4.3. The torsional eigenfunctions and eigenenergies of the electronic ground and first excited state are obtained as solution of the TISE, see eq. 2.2. The numerical calculations were carried out on a grid of 1024 points by applying the FGH method [179, 180], using the moment of inertia $I_r = 163527\ m_e a_0^2$. The 1D model diabatic Hamiltonian for this system is:

$$H_{ij}^{d} = -\frac{\hbar^2}{2I_r}\frac{\partial^2}{\partial^2\phi^2} + W_{ij}. \tag{4.25}$$

The torsional eigenenergies for ground and excited states are listed in table 4.1. The energy splitting of the doublets of the energetically lowest states is smaller than the numerical precision of 10 significant figures. The eigenfunctions $\mid \Psi^0_{\nu R/S}\rangle$ are either localized in the inner well or in the outer well. In the dynamical simulations carried out in this study, the wave function is initially localized in one potential well (a superposition of eigenfunctions of the R and S enantiomers).

4.4.2 One-Dimensional δ-Pulse Dynamical Simulations

As it was mentioned in section 4.3.1, each enantiomer of the 4MCF molecule is well separated from the opposite one by two high potential energy barriers (of the order of 30 000 hc cm^{-1}) located at $\phi = 90°$ and $\phi = 270°$. Accordingly, V_0 is a symmetric double barrier potential with two minima located at $\phi = 0°$ and $\phi = 180°$. The energy gaps between the minima of the excited state PES and the maxima of ground

Table 4.1: Torsional eigenenergies for the ground state of the model system 4MCF. The energies of eigenfunctions $\mid \Psi^i_{\nu S}\rangle$ and $\mid \Psi^i_{\nu R}\rangle$ localized in the left well (S-enantiomer) and to the right (R-enantiomer), respectively.

$\mid \Psi^i_{\nu S}\rangle$	energy (cm^{-1})	$\mid \Psi^i_{\nu R}\rangle$	energy (cm^{-1})
0	112.868	0	112.868
1	340.887	1	340.887
2	566.574	2	566.574
3	790.645	3	790.645
4	1013.294	4	1013.294
5	1234.701	5	1234.701
6	1454.962	6	1454.962
7	1674.165	7	1674.165
8	1892.371	8	1892.371
9	2109.633	9	2109.633
10	2325.995	10	2325.995

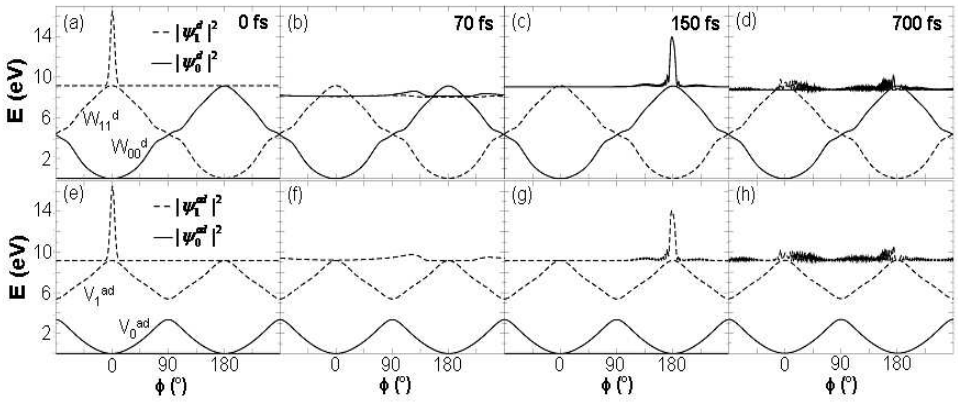

Figure 4.17: Snapshots of the wave function in diabatic (a-d) and adiabatic (e-h) representation simulated on their corresponding potential energy curves at selected times as indicated (R = 3.5 $\mathring{A}$).

state PES point to avoided crossings, which once the potentials are diabatized then cross at $\phi = 90°$ and $\phi = 270°$. In this section, as a first approach, we are interested in exploring the non-adiabatic (or diabatic) isomerization dynamics with the related couplings. This is done using the 1D diabatic PESs (W_{00} and W_{11}) along the torsion angle ϕ at the minimum $R = 3.5\mathring{A}$. Using the 1D diabatic PESs of 4MCF quantum dynamical calculations were performed in a grid of 1024 points using the Split-Operator method [120, 121, 181, 182] with a time discretization of 0.01 fs. We assume all molecules to be in the configuration of the S-enantiomer ($\phi = 0°$), and therefore to be located in the minimum of the W_{00} state. Then, it is instantaneously excited to the W_{11} potential using a δ-pulse. Snapshots of the wave packet in 1D for selected times in the adiabatic and diabatic pictures are shown in Figure 4.17(a-d) and 4.17(e-h), respectively. The adiabatic wave functions are obtained by transforming the diabatic wave function back to the adiabatic one:

$$\begin{pmatrix} \Psi_0^{ad} \\ \Psi_1^{ad} \end{pmatrix} = \begin{pmatrix} \Psi_0^{d} \\ \Psi_1^{d} \end{pmatrix} U^{\dagger}(R). \tag{4.26}$$

Figure 4.17 (b) shows that the wave packet spreads very quickly in both directions along the torsion coordinate. Since the potential is cyclic, both wave packet portions interfere constructively at ≈ 150 fs recovering a localized wave packet at $\phi = 180°$ (R-enantiomer) (Figure 4.17 (c) or (g)). The last snapshot at 700 fs shows the wave packet completely delocalized between the R and S enantiomers (Figure 4.17 (d) and (h)). As expected, both adiabatic and diabatic simulations give the same result. The population transfer to the electronic ground state is negligibly small, even at longer propagation times (700 fs). This is not surprising since the NACT at $\phi = 90°$ is small and the gap between the PESs is still large (Figure 4.17 (a) and (c)) which demonstrates that other coordinates might be necessary to arrive to the CI.

4.4.3 Two-Dimensional δ-Pulse Dynamical Simulations

In the following section, the results of the quantum dynamic simulations in 2-dimensions (2D) are shown. This will allow to investigate the branching of the wave packet in the torsional coordinate (which could preserve a potential molecular rotor or switch) and in the dissociation coordinate (HF fragment elimination), after excitation to the bright $\pi\pi^*$ excited state. A rotor can be preserved in the excited as well as in the ground state. For this reason, it is interesting to investigate the efficiency of the non-adiabatic population transfer to the ground state at or near the CI. Using the 2D diabatic PESs of 4MCF, W_{00} and W_{11}, quantum dynamical calculations in 2D, along ϕ and R, were performed in a grid of 1024×512 points,

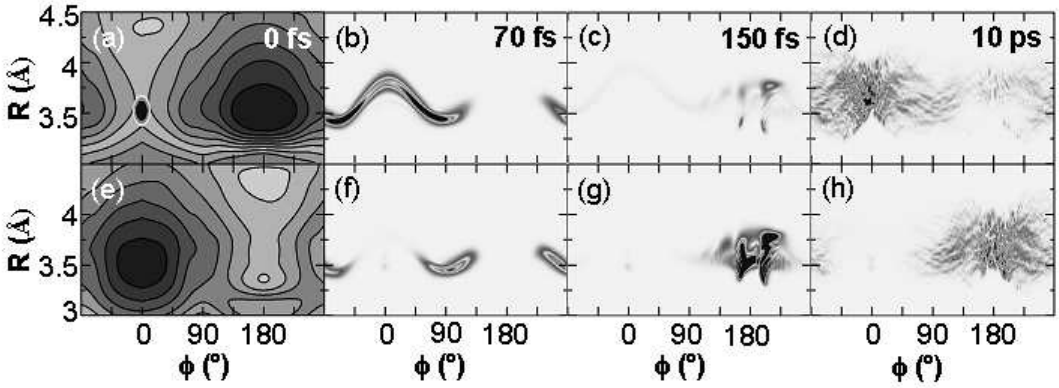

Figure 4.18: Snapshots of wave packet distributions in the 2D diabatic potentials W_{11} (panels a-d) and W_{00} (panels e-h) along R and ϕ for selected times. The corresponding PESs are superimposed in panels (a) and (e).

respectively, using the Split-Operator method [120, 121, 181, 182] with a time discretization of 0.01 fs. The system is initially prepared in the torsional ground state of W_{00} that is localized in the left minimum. Then, it is instantaneously promoted to W_{11} employing a δ-pulse. In 2D the ground state torsional eigenfunction is obtained by, first, calculating two torsional ground state 1D eigenfunctions with the FGH method in a grid of 512 points along R for $\phi = 0°$ and in a grid of 1024 points along ϕ for R=3.5 $\mathring{A}$. Then, an initial 2D guess is prepared as the product of both 1D eigenfunctions. Finally, this guess is relaxed to a minimum by propagating it in imaginary time [117]. In our reduced 2D model, the diabatic Hamiltonian is given by the equation:

$$H_{ij}^{d} = -\frac{\hbar^2}{2\mu}\frac{\partial^2}{\partial^2 R^2} - -\frac{\hbar^2}{2I_r}\frac{\partial^2}{\partial^2 \phi^2} + W_{ij}. \tag{4.27}$$

Snapshots of the wave packet propagation on the 2D diabatic surfaces at selected times are shown in Figure 4.18. After excitation, at 70 fs (Figure 4.18 (b)), it can be seen that the wave packet moves along both R and ϕ coordinates following the gradient of the corresponding W_{11} PES (superimposed in Figure 4.18(a)). It can be also noticed that a portion of the wave packet is already transferred to W_{00} (Figure 4.18 (f)). Furthermore, at 150 fs a recombination of the wave packet in the R enantiomer is observed (Figure 4.18 (c) and (g)). It is interesting to see that the wave packet does not move beyond ca. R =4 $\mathring{A}$ even at long propagation times (10 ps). This shows that although the wave packet starts with an excess of energy of ≈ 2 eV with respect to the HF-elimination CI, within this reduced model no dissociation is observed and torsion dominates. The absence of dissociation products can be

referred to the fact that there is not enough momentum transfer from ϕ to R.

When studying photodissociation dynamics, it is very typical to explore the quantum distributions of the products [162, 183]. Similarly, to evaluate the efficiency of a possible rotor in our 2D model, one can follow the population dynamics in the basis of the previously calculated 1D torsional levels at the equilibrium geometry [85].

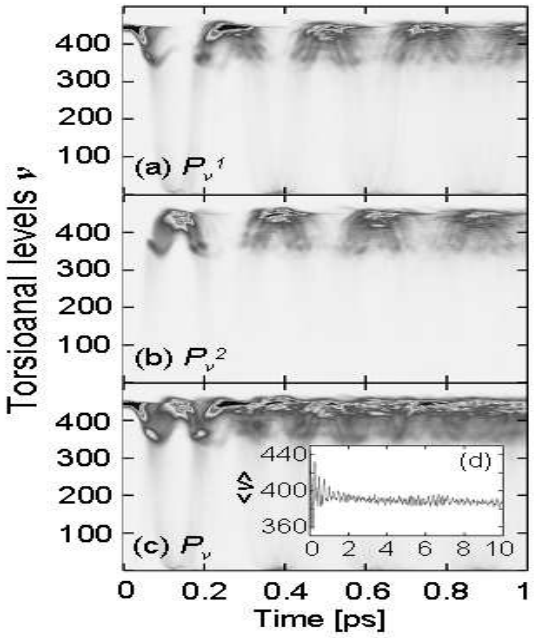

Figure 4.19: Population dynamics in the basis of the torsional states for W_{00} (a), W_{11} (b) and the sum of both (c). The inset (d) shows the average torsional level ν.

If we assume that the eigenfunctions in ϕ are constant with respect to R (as it is close to the equilibrium geometry), we can evaluate the time-dependent vibrational distribution of the wave function at every R:

$$P_v^i(R,t) = \int_\phi \Psi_v^{i*}(\phi)\Psi_v^i(R,t)d\phi, \tag{4.28}$$

where $P_v^i(R,t)$ represents the probability to find the wave function in the vibrational quantum state Ψ_ν^i at every time and for every dissociation distance. These probabilities can be added with respect to R. Thus, the population $P_\nu^i(t)$ in each torsional state ν for the potential i is given by [85]:

$$P_\nu^i(t) = \int_R |\int_\phi \Psi_\nu^{i*}(\phi)\Psi_i^d(R,\phi)|^2 dR. \tag{4.29}$$

The behavior of the system is similar to the 1D propagation since there is no transfer of kinetic energy between the torsion and the dissociation (recalling that there is not enough momentum transfer from ϕ to R). This means that, in our reduced model, the rotation is maintained over at least the first 1 ps. If the sum of the populations in both potentials $P_\nu = \sum_i P_\nu^i$ varies with time, the rotor is destroyed via the dissociation channel. Figure 4.19 (a) and (b) show the out-of-phase P_ν^0 and P_ν^1 which indicate the population exchange between the two diabatic potentials. From the out-of-phase period, it can be observed that the time required to pass from the R to the S enantiomer is ca. 150 fs, in satisfying agreement with the time inferred from the 1D and 2D snapshots of Figures 4.17 and 4.18, respectively. In Figure 4.19 (c), the evolution of the sum of both populations is plotted, illustrating that lower torsional levels are slowly populated over time. This decrease is even more clear in the inset (Figure 4.19 (d)), where the average torsional level $\langle\nu\rangle = \nu P_\nu$ until 10 ps is represented. At long times, the expectation value of ν has decreased from $\approx$ 400 to only 380. Considering that the dissociation energy of the molecule is around 7.5 eV, which corresponds to a torsional level of around 350, a torsional lifetime of at least 10 ps can be anticipated in this molecule.

4.5 Effects of Laser Pulses on the Dynamics of 4MCF

The control of a molecular system by means of an external laser field is a hot topic in the field of quantum dynamics [184, 185]. The objective is to bring the system from a given initial state to a desired final state using laser fields. Finding the "best shape" for a function is subjected to constrains that will maximize or minimize a certain quantity. In the case of applying a laser, the search is for the best shape of the laser pulse, subject to some constraints, to maximize or minimize a certain chemical product yield [126]. Where the constraint is the TDSE, see eq. 2.86, in the presence of the control, which is the electric field interacting with the dipole (permanent or transition dipole moment) of the molecule. Our objective is to design an electric field as a function of time that will move the wave packet in some desired channel, starting out in a well defined initial ground state.
The first quantum simulations towards the ignition of unidirectional intramolecular rotations in chiral molecules have been carried out by means of linearly polarized laser pulses in the IR frequency domain [12, 13, 14, 24]. This approach may provide an alternative to chemical, electrochemical or photochemical stimuli for molecular rotors [186]. In Ref. [24] Quantum ignitions of unidirectional in-

tramolecular rotation is achieved in two steps: first, a few-cycle intense IR laser pulse is used to excite the torsional motion of one fragment in the molecule against the rest of the molecule; second, a well-timed ultrashort UV laser field transfers the system from the electronic ground state into an excited state such that the torsional motion is converted into unidirectional intramolecular rotation. In this thesis we shall carry out exploratory investigations of laser pulses which may turn out useful for future investigations of control of unidirectional intermolecular rotation. Specifically, we study the effect of IR+UV pulses on the oriented model system, (4-methyl-cyclohexylidene)fluoromethane (4MCF). For simplicity, the laser induced wave packets are propagated on 1D PES along the torsion.

4.5.1 IR pulse

The optimization of the IR laser pulse used to excite the torsional motion of the CHF fragment against the rest of the molecule will be discussed in this section. For simplicity, first we will optimize the IR laser pulse representation and investigate its dynamics of the adiabatic representation. Then we will use the obtained optimal laser parameters for propagating the wave packet on the 1D diabatic PESs (after diabatizing the PESs and dipole moments, see Figure 4.14 and 4.16).

Few-cycle pulses were introduced in section 2.4.5, and we will now discuss the design of such pulses for our quantum dynamics simulations. This section will provide a step-by-step guide for building a smooth $\sin^2$-pulse which is used in the forthcoming simulations. We want to design an IR laser pulse that induce the coherent torsion of the CHF moiety. To this aim, the frequency of the IR laser pulse should be tuned to match the natural rotational movement of the CHF moiety. The frequency of the IR laser pulse that excites this mode, ω_{IR}, should therefore have the characteristic that one cycle of the electric filed oscillation ($\frac{2\pi}{\omega_{IR}}$) should match the period of the natural rotational movement of the CHF moiety. For a pulse duration,t_p, the IR pulse frequency given by

$$\omega_{IR} = \frac{2\pi}{t_p}, \tag{4.30}$$

so that the IR frequency, ω_{IR}, can now be replaced in the laser field expression, see eq. 2.112. For a short pulse duration, $t_p \leq 100fs$, the field applies a brief force on the charge distribution (permanent dipole moment) and induces a change in the energy of the system. If this energy is resonant with the natural vibrational energy,

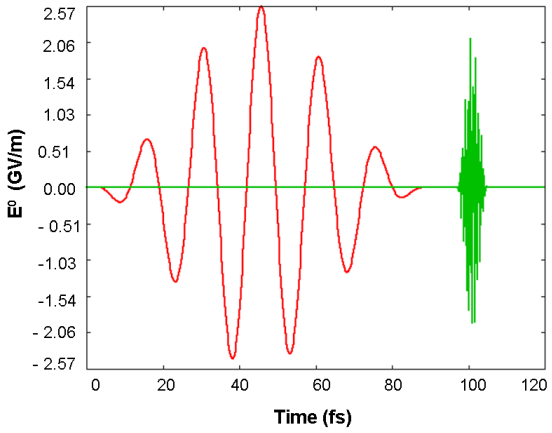

Figure 4.20: IR and UV pulses. The IR pulse (red curve) polarized in the y-direction consists of 5 cycles. The IR pulse parameters are $\vec{E}^0 = 2.57$ GV/m, corresponding to $I_{max} = 875$ GW/cm^2, $\omega_{IR} = 226$ cm^{-1} (see eq. 4.30), $\rho = 0°$, $t_0 = 0$ fs and $t_p = 90$ fs. The UV pulse (green curve) is polarized in the z-direction. The UV pulse parameters are $I_{max} = 617.4$ GW/cm^2, $\omega = 73919$ cm^{-1}, $\rho = 0°$, $t_0 = 97$ fs and $t_p = 8$ fs.

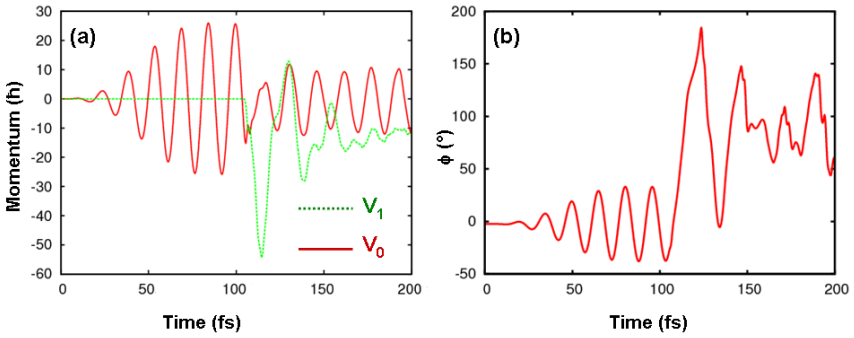

Figure 4.21: Evolution of angular momentum with time. The red and green curves represent the evolution of the angular momentum with time for V_0, V_1 PESs, respectively.

the corresponding vibrational transition will take place. Therefore, the corresponding vibrational eigenstate is excited, and the result is a brief "kick" applied to the CHF moiety which begins rotating around the C=C bond. Few-cycle pulses applied to the system would cause even large in the amplitude torsion angles, similar to a pendulum being pushed each time it reaches its center of motion. One can think of applying few-cycles pulses, each of which would induce the CHF moiety rotation more and more away from its initial position. However, the vibrational wave packet that is created simultaneously undergoes dispersion due to anharmonicity of the PES, so that this competing effect must also be considered over longer times. A compact wave packet is typically desired for maximum population transfer. Therefore, wave packet propagation times and pulse durations should be kept short relative to dispersion time scales.

Few-cycle pulses can be replaced by a single $\sin^2$-shaped pulse with an average IR carrier frequency, ω_{IR}, that smoothly turns on and off, as introduced in eqs. 2.110 and 2.111. Pulse duration, t_p, in eq. 2.110 is the pulse duration governing the number of field cycles that are contained within the pulse envelope. A smooth five cycle IR pulse that is shown in Figure 4.20 was used in this study. The choice of the five cycle pulses was made so as to obtain the maximum population transfer. This five cycles IR laser pulse is polarized in the y-direction of the oriented 4MCF model system. This pulse consists of 5 cycles ($\vec{E}^0 = 2.57$ GV/m) with a maximum intensity of 857 GW/cm^2. The optimal pulse parameters (see eq. 2.112) are $\omega = 226 cm^{-1}$, $\rho = 0°$, $t_0 = 0fs$, and $t_p = 90$ fs. At the end of the IR laser pulse, the wave packet has been coherently shifted $\phi = 38°$ from the equilibrium position at 88 fs. Then, it swings back towards the opposite turning point ($\phi = 32°$) at 95 fs, gaining maximum torsional angular momentum maximum amplitude (Figure 4.21) at ≈ 100 fs. The wave packet created in the electronic adiabatic state V_0 is shown in Figure 4.22(a).

4.5.2 UV pulse

When the appropriate torsional movement has been maximally shifted by the few-cycle IR pulse (and gaining maximum torsional angular momentum), an ultrashort UV pulse can be applied to excite vertically the displaced wave packet, see Figure 4.22(b), to the excited state. We will now discuss the design of the UV pulse. The frequency of the UV light, ω_{UV}, should be chosen such that it matches the vertical energy spacing between the ground and first excited states PESs. The intensity of the pulse is chosen to transfer the maximum population from the adiabatic V_0 to the V_1 state. Such a UV pulse, polarized in the z-direction centered at 73919 cm^{-1}, has a maximum intensity of $617.4 GW/cm^2$, $\omega_{UV} = 73919 cm^{-1}$ and $\rho = 0°$,

see eq. 2.112. The pulse duration is $8fs$. At $100fs$ (Figure 4.20), the wave packet is transferred vertically from the electronic ground state to the excited singlet state with almost 55% efficiency. The resulting FC transition conserves the momentum. Therefore, the wave packet created in the electronic excited state V_1 starts moving on the V_1 1D-PES as it is shown in Figure 4.22(a)-(b). The related kinetic energy is large enough to overcome the barrier and the wave packet begins to move in a unidirectional manner.

4.5.3 Exploratory One-Dimensional Dynamics under IR and UV Laser Pulses

In this section we will discuss the effect of applying the IR+UV laser pulses discussed in sections 4.5.1 and 4.5.2 on 4MCF. The propagation of the wave packet will be done in adiabatic and diabatic 1D-PESs. The ultrashort IR+UV laser fields are shown in Figure 4.20, and their effects on the a S-enantiomer in the adiabatic representations are shown in Figure 4.22(a)-(b). This figure illustrates how the IR pulse induces the movement of the wave packet in V_0 and then the UV excites it to the V_1 with almost 53% efficiency, see Figure 4.23.

The results shown in Figure 4.22(a)-(b), have been obtained for the adiabatic wave packet dynamics propagated on adiabatic PESs and employing adiabatic dipole moments, see eq. 2.91. The IR and UV pulses employed here utilize the adiabatic dipole moment in the y- and z- direction, respectively (see Figure 4.11 and 4.12). This figure shows that the wave packet spreads very quickly in both directions along the torsion coordinate. Since the potential is cyclic, both wave packet portions interfere constructively at ca. 120 fs recovering a localized wave packet at $\phi = 180°$ (R-enantiomer). At 200 fs, the wave packet is delocalized between the R and S enantiomers and the wave packet begins to move in a unidirectional manner involving sequential cis-trans isomerizations which implies that the rotor can be preserved in the excited state.

Figure 4.22(c)-(d) shows the wave packet dynamics obtained in the diabatic representations. These results are obtained by applying eq. 2.92 on the diabatic 1D PESs. The IR and UV pulses employed here utilize the diabatic dipole moment in the y- and z- direction, respectively (see Figure 4.16). As it is expected, both adiabatic and diabatic simulations provide the same result.

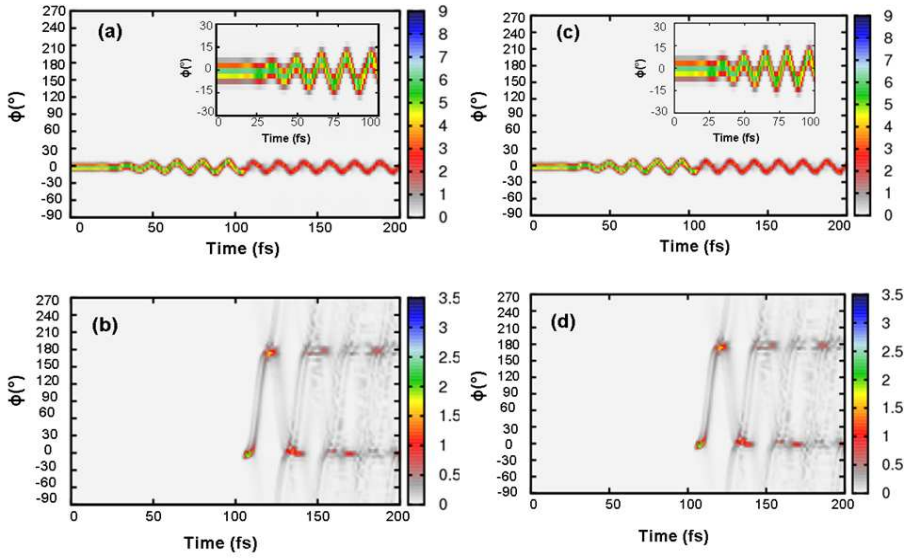

Figure 4.22: Evolution of the wave packet after applying a few-cycle IR and a UV pulse on the adiabatic (a) V_0, (b) V_1 and diabatic (c) W_{00} and (d) W_{11} PESs. The insets in plots (a) and (c) show a zoom for the evolution of the wave packet between $t = 0$ fs and $t = 150$ fs. The IR pulse is polarized in the y-direction and has the parameters: $I_{max} = 875\ GW/cm^2$, $\omega_{IR} = 226\ cm^{-1}$, $\rho = 0°$, $t_0 = 0$ fs and $t_p = 18$ fs. The UV pulse is polarized in the z-direction and has the parameters: $I_{max} = 617.4 GW/cm^2$, $\omega_{UV} = 73919 cm^{-1}$, $\rho = 0°$, $t_0 = 97$ fs and $t_p = 8$ fs.

Figure 4.23(a) shows the population of the wave packet on the adiabatic and diabatic PESs. This figures shows that at the time of applying the UV pulse ($t = 100 fs$), almost 53% of the wave packet is transferred to top hill of the adiabatic V_1 state PESs. However, at the end of UV pulse duration ($105 fs$), almost 47% of the population remains on the adiabatic PESs. Almost 47% of the wave packet is transferred to the excited state PES during all the propagation time of $200 fs$ in the adiabatic representation. For dynamical simulations in the diabatic representation, 45% of the population remains on the W_{11} state. Figure 4.23(b) shows that the same behavior obtained when exciting the wave packet from the R or S enantiomers on the adiabatic PESs in the adiabatic representation.

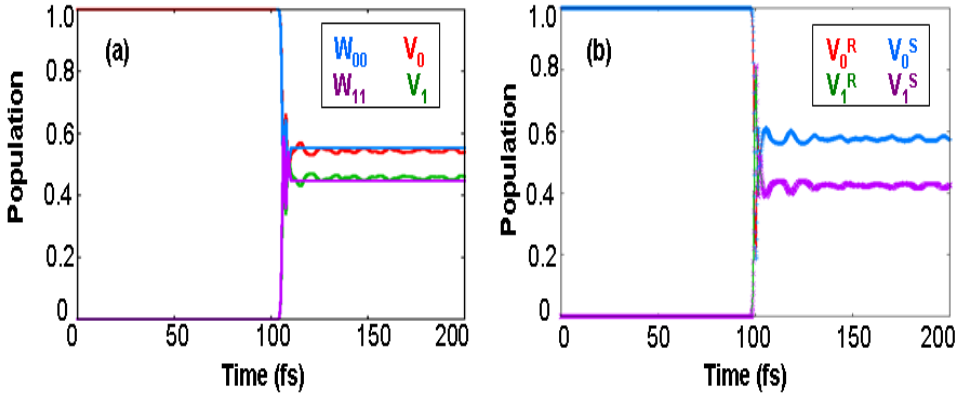

Figure 4.23: (a) Population of the wave packet on the diabatic and adiabatic PESs. The blue, violet, red and green curves indicate population on the V_0, V_1, W_{00} and W_{11} PESs, respectively. (b) Population of the wave packet on the adiabatic PESs for excitation the wave packet of the R and S enantiomers. The blue, violet, red and green curves indicate population on the V_0^S, V_1^S, V_0^R and V_1^R PESs, respectively. The superscripts "S" and "R" refers to the S and R enantiomers, respectively.

4.5.4 Outlook

A simple model is set up aiming to investigate the chiral interconversion between R and S enantiomers of the 4MCF molecule obtained upon rotation around the C=C double bond, versus the competing reaction of eliminating HF. To this aim, two relevant coordinates were considered to build the PESs namely, the torsion around the C=C and the distance between the center of masses of the hydrocarbon moiety and the HF fragment. Then, 1D and 2D quantum dynamics were carried out on the calculated PESs. Both adiabatic and diabatic simulations shows that the population transfer to the electronic ground state is negligibly small, even at longer propagation times. The behavior of the system in 2D propagations is similar to the 1D propagation since there is no transfer of kinetic energy between the torsion and the dissociation. This means that, in our reduced model, isomerization dominates over dissociation in the ps time scale.

Investigating the effect of laser pulses on the 4MCF dynamics was done employing quantum ignition by means of few-cycles IR+UV laser pulses on 1D PESs. In this thesis we have used methods based on manual optimization of the laser in order to design an appropriate laser pulse sequence which can be useful for future investigations of control of unidirectional intramolecular rotation. Quantum ignition of an intramolecular rotation may be exploited as initial step in order to

drive a molecular rotor by laser light. After that, the unidirectional rotation must be preserved efficiently bringing a molecular machine to work. By resemblance to macroscopic or biological machines, this second assignment needs a permanent supply of energy. The most primitive solution to this problem is permanent repetition of the sequential IR+UV laser pulses, corresponding to continuous re-start of the molecular rotor. An efficient scheme as suggested in [24], is that after ignition of the unidirectional intramolecular rotation, it is maintained by a series of ultrashort UV pulses which induce sequential electronic transitions between the electronic ground and excited states. Another option to maintain unidirectional intramolecular rotations even in dissipative environments is implied by the approach of Korolkov and Paramonov [187], i.e. dissipative loss of rotational energy and angular momentum can be compensated by permanent re-excitations by continuous wave lasers which induce transitions from torsional to more excited intramolecular rotational states [24]. To achieve the laser control of the 4MCF dynamics, torsional and intramolecular angular momentum should be conserved. Unfortunately, with the laser pulses employed in this thesis, we did not achieve this purpose.

However, there are some limitations in the model employed in this study. The most important limitation is the use of a reduced 2D system. In principle, the lack of other coordinates requires caution in the interpretation of the results. However, since after vertical excitation 4MCF does have enough kinetic energy excess to reach the HF-elimination CI, photodissociation should have manifested already within this 2D model, and it has not. Other coordinates, like the H–F distance or pyramidalization, will certainly move (lower) the position of the CI and add more excess of kinetic energy to the initial wave packet. However, even this could accelerate the transfer of momentum from the torsion to the HF dissociation coordinate, it is not reasonable that the photolysis time scale change from ns to fs. Based on these considerations, we are therefore left to conclude that the HF- dissociation dynamics from the $\pi\pi^*$ state is not competitive to isomerization in olefinic systems on ultrashort time scales. On the other hand, due to the configuration mixing of the $\pi\pi^*$ transitions with the $\sigma\pi^*$, considering more states in necessary for more proper description of the 4MCF dynamics.

4.6 Summary

This study investigates the branching of the wave packet in the torsional coordinate (that preserves a potential molecular rotor or switch) versus the HF elimination or dissociation coordinate. Wave packet propagations show that although the system

has enough energy to access the HF-elimination CI, isomerization dominates after light irradiation. These results are encouraging for the use of 4MCF as a model for a molecular device. It was shown that no dissociation is observed and torsion dominates, although the wave packet starts with an excess of energy of ≈ 2 eV with respect to the HF-elimination CI. The absence of dissociation products can be explained by the fact that there is not enough momentum transfer from ϕ to R.
The present model simulations suggest that, analogous to what was obtained in Ref. [24], quantum ignition of unidirectional intramolecular rotation is possible in two steps: first, a few-cycle intense IR laser pulse excites the torsional motion of CHF fragment against the rest of the molecule; second, a well-timed ultrashort UV laser field transfers the system from the electronic ground state into an excited state such that the torsional motion is converted into unidirectional intramolecular rotation.

Chapter 5

Solvent effect on the conical intersection of 4-cyclopentadienylidene-1,4-dihydropyridine (CPDHP)

5.1 Background: Experimental and Theoretical Investigation of Solvent Effect on the Conical Intersection.

The photo-physics of 1-butyl-4-(1H-inden-1-ylidene)-1,4-dihydropyridine (BIDP) was discussed in Ref. [74] as system for which a conical intersection between S_1 and S_0 states is predicted to be strongly affected by interactions with a solvent. The BIDP molecule (see Figure 5.1) is stable under ambient conditions and has a very strong absorption in the visible region. Besides, it can be dissolved in both polar and non-polar solvents. In addition, it was also reported to be none fluorescent [188], indicating rapid radiationless decay (weak emission in MeCN [189]). All these reasons make this molecule very easy to handle experimentally and to be selected for the practical demonstration where the interest is in a molecular system in which the conical intersection can be manipulated in a predetermined way. Fluorescence

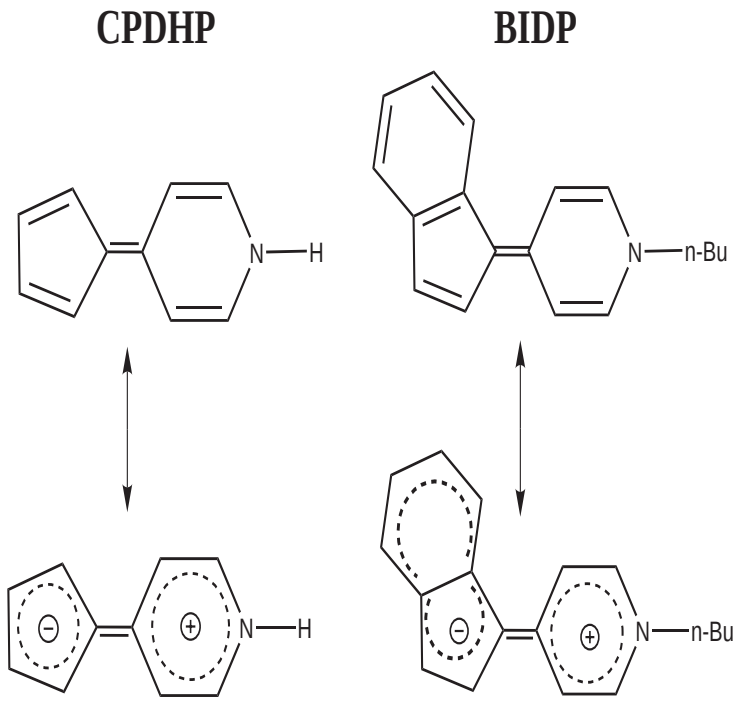

Figure 5.1: The BIDP and CPDHP two main valence bond structures.

experiments on (1-butyl-4-(1H-inden-1-ylidene)-1,4-dihydropyridine (BIDP, Figure 5.1) have revealed that the fluorescence quantum yield of the S_0 state is of the order of 20-60% in various cryogenic glasses but becomes very small in fluid solutions [74]. Moreover, the fluid solution yield is about five times larger in a polar solvent (acetonitrile, MeCN) than in a non-polar one (methylcyclohexane, MCH). The rapid nonradiative transitions in fluid solutions were assigned to internal conversion in both solvent classes, as intersystem crossing is much slower than internal conversion and no net reaction is observed [189]. These results are in agreement with predictions made for the closely related (in terms of electronic structure) but simpler molecule 4-cyclopentadienylidene-1,4-dihydropyridine (CPDHP) for which a conical intersection between S_1 and S_0 states was recently proposed [86, 143] based on a method developed to locate conical intersections between the ground state potential surface and the first electronically excited states of polyatomic molecules [142]. The method is an extension of the Longuet-Higgins sign-change theorem [29] and uses reaction coordinates of elementary reactions as the starting point of the analysis. The structures of the molecules studied in [74] (1-butyl-4-(1H-inden-1-ylidene)-1,4-dihydropyridine (BIDP) as well the smaller molecule used for high level computations (cyclopentadienyl-dihydropyridine (CPDHP)) are shown in Figure 5.1. This

figure shows that the two dominant valence bond structures of BIDP are similar to those for CPDHP [143]. The combined experimental and theoretical study designed in Ref. [74] such that the polar solvent used at room temperature (MeCN) cannot form hydrogen bonds which illustrates that its effect must be only due to the higher polarity. In line with the model in Ref. [74], the S_1 state was found to have an ultra-short decay time in the fluid solvents indicating the existence of a conical intersection. A strong solvent effect on the lifetime was found where the decay was faster in non-polar solvents than in polar ones. Furthermore, even avoided crossings can act as funnels when the energy gap is small. In view of the similarity between the electronic structures of BIDP and CPDHP, quantum mechanical calculations on the CPDHP model show that a conical intersection between S_1 and S_0 exists in the gas phase and in non-polar solvents, whereas the degeneracy is removed in polar solvents. This unique property is due to the fact that the electronic wave-function of the CPDHP at its equilibrium ground state configuration cannot be presented by single spin pairing scheme. Thus, a covalent and a zwitterion forms are required for this purpose. It was found that there are two possible distinct routes on the

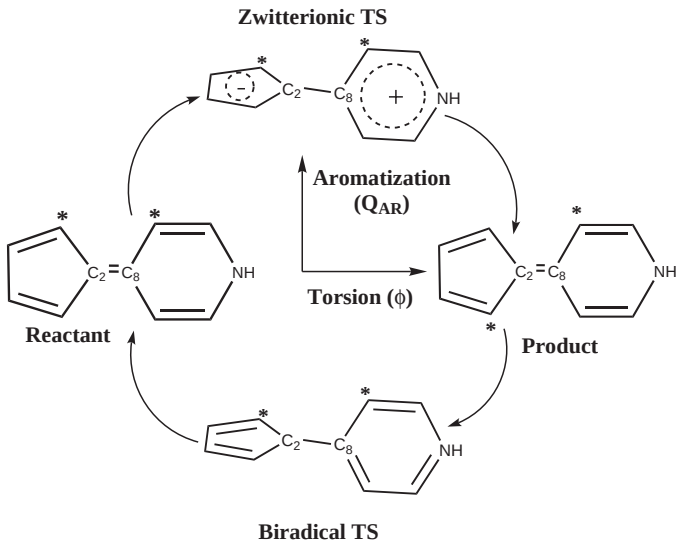

Figure 5.2: The Longuet-Higgins loop for CPDHP. The reactant and product are E and Z isomers and are connected by the torsion coordinate. In the two transition states the pyridine and cyclopentadiene rings are perpendicular to each other. The coordinate connecting them is an aromatization coordinate that converts the quinoid structure of the BRTS to the aromatic structure of the ZWTS. The asterisk (*) labels the relative position of the atoms changed upon rotation around the C_2=C_8 bond.

ground state surface for the E-Z isomerization around inter-annular double bond

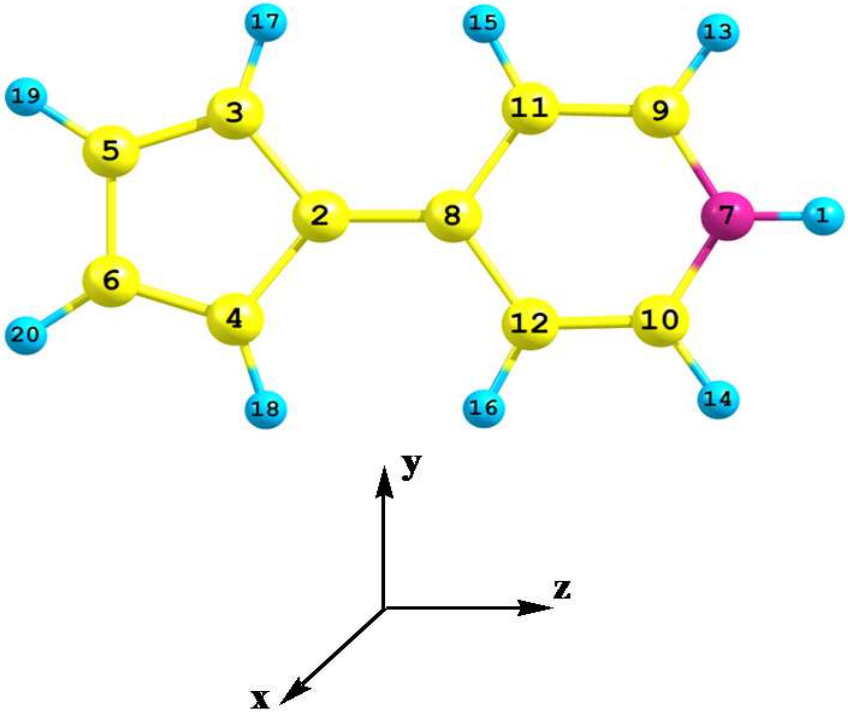

Figure 5.3: Coordinate axes in CPDHP.

[143]. One is via the well known biradical (covalent-ethylene-like) transition state (BRTS), the other via a zwitterion (charge transfer) transition state (ZWTS) that is stabilized by the concomitant aromatization of the two ring systems. A phase inverting Longuet-Higgins loop [25, 143, 142] can be constructed in which a conical intersection is located as Figure 5.2 shows. The gas phase isomerization around the double bond connecting the two rings can be carried out along two reaction coordinates: in one the transition state is of biradical nature, as in ethylene; this transition state is of C_{2V} symmetry and transforms as A_2. The ZWTS is ionic: an electron is transferred from the pyridine ring to the cyclopentadiene one; this transition state also belongs to the C_{2V} symmetry group and transforms as A_1. A phase inverting Longuet-Higgins loop can be constructed for this system by connecting the reactant and product in a closed loop via the two transition states. Therefore, a conical intersection is located within the loop [143, 142, 25]. The loop is shown in Figure 5.2. The structure and the energy of the conical intersection are closely related to both biradical and zwitterion transition states; in specific, the energy can be altered by changing the solvent's polarity. As shown in [74, 189, 86, 143] the conical intersection in this molecule is accessed along the two coordinates: torsion (ϕ) and aromatization (Q_{AR}). The idea that the conical intersection between S_1

and S_0 curve crossing will be eliminated in the presence of a polar solvent was also proposed and discussed. In this study, we provide a calculation of the potential surface along the two coordinates lifting the degeneracy which allows more detailed discussion of the photophysics of this molecule covering both non-polar and polar solvents. To our knowledge, this is the first systematic calculation of the effect of solvent polarity on the energy of conical intersections that analyzes both polar and non-polar solvents. In this chapter we will first introduce the model system used to carry out the quantum mechanical calculations and then discuss the effect of the different solvents on the conical intersection.

5.2 Model System

In order to locate the conical intersection, critical points on the ground state potential energy surface must be located; these include the reactant, product and two transition states [86, 143, 190]. Calculations were carried out using the CASSCF method [149]; the active space was constructed from orbitals suitable for both transition states, in which the two rings are perpendicular to each other (C_{2V} geometry). Figure 5.3 shows that the C_2-C_8 bond lies on the Z-axis, the pyridine ring lies in the YZ-plane and the cyclopentadienyl ring lies in the XZ-plane. This choice facilitated the computations since the CI is also expected to be of C_{2V} symmetry. The active space consisted of all p orbitals, 6 occupied and 5 unoccupied; their shapes and symmetries are shown in Figure 5.4. The two coordinates used to construct the potential energy surfaces (Figure 5.2) are the torsion and the aromatization coordinates. All calculations were first carried out on the isolated molecule. The energies and structures of the ground state and the two transition states were optimized, and used subsequently in the solution phase calculations. The energy and structure of the crossing point between the S_0 and S_1 states was calculated using the method of Ref. [86]. Crossing between PESs takes place at a torsional angle of 90° of C_{2V} symmetry, the two states transform as A_1 and A_2 near the conical intersection. The PES was calculated using state averaged calculations. The effect of the solvent was approximated using the self consistent reaction field (SCRF) theory in the framework of the Kirkwood and Onsager [94, 93] model. The electrostatic free energy calculations were carried out using the GAMESS [101] program suite using the cavity radius of 4.57 $\mathring{A}$ calculated using the standard GAUSSIAN procedure [102]. The potential energy surfaces calculated along the two coordinates lifting the S_0 and S_1 degeneracy are shown for several solvents in Figure 5.5. The aromatization coordinate Q_{AR} is the coordinate connecting the two transition states at the perpendicular configuration as it is shown in Figure 5.2. This coordinate was calculated consid-

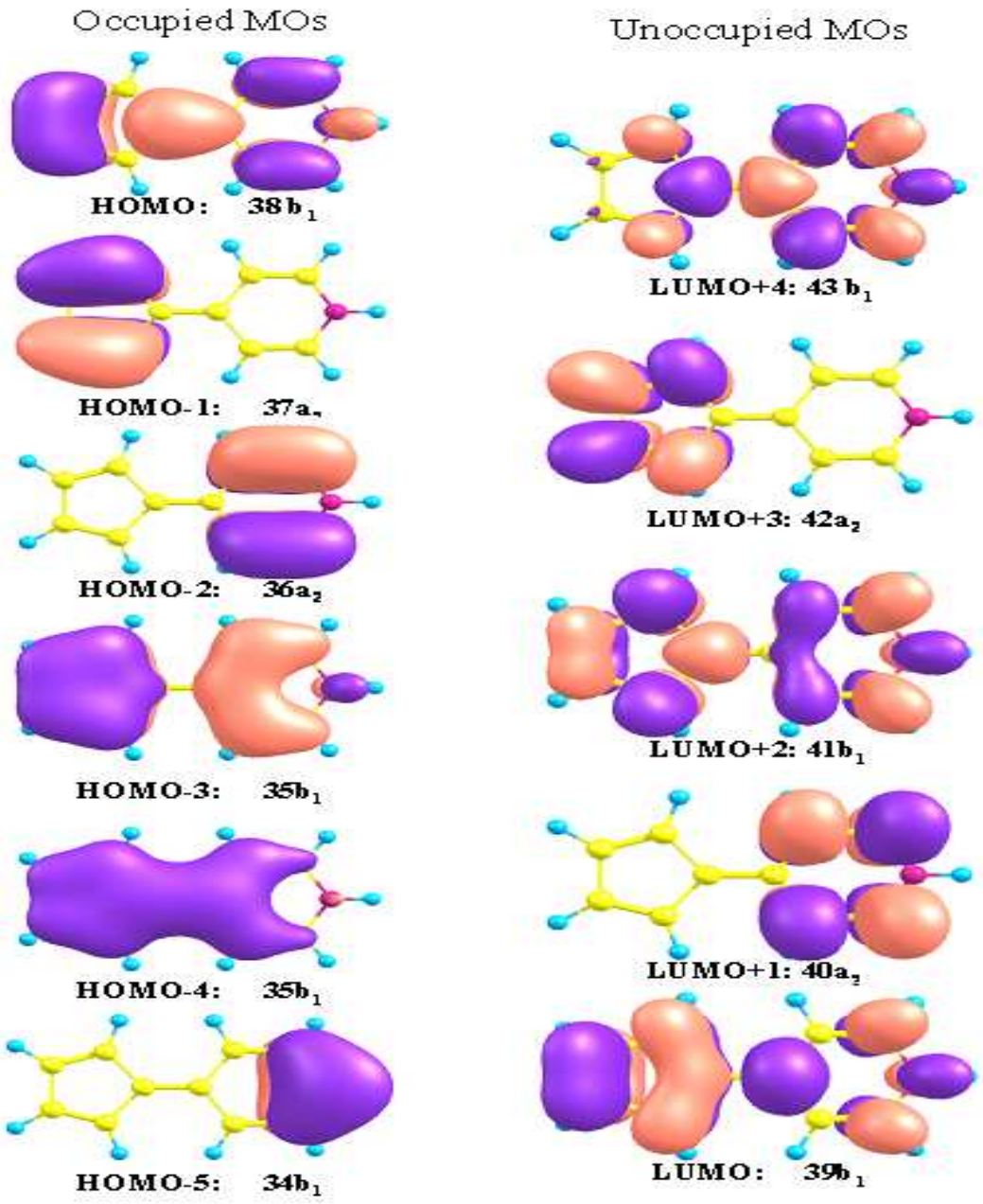

Figure 5.4: Molecular orbitals used in the construction of the active space.

ering the changes in the cartesian coordinates (x, y and z) of all the atoms on the interval starting from the BRTS geometry to the ZWTS geometry. In Figure 5.5 the Q_{AR} coordinate was set to 0 at the BRTS geometry and the interval to the ZWTS geometry was divided to 18 equally spaced segments. The torsion coordinate (ϕ) was divided into a grid of 7 points starting from 90° to 0° with a step size of 15°. Data were calculated for 126 points (18 × 7), and the PESs shown in Figure 5.5 were obtained by linear interpolation using Cartesian coordinates.

5.3 Solvent Effects on the Conical Intersection

The calculated gas phase structures of the ground state minimum, the two transition states and the conical intersection between S_0 and S_1 are shown in Figure 5.6. This figure shows that the CI geometry is intermediate between the geometry of the ZWTS of A_1 symmetry and that of the BRTS of A_2 symmetry but is more alike that of the ZWTS that lies at a higher energy. To invistigate the effect of solvent on the conical intersection, some solvents with different polarities (or dielectric constant, ε) were used in this study. These solvents are methylcyclohexane (MCH, $\varepsilon = 2$), 2 methyl tetrahydrofurane (MTHF, $\varepsilon = 7$) and acetonitrile (MeCN, $\varepsilon = 37.5$). The structure of the CI in MCH was found to be very similar to that of the BRTS, which is the higher lying transition state in this solvent as it is shown in Table 5.1. Table 5.1 shows the calculated energies of the ground state and the two transition states of CPDHP in several solvents in addition to the energy of the conical intersection when applicable. This table also shows the energy gap between S_0 and S_1 states (gap_{S_0,S_1}) and the excitation energy from S_0 to S_1 states ($V_{ex,(S_0,S_1)}$). Table 5.2 shows the dipole moments of the relative geometries. A crossing between S_0 and S_1 states was found only for the gas phase and for MCH while no surface crossing was calculated in the case of the more polar solvents. The geometry of the crossing was different for the two cases in which it was found (see Figure 5.5). Table 5.2 shows that the ground state dipole moment in the gas phase is 4.3 D and becomes a little larger (6.4 D) in polar solvents. On the other hand, the ZWTS has a much larger dipole moment (21.1 D) whereas the BRTS has a dipole moment of only 2.8 D. Therefore, in the ground state the contribution of the biradical-like valence bond structure (Figure 5.5) is larger than that of the zwitterion one, where in the transition states the BRTS has a basically pure biradical nature and the ZWTS a purely ionic charge transfer character.

[1]Energy of the S_0/S_1 conical intersection, or of the two states at their smallest distance.

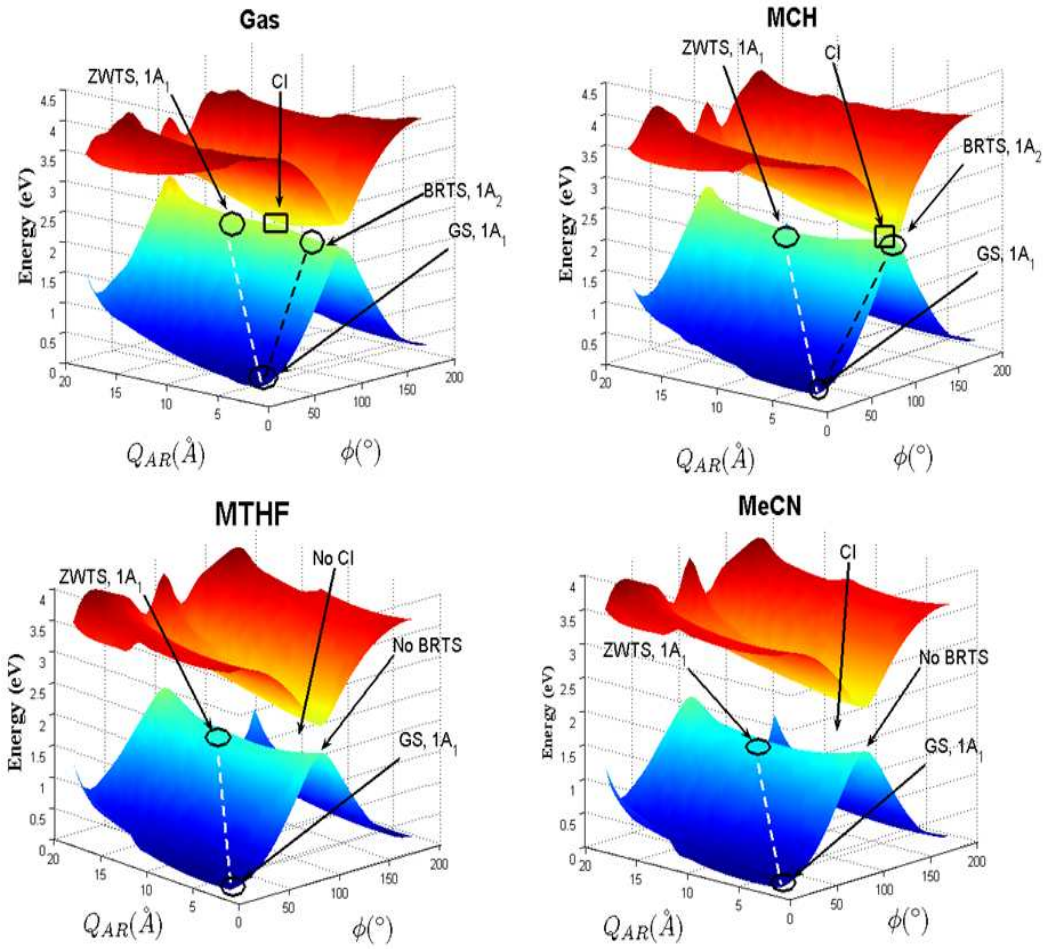

Figure 5.5: The calculated potential energy surface for CPDHP in the gas phase and some solvents in the vicinity of the conical intersection. The positions of the planer ground state (GS) and the two perpendicular transition states both having C_{2V} symmetry are marked in the figure along with that of the CI. In methylcyclohexane (MCH) the CI has a very similar structure to the BRTS and its energy is only slightly higher. In both environments the S_0 and S_1 cross at a torsional angle of 90 degrees, at this angle the states transform as A_1 and A_2. In the more polar solvents, 2-methyl tetrahydrofuran (MTHF) and acetonitrile (MeCN), the $1A_2$ structure lies only on S_1, whereas the ground state transforms as A_1: there is no biradical transition state and the CI disappears in the neighborhood of the transition states, where our model applies.

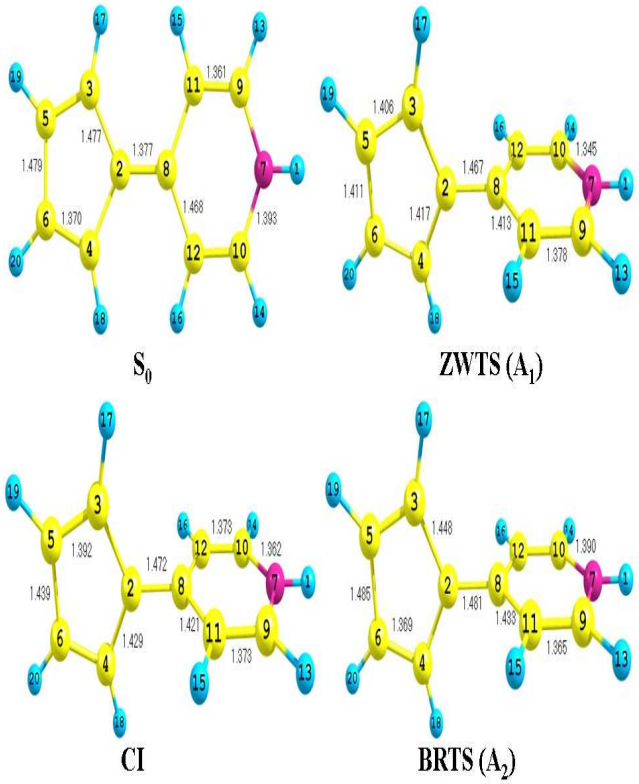

Figure 5.6: Calculated geometries of the optimized forms of some CPDHP species in the gas phase.

Table 5.1: Relative energies (eV) between the structures of CPDHP at the SA–CASSCF(12,11)/cc-pVDZ level in some solvents.

Geometry	**Gas**	**MCH ($\varepsilon = 2$)**	**MTHF ($\varepsilon = 7$)**	**MeCN ($\varepsilon = 37.5$)**
minimum (A_1)	0.000	−0.028	−0.067	−0.087
ZWTS (A_1)	2.048	1.662	1.184	0.960
BRTS (A_2)	1.941	1.935	1.926	1.922
CI[1]	2.093/2.069	1.927/1.938	–	–
gap_{S_0,S_1}	0.024	0.011	0.468	0.685
$V_{ex,(S_0,S_1)}$	4.525	4.380	4.206	4.130

The optimized structures and energies of the minimum, BRTS, ZWTS and the CI between S_0 and S_1 states of the CPDHP in the gas phase are given in Figures

5.6. This figure shows that there is no change in the structure and energy of the A_2 species which is a transition state in the gas phase and in MCH, when the more polar solvents were used. In these environments it became a minimum on S_0. On the contrary, the ZWTS was a transition state in all solvents, and its structure and energy varied considerably upon optimization. The structure of the CI in MCH was found to be very analogous to that of the BRTS, which is the higher lying transition state in this solvent (see Table 5.1). This study spotlights on the effects of equilibrium solvation conditions.

Table 5.2: Dipole moments (D) in the direction of the positive z-axis, see Figure 5.3, for the minimum (S_0), BRTS and ZWTS of CPDHP at the SA–CASSCF(12,11)/ccpVDZ level in some solvents.

Geometry	**Gas**	**MCH (ε = 2)**	**MTHF (ε = 7)**	**MeCN (ε = 37.5)**
minimum (A_1)	4.3	5.0	5.9	6.4
ZWTS (A_1)	16.3	18.1	20.2	21.2
BRTS (A_2)	2.2	2.4	2.7	2.8

In the gas phase, the energy of the BRTS is a little lower than that of the ZWTS (1.94 vs. 2.05 eV, respectively). In the polar solvents, the ZWTS is considerably stabilized to 0.96 eV which lowers the whole ground state potential surface. In these solvents, the biradical perpendicular structure is not a transition state, but lies on the S_1 surface. Hence, there is only one transition state, of A_1 symmetry, under these conditions, and the curve crossing is avoided. The nearest approach of the two surfaces is now at torsion angle of 90° and the structure of the ring (Q_{AR}) that is similar to that of the gas phase BRTS. At 90°, the symmetry of the S_0 state is A_2 at all values of the aromatization coordinate, in contrast with the case of the gas phase and the non-polar solvent. At much higher energies the two surfaces may cross but there is no surface crossing in the neighborhood of the transition states where our model applies. The results designate that solvation, even in polar solvents, does not strongly affect the energy of the ground state relative to the gas phase. A much larger stabilization is obtained for the ZWTS, an effect that leads to the lowering of the ground state potential surface in its vicinity, while the biradical structure maintains its energy and becomes part of the excited state. These trends are in line with the changes in the dipole moments of the species where the dipole moment of the ground state minimum and the biradical species are small (about 4 D) and that of the ZWTS is much larger (16 D). The stabilization energy of a point dipole μ in a solvent having a dielectric constant ε is given by eq. 2.34. For $\varepsilon >> 1$, with μ = 16 D and a = 5 $\mathring{A}$, $\Delta G_{electronic}$ = 0.6 eV. This result is matched

with the quantum chemical computations since, in the highly polar solvents, the two states are separated by about the classically expected value. Consequently, a larger dipole is required to obtain a larger separation between the two potential surfaces; since in the present system the quantity of charge transferred is essentially unity, increasing the distance between the donor and acceptor moieties is the only way to achieve a larger gap between the two states for analogous molecules. Comparing the calculated structures of the CI with those of the transition states, shows that in the both cases the CI structure is more similar to that of higher lying TS: the ZWTS in the gas phase and the BRTS in MCH. In the case of the latter (MCH solvent) the energy of the CI is almost the same as that of the BRTS. This tendency reminds of Hammond's postulate [191] which states that the structure of a transition state of a thermal reaction is similar to that of the species nearest to it in free energy. That is to say, the transition state structure is similar to the less stable minimum. On the basis of these findings, an analog for Hammond's postulate for photochemical reactions was suggested [74]. That is to say; the conical intersection structure is similar to that of the less stable transition state in the relevant LH loop. Whereas the energy minima (reactant and product) are the reference structures in the original Hammond postulate for the transition state, in the case of conical intersections the reference structures are transition states themselves.

5.4 Comparison with Previous Studies

Previous approaches used other methods, which allow extensions to non-equilibrium situations, which may be important in the analysis of ultrafast experiments. Burghardt and Hynes [71] used an extension of the two-electron two-orbital model of Bonačić-Koutecký et al. [72] to estimate the solvent effect on the CI of small protonated Schiff base. The solvent was modeled by 'Marcus-like' parabolas using a parameterized force constant. The authors in [71] describe two situations: a "frozen" solvent polarization where the solvent coordinate is fixed throughout, imposing a pronounced non equilibrium solvation situation, and the case of equilibrium solvation which implies extremely rapid solvent motion, adiabatically adjusting to the solute charge distribution. Since the solvent needs a certain finite time (of the order of magnitude of a hundred to a thousand fs [192], depending upon the solvent), to come to equilibrium with the new charge distribution. Hence it was suggested in [71] that for an ultrafast spectroscopic experiment, the first case is the more realistic picture of solvation effects [73]. Using this approach, the authors found that a conical intersection existing in the gas phase (vacuum) can be eliminated. In this study we are interested in comparing with the experimental results observed

in Ref [74], therefore our choice for the solvation model agrees in accordance with the suggestions in [71, 73]. However, it is unquestionably that the analysis of ultrafast experiments requires non-equilibrium analysis. Nevertheless, this study does not address ultrafast experiments. One has first to analyze the equilibrium case (as we do here) and then, for specific applications, one may add diversions from these conditions. Furthermore, the approach used in [71, 73] is based on empirical potentials. When the interest is in properties that depend directly on the electron density distribution, one has to resort to a more fundamental and general approach using high level quantum mechanics methods. In Yamazaki and Kato's paper [193], the reference interaction site model self consistent field theory [194] was used to model the solvent with the help of semi-empirical model potentials. They limited the discussion to polar solvents only. The approach used in this study utilizes the Onsager-Kirkwood method which allows straight forward comparison of polar and non-polar solvents. Finally it is noticed that the calculation, as well as experimental results on the analogous molecule BIDP, expose a relatively small solvent effect on the electronic absorption spectrum. This is due to the relatively small dipole moment of the molecule in both ground and first excited electronic states. Thus, no predictions concerning the solvent effect on curve crossing can be deduced from the solvent effect on the absorption spectra.

5.5 Summary

In this study, it was found that in the gas phase and in a non-polar solvent the E-Z isomerization of CPDHP can take place along two reaction coordinates, one via a biradical transition state, the other via a zwitterion one. In a polar solvent, the energy of the ZWTS is significantly lowered. The biradical structure, whose energy with respect to the ground state minimum is not changed, becomes part of the excited state. Consequently, a conical intersection between the S_0 and S_1 states is found in the gas phase and non-polar solvents, whereas in polar solvents the degeneracy is lifted. These results are in agreement with experimental findings on a related molecule in which the fluorescence was found to be more intense in polar than in non-polar solvents. At higher energies a different crossing can occur. However, our work is concerned with the low part of the S_0 state, which is responsible for the observed fluorescence.

Chapter 6

Conclusions and Outlook

This thesis aims to obtain a clear picture of the molecular dynamics in the excited electronic state, for three model systems. Two central questions are: (1) whether laser radiation can be used to control the photochemistry of the models used in this study to produce molecular rotors (2) what is the effect of solvent polarity on the conical intersection. On the way towards these goals, several purposes could be achieved for the three systems:

6.1 Photoinduced Quantum Dynamics of Fulvene

In this study, we investigated the photoinduced nuclear dynamics and ultrafast non-radiative decay for a model of fulvene including three nuclear degrees of freedom. The PESs of the ground and first excited electronic states which show a seam of CIs have been calculated using ab initio methods. The proposed model potential is based on the analysis of the quantum chemical calculations. It was shown that the seam of the CIs stretches from planar configuration to the energetically lower twisted structures. This implies a competition between two different photochemical pathways: large amplitude vibration to the CI close to the planar configuration followed by radiationless decay and subsequent return to the initial state versus molecular torsion which leads to photoisomerization. These pathways were explored by quantum dynamical simulations. The diabatic potentials and potential coupling which are required for the dynamical simulations have been obtained with the quasidiabatization method developed by Köppel [63]. The molecules are assumed to be

preoriented (e.g., by a strong nonresonant laser pulse) to permit efficient excitation to the excited electronic state. Radiationless decay due to vibration along symmetric allylic stretching coordinates, which takes place after t ≈10-15 fs, is much faster than the radiationless decay along the torsion coordinates that takes place after t ≈ 50 fs. These results are important for later studies on more accurate three dimensional ab-initio PES where it has been shown that after vertical excitation, the fast radiationless decay along the symmetric allylic stretching coordinates prevents the slower torsion of the CH_2 group [63]. Recently, some dynamical studies has been carried out on the fulvene molecule [63, 64, 65]. The authors in Ref [63, 64, 65]. proposed a wavepacket interferometric scheme for the separation of different nuclear spin isomers. Furthermore, they have pointed to, the conceptually interesting but barely investigated up to now, symmetry-induced coupling of torsion and nuclear spin modes of molecules where they have used the fulvene molecule as a model. This study is just an initial investigation of the photoinduced quantum dynamics of fulvene. Further investigations on this system such as applying optimal control theory, design laser pulses for unidirectional torsions and exploring the effects of strong electric fields are being considered by coworkers [63, 64, 65].

6.2 Photoinduced Quantum Dynamics of 4MCF

This study investigated a model of two competing reactions of the chiral 4MCF: the cis-trans photoisomerization around the C=C double bond and the photodissociation reaction leading to the HF elimination. The competition between the photo-isomerization and photodissociation paths in 4MCF was investigated using two coordinates: the torsion around the double bond and the dissociation coordinates represented by the distance between the centers of masses of the hydrocarbon fragment and the HF fragment. In this reduced dimensionality model, the HF distance is kept rigid and the rest of the molecule is frozen at the equilibrium geometry (minimum that was calculated at B3LYP/6–311+G(d,p) level of theory [24]). Our model was restricted to the ground and first excited valence singlet state, $\pi\pi^*$ states which are coupled non-adiabatically. The corresponding 2D potential energy surfaces, dipoles and non-adiabatic coupling terms (NACTs) along the torsion and dissociation coordinates were calculated using the CASSCF method averaged over two states (SA–CASSCF) with the double zeta basis set cc–pVDZ. The obtained adiabatic PESs were diabatized after calculating the mixing angle α from the ab initio NACTs (see Ref [57]). The obtained diabatic potentials are not symmetric because the mixing angle does not fulfill ideal conditions [57]. The deviations from the ideal conditions obtained with this two-state model are due to the presence of a

second excited state interacting with the first one. Examining the PES corresponding to the $\pi\pi^*$ excited state reveals that an additional crossing of the higher-lying states of $\pi\sigma^*$ nature. More accurate description of this system requires to calculate more electronically excited states beyond the $\pi\pi^*$ excitation (the $\pi\sigma^*$) which will add more complexity to the diabatization and the quantum reaction dynamics. The optimal IR pulse contains three cycle pulses and has a frequency of 225.9 cm^{-1}, amplitude of 0.857 TW/cm^2 and a pulse duration of 83 fs. This pulse provides the wavepacket with a kinetic energy that is large enough to move the wave packet along the torsion coordinates in a unidirectional mode and overcome all potential barriers. Furthermore, the optimal UV pulse obtained is centered at 73919.1 cm^{-1} and has an amplitude of 2 TW/cm^2 and a duration of 80 fs. This pulse, that is applied at 379 fs, transfers the wavepacket vertically from the electronic ground state to the excited singlet state PES with almost 64% efficiency during all the propagation time of 5000 fs. The wavepacket propagations show that although the system has enough energy to access the HF-elimination CI, isomerization dominates after light irradiation. These results are encouraging for the use of 4MCF as a model for a molecular device. It is assumed that HF dissociation takes place only via the ground state because of the CI presence, while a rotor can be conserved in the excited as well as in the ground state. It was shown that within the reduced model no dissociation is observed and torsion dominates. The absence of dissociation products can be explained by the fact that there is not enough momentum transfer from torsion coordinates to the dissociation coordinates. Further investigation of this system such as applying the optimal control theory, designing a laser pulse for selective chiral switches and unidirectional torsions, competing against dissociation via several CIs of coupled potential energy surfaces, exploring the effects of strong electric fields are being considered by other coworkers.

6.3 Solvent Effect on the Conical Intersection of 4-cyclopentadienylidene-1,4-dihydropyridine (CPDHP)

This study spots light on the effects of equilibrium solvation conditions on conical intersections. We present a high level calculation of the potential energy surface of the two lowest lying singlet states of CPDHP for several solvents. It is found that in the gas phase and in a non-polar solvent the E-Z isomerization of CPDHP can take place along two reaction coordinates, one via a biradical transition state, the other via a zwitterion one. In a polar solvent, the energy of the ZWTS is significantly lowered, and the biradical structure, whose energy with respect to the ground state

minimum is not changed, becomes part of the excited state. Consequently, a conical intersection between the ground and first excited electronic states is found in the gas phase and non-polar solvents, whereas in polar solvents the degeneracy is lifted. These results are in line with experimental findings on a related molecule in which the fluorescence was found to be more intense in polar than in non-polar solvents [74]. An analogy for Hammond's postulate [191] for photochemical reactions was suggested. The postulate is that the conical intersection structure is similar to that of the less stable transition state in the relevant Longuet-Higgins loop.

Finally, the results obtained throughout this work provide new insights on the interaction of olefins with laser pulses. Based on these results further theoretical investigations are being already stimulated on the fulvene and 4MCF model systems. In the future, this research as well as other researches carried out within the frame of this trilateral project using the PLCI-QC-QRD approach may serve as basis for experimental application such as the development of molecular rotors.

Bibliography

[1] J.M. Lehn, Proc. Natl. Acad. Sci., USA, 99, 4763 (2002).

[2] T. Ross Kelly, Harshani De Silva and Richard A. Silva, 401, 150 (1999).

[3] N. Koumura, R.W. Zijlstra, R.A. van Delden, N. Harada, B.L. Feringa, Nature 401, 152, (1999).

[4] V. Balzani, M. Venturi, A. Credi, Molecular Devices and Machines: A Journey into the Nanoworld, Wiley-VCH, Weinheim (2004).

[5] V. Balzani, M. Venturi, A. Credi, Special Issue of ScientificAmerican: Nanotech, The Science of the Small GetsDown to Business, September (2001).

[6] V. Balzani, M. Venturi, A. Credi, Acc. Chem. Res., Special issue (Molecular Machines), 34, 6 (2001).

[7] M. Dittrich and K. Schulten, Structure, 14, 1345 (2006).

[8] J. Yu, T. Ha and K. Schulten, Biophys J., 93, 3783 (2007).

[9] B. L. Feringa, J. Org. Chem., 72, 6635 (2007).

[10] J. Hsin, J. Gumbart, L. G. Trabuco, E. Villa, P. Qian, C. N. Hunter and K. Schulten, Biophys J., 97, 321 (2009).

[11] G. S. Kottas, L. I. Clarke, D. Horinek, J. Michl, Chem. Rev., 105, 1281 (2005).

[12] K. Hoki, M. Yamaki, S. Koseki, Y. Fujimura, J. Chem. Phys., 118, 497 (2003) .

[13] K. Hoki, M. Yamaki, Y. Fujimura, Angew. Chem. Int. Ed., 42, 2976 (2003) .

[14] K. Hoki, M. Yamaki, S. Koseki, Y. Fujimura, J. Chem. Phys. 119, 12393 (2003).

[15] T.R. Kelly, H.D. Silva, R.A. Silva, Nature, 401, 150 (1999).

[16] B.L. Feringa, Acc. Chem. Res., 34, 504 (2001).

[17] R.A. van Delden, N. Koumura, A.M.A. Schoevaars, B.L. Feringa, Org. Biomol. Chem., 1, 33 (2003).

[18] J. Vacek, J. Michl, Proc. Natl. Acad. Sci. USA, 98, 5481 (2001).

[19] L. Clarke, D. Horinek, G. Kottas, N. Varaksa, T. Magnera, T.P. Hinderer, R.D. Horanskz, J. Michl, J.G. Price, Nanotechnology, 13, 533 (2002).

[20] J.-P. Sauvage, Molecular Machines and Motors, Springer, Berlin, (2001).

[21] J.-P. Sauvage, Acc. Chem. Res., 31, 611 (1998).

[22] J. Michl, T. Magnera, Proc. Nat. Acad. Sci., USA, 99, 4788 (2002).

[23] T. Seideman, J. Phys. Condens. Matter (Topical Review Section) 15, R521 (2003).

[24] Y. Fujimura, L. González, D. Kröner, J. Manz, I. Mehdaoui, B. Schmidt, Chem. Phys. Lett., 386, 248 (2005).

[25] S. Zilberg, Y. Haas, Chem. Eur. J., 5, 1755 (1999).

[26] S. Zilberg, Y. Haas, Chem. Phys., 259, 249 (2000).

[27] S. Zilberg and Y. Haas, J. Photochem. Photobiol., 144, 221 (2001).

[28] E. Teller., J. Phys. Chem., 41, 109 (1937).

[29] H. C. Longuet-Higgins, Proc. Roy. Soc. London A, 344, 147 (1975).

[30] G. Herzberg, and H. C. Longuet-Higgins, Dis. Faraday Soc., 35, 77 (1963).

[31] S. Zilberg, Y. Haas, Adv. Chem. Phys., 124, 433 (2002).

[32] M. Born, R. Oppenheimer., Ann. Phys., 84, 457 (1927).

[33] A. Szabo, N. S. Ostlund., Modern Quantum Chemistry. Dover Publications, Mineola (New York) (1996).

[34] L. R. Khundkar, A. H. Zewail, Annu. Rev. Phys. Chem., 41, 15 (1999).

[35] A. H. Zewail, Faraday Discuss Chem. Soc., 91, 207 (1991).

[36] G. K. Paramonov. In J. Manz and L. Wőste, (Eds.), fundamentals. In. J. Manz and L. Wäoste, editors, Femtosecond Chemistry. VCH, Weinheim (1995).

[37] T. Baumert, G. Gerber, Adv. At. Molec. Opt. Physics., 35, 163 (1995).

[38] A.H. Zewail, Angew. Chem. Int. Ed., 39, 2586 (1999).

[39] A. Zewail, J. Phys. Chem. A., 104, 5660 (2000).

[40] J. Michl, Bonačić-Koutecký, V. Electronic Aspects of Organic Photochemistry; Wiley: New York, (1990).

[41] W. Domcke, D. Yarkony, H. Köppel, Conical Intersections: Electronic Structure, Dynamics and Spectroscopy; Eds.; World Scientific: Singapore (2004).

[42] C. Daniel, J. Full, L. González, C. Lupulescu, J. Manz, A. Merli, Š. Vajda and L. Wöste, Science, 299, 536 (2003).

[43] R. S. Judson and H. Rabitz. Phys. Rev. Lett., 68, 1500 (1992).

[44] A. Assion, T. Baumert, M. Bergt, T. Brixner, B. Kiefer, V. Seyfried, M. Strehle and G. Gerber. Science, 282, 919 (1998).

[45] S. Shi, A. Woody, H. Rabitz., J. Chem. Phys., 88, 6870 (1988).

[46] A. P. Peirce, M. Dahleh, H. Rabitz. Phys. Rev. A, 37, 4950 (1988).

[47] W. S. Warren, H. Rabitz, M. Dahleh. Science, 259, 1581 (1993).

[48] P. Brumer and M. Shapiro., Chem. Phys. Lett., 126, 541 (1986).

[49] M. Shapiro, P. Brumer, Int. Rev. Phys. Chem., 13, 187 (1994).

[50] R. Schinke, Photodissociation Dynamics, Cambridge University Press, Cambridge (1993).

[51] H. Köppel, W. Domcke, L. S. Cederbaum, Adv. Chem. Phys., 57, 59 (1984).

[52] H.-J. Werner, P. J. Knowles, R. Lindh, F. R. Manby, M. Schütz, P. Celani, T. Korona, A. Mitrushenkov, G. Rauhut, T. B. Adler, R. D. Amos, A. Bernhardsson, A. Berning, D. L. Cooper, M. J. O. Deegan, A. J. Dobbyn, F. Eckert, E. Goll, C. Hampel, G. Hetzer, T. Hrenar, G. Knizia, C. Köppl, Y. Liu, A. W. Lloyd, R. A. Mata, A. J. May, S. J. McNicholas, W. Meyer, M. E. Mura, A. Nicklass, P. Palmieri, K. Pfluger, R. Pitzer, M. Reiher, U. Schumann, H. Stoll, A. J. Stone, R. Tarroni, T. Thorsteinsson, M. Wang, A. Wolf, Molpro, version 2006.1, a package of ab initio programs, see http://www.molpro.net (2006).

[53] G.J. Halász, A. Vibók, S. Suhai, M.Baer, J. Chem. Phys., 127, 244101 (2007).

[54] G.J. Halász, A. Vibók, M.Baer, J. Chem. Phys., 127, 144108 (2007).

[55] C. Levi, G.J. Halász, A. Vibók, I. Bar, Y. Zeiri, R. Kosloff, M. Baer, J. Chem. Phys., 128, 244302 (2008).

[56] J. Pittner, H. Lischka, M. Barbatti, Chem. Phys., 356, 147 (2009).

[57] M. Baer, Beyond Born-Oppenheimer: Electronic Nonadiabatic Coupling Terms and Conical Intersections, John Wiley & Sons, Hoboken, (2006).

[58] J. Dreyer, M. Klessinger, J. Chem. Phys., 101, 10655 (1994).

[59] M. J. Bearpark, F. Bernardi, M. Olivucci, M. A. Robb, and B. R. Smith, J. Am. Chem. Soc., 118, 5254 (1996).

[60] O. Deeb, S. Cogan, S. Zilberg, Chem. Phys., 325, 251 (2006).

[61] M. J. Paterson, M. J. Bearpark, M. A. Robb, L. Blancafort, J. Chem. Phys., 121, 11562 (2004).

[62] F. Sicilia, M. J. Bearpark, L. Blancafort, M. A. Robb, Theor. Chem. Acc., 118, 241 (2007).

[63] S. Alfalah, S. Belz, O. Deeb, M. Leibscher, J. Manz, S. Zilberg, J. Chem. Phys., 130, 124318 (2009).

[64] T. Grohmann, O. Deeb, M. Leibscher, Chem. Phy., 338, 252 (2007).

[65] O. Deeb, M. Leibscher, J. Manz, W. von Muellern, T. Seideman, Chem. Phys. Chem 8, 322 (2007).

[66] M. Barbatti, A. J. A. Aquino, H. Lischka, J. Phys. Chem. A, 109, 5168 (2005).

[67] M. Schreiber, M. Barbatti, S. Zilberg, H. Lischka, L. González, J. Phys. Chem. A 111, 238 (2007).

[68] S. Zilberg, S. Cogan, Y. Haas, O. Deeb, L. González, Chem. Phys. Lett., 443, 43 (2007).

[69] D. Kröner, L. González, Phys. Chem. Chem. Phys., 5, 3933 (2003).

[70] D. Kröner, L. González, Chem. Phys. 298, 55 (2004).

[71] I. Burghardt, J.T. Hynes, J. Phys. Chem. A, 110, 11411 (2006).

[72] V. Bonačić-Koutecký, J. Koutecký, J. Michl, Angew. Chem., 26 (1987) 170.

[73] R. Spezia, I. Burghardt, J.T. Hynes, Mol. Phys., 104, 903 (2006).

[74] S. Cogan, A. Kahan, S. Zilberg, Y. Haas, J. Phys. Chem. A, 112, 5604 (2008).

[75] M. Born, R. Oppenheimer., Ann. Phys., 84, 457 (1927).

[76] C. C. J. Roothan. ,Rev. Mod. Rhys., 23, 69 (1951).

[77] P. O. Löwdin., Adv. Chem. Phys., 2, 207 (1959).

[78] F. Jensen., Computational Chemistry. Wiley, Chichester (1999).

[79] J. C. Slater, Phys. Rev., 36, 57 (1930).

[80] S. F. Boys, Proc. R. Soc. (London) A, 200, 542 (1950).

[81] S. Huzinaga, J. Chem. Phys., 42, 1293 (1965).

[82] B. J. Rosenberg, I. Shavitt, J. Chem. Phys., 63, 2162 (1975).

[83] F. Grimaldi, A. Lecourt, C. Moser, Int. J. Quantum Chem., S1, 153 (1967).

[84] B. O. Roos, P. R. Taylor, Chem. Phys., 48, 157 (1980).

[85] S. Alfalah, D. Kinzel, J. González-Vázquez, L. González, Chem. Phys., submitted.

[86] S. Alfalah, O. Deeb, S. Zilberg, Y. Haas, Chem. Phys. Lett., 459, 100 (2008).

[87] O. Deeb, Faculty of Pharmacy, Al-Quds University, Palestine, private communication (2006).

[88] K. V. Mikkelsen, H. Ågren, J. Mol. Struct., Theochem, 234,425 (1991).

[89] C. J. Cramer, D. G. Truhlar, Chem. Rev., 99, 2161 (1999).

[90] P. E. Smith, B. M. Pettitt, J. Phys. Chem., 98, 9700 (1994).

[91] B. Roux, T. Simonson, Biophys. Chem., 78, 1 (1999).

[92] J. Tomasi, M. Persico, Chem. Rev., 94, 2027 (1994).

[93] L. Onsager, J. Am. Chem. Soc., 58, 1486 (1936).

[94] J. Kirkwood, J. Chem. Phys., 2, 351 (1934).

[95] M. J. S. Dewar, E. G. Zoebisch, E. F. Healy, J. J. P. Stewart, J. Am. Chem. Soc., 107, 3902 (1985).

[96] J. J. P. Stewart, J. Comp. Chem., 10, 209 and 221 (1989).

[97] C.J.F. Böttcher and P. Bordewijk, Theory of Electric Polarization, Elsevier, Amsterdam (1978).

[98] M.M. Karelson, M.C. Zerner, J. Phys. Chem, 96, 6949 (1992).

[99] M. Szafran, M.M. Karelson, J. Kopupt, M. Zerner, J. Comput. Chem., 14, 371 (1992).

[100] Y. Luo, H. Ågren, K.V. Mikkelsen, Chem. Phys. Lett., 275, 145 (1997).

[101] M.W. Schmidt, K.K. Baldridge, J.A. Boatz, S.T. Elbert, M.S. Gordon, J.H. Jensen, S. Koseki, N. Matsunaga, K.A. Nguyen, S. Su, T.L. Windus, M. Dupuis, J.A. Montgomery Jr, J. Comput. Chem. 14, 1347 (1993).

[102] M.W. Wong, K.B. Wiberg and M.J. Frisch, J. Comput. Chem., 16, 385 (1995).

[103] S. A. Trushin, W. Fuss, L. Kompa, and W.E. Schmid. J. Phys. Chem. A, 104, 1997 (2000).

[104] F. T. Smith., Phys. Rev., 179, 111 (1969).

[105] D. Simah, B. Hartke, H. Werner, J. Chem. Phys., 111, 10 (1999).

[106] G. Hirsch, R. J. Buenker, C. Petrongolo, Mol. Phys., 70, 835 (1990).

[107] J. Hendeković, Chem. Phys. Lett., 90, 193 (1982).

[108] G. J. Atchity, K. Ruedenberg, Theor. Chem. Acc., 97, 47 (1997).

[109] K. Ruedenberg, G. J. Atchity, J. Chem. Phys. 99, 3799 (1993).

[110] H. Köppel, J. Gronki, S. Mahapatra, J. Chem Phys., 115, 2377 (2001).

[111] G. Hirsch, P. J. Bruna, R. J. Buenker, S. D. Peyerimhoff. Chem. Phys., 45, 335 (1980).

[112] H.-J. Werner, W. Meyer, J. Chem. Phys., 74, 5802 (1981).

[113] V. Prelog., Science 193, 17 (1976).

[114] C. Clay, M. Balint-Kurti, G. Balint-Kurti, J. Chem. Phys., 91, 3571 (1989).

[115] J. Stare, G. Balint-Kurti, J. Phys. Chem. A, 107, 7204 (2003).

[116] WAVEPACKET by B. Schmidt, Berlin, (1997).

[117] R. Kosloff, Dynamics of Molecules and Chemical Reactions, Mercel Dekker, New York, p. 185 (1996).

[118] E. Merzbacher., Quantum mechanics, John Wiley & Sons, New York (1970).

[119] E. Fischer., Chem. Ber., 27, 2985 (1984).

[120] M. D. Feit, J. A. Fleck Jr., A. Steiger. J. Comput. Phys., 47, 412 (1982).

[121] M. D. Feit, J. A. Fleck Jr., J. Chem. Phys., 78, 301 (1983).

[122] J. Alvarellos, H. Metiu., J. Chem. Phys., 88, 4957 (1988).

[123] A. D. Bandrauk, H. Shen. Can., J. Chem. 70, 555 (1992).

[124] A. D. Bandrauk, H. Shen., J. Chem. Phys., 99, 1185 (1993).

[125] P. Schwendner, F. Seyl, R. Schinke, Chem. Phys., 217, 233 (1997).

[126] D.J. Tannor, Introduction to quantum mechanics, a time-dependent perspective, University science books, California (2007).

[127] F. A. Carey, R. J. Sundberg., Advanced Organic Chemistry. VCH, Weinheim (1993).

[128] G. K. Paramonov, V. A. Savva., Phys. Lett. A, 97, 340 (1983).

[129] D. J. Tannor, S. A. Rice., J. Chem. Phys., 83, 5013 (1985).

[130] D. J. Tannor, R. Kosloff, S. A. Rice., J. Chem. Phys., 85, 5805 (1986).

[131] L. Allen, J. H. Eberly. Optical Resonance and Two-Level Atoms. Wiley, New York (1975).

[132] V. M. Akulin, N. V. Karlov. Intense Resonant Interactions in Quantum Electronics. Springer, Berlin (1992).

[133] M. Holthaus, B. Just., Phys. Rev. A, 49, 1950 (1994).

[134] E. J. Heller., J. Chem. Phys., 68, 2066 (1978).

[135] A. D. Bandrauk, Molecules in intense laser fields: fundamentals. In. J. Manz and L. Wäoste, editors, Femtosecond Chemistry. VCH, Weinheim (1995).

[136] L. V. Keldysh., Sov. Phys. JETP, 20, 1307 (1965).

[137] C. Hirlimann. Pulsed optics. In C. Rulliere, editor, Femtosecond Laser Pulses. Springer, Berlin (1998).

[138] M. Nisoli, G. Sansone, S. Stagira, S. De Silvestri, C. Vozzi, M. Pascolini, L. Poletto, P. Villoresi, G. Tondello., Phys. Rev. Lett., 91, 213905 (2003).

[139] D. J. Jones, S. A. Diddams, J. K. Ranka, A. Stenz, R. S. Windeler, J. L. Hall, S. T. Cundiff., Science, 288, 635 (2000).

[140] C. M. Dion, A. Keller, O. Atabek., Eur. Phys. J. D, 14, 249 (2001).

[141] S. Chelkowski, A. D. Bandrauk., Phys. Rev. A, 71, 053815 (2005). Smith, J. Am. Chem. Soc., 118, 5254 (1996).

[142] S. Zilberg, Y. Haas, Adv. Chem. Phys., 124, 433 (2002).

[143] Y. Haas, S. Cogan, S. Zilberg, Int. J. Quantum Chem., 102, 961 (2005).

[144] V. Galasso, Chem. Phys., 171, 171 (1993).

[145] W.T. Borden, E.R. Davidson, J. Am. Chem. Soc., 101, 3771 (1979).

[146] S. Zilberg, Y. Haas, J. Am. Chem. Soc., 124, 10683 (2002).

[147] T.H. Dunning, J. Chem. Phys., 90, 1007 (1989).

[148] The basis sets were obtained from the Extensible Computational Chemistry Environment Basis Set Database, Version 02/25/04, as developed and distributed by the Molecular Science Computing Facility, Environmental and Molecular Sciences Laboratory which is part of the Pacific Northwest Laboratory, P.O. Box 999, Richland, Washington 99352, USA, and funded by the US Department of Energy. Pacific Northwest Laboratory is a multi-program laboratory operated by Battelle Memorial Institute for the US Department of Energy under contract DE-AC06-76RLO 1830.

[149] B.O. Roos, Adv. Chem. Phys. 69, 399, (1987).

[150] I. Yu, D.W. Cullin, J.M. Williamson, T.A. Miller, J. Chem. Phys., 98, 2682 (1993).

[151] P.J. Domaile, J.E. Kent, M.F. O'Dwyer, Chem. Phys., 6, 66 (1974).

[152] P.J. Harman, J.E. Kent, M.F. O'Dwyer, M.H. Smith, Aust. J. Chem., 32, 2579 (1979).

[153] A. Thiel, H. Köppel, J. Chem Phys., 110, 9371 (1999).

[154] H. Köppel, Faraday Discuss., 127, 35 (2004).

[155] G. Worth, L. S. Cederbaum, Annu. Rev. Phys. Chem., 55, 127 (2004).

[156] R. Morrison, R. Boyd, Organic Chemistry, Prentice-Hall International, Inc., New Jearsy (1992).

[157] B. G. Levine, T. J. Martínez, Ann. Rev. Phys. Chem., 58, 613 (2007).

[158] R. P. Krawczyk, A. Viel, U. Manthe, W. Domcke, J. Chem. Phys., 119, 1397 (2003).

[159] M. Barbatti, J. Paier, H. Lischka, J. Chem. Phys., 121, 11614 (2004).

[160] M. Ben-Nun, T.J. Martínez, Chem. Phys., 259, 237 (2000).

[161] B. A. Balko, J. Zhang, Y. T. Lee, J. Chem. Phys., 97, 935 (1992).

[162] E. F. Cromwell, A. Stolow, M. J. J. Vrakking, Y. T. Lee, J. Chem. Phys., 97, 4029 (1992).

[163] G. E. Hall, J. T. Muckerman, J. M. Preses, J. Ralph E. Weston, G. W. Flynn, A. Persky, J. Chem. Phys., 101, 3679 (1994).

[164] B. A. Balko, J. Zhang, Y. T. Lee, J. Phys. Chem. A, 101, 6611 (1997).

[165] J. J. Lin, S. M. Wu, D. W. Hwang, Y. T. Lee, X. Yang, J. Chem. Phys., 109, 10838 (1998).

[166] D. A. Blank, W. Sun, A. G. Suits, Y. T. Lee, S. W. North, G. E. Hall, J. Chem. Phys., 108, 5414 (1998).

[167] K. Sato, S. Tsunashima, T. Takayanagi, G. Fijisawa, A. Yokoyama, Chem. Phys. Lett., 242, 401 (1995).

[168] A. Peña-Gallego, E. Martínez-Núñez, S. A. Vázquez, Chem. Phys. Lett., 353, 418 (2002).

[169] E. M. Núñez, S. A. Vázquez, Struct. Chem., 12, 95 (2001).

[170] E. Martínez-Núñez, C. M. Estévez, J. R. Flores, S. A. Vázquez, Chem. Phys. Lett., 348, 81 (2001).

[171] J. González-Vázquez, A. Fernández-Ramos, E. Martínez-Núñez, S. A. Vázquez, J. Phys. Chem. A, 107, 1389 (2003).

[172] S. A. Vázquez, F. J. Aoiz, L. Bañares, J. Santamaria, E. Martínez-Núñez, A. Fernández-Ramos, J. Chem. Phys., 118, 9641 (2003).

[173] J. González-Vázquez, L. González, Chem. Phys., 349, 287 (2008).

[174] E. M. Núñez, A. Fernández-Ramos, S. A. Vázquez, F. J. Aoiz, L. Bañares, J. Phys. Chem. A, 107, 7611 (2003).

[175] J. González-Vázquez, E. Martínez-Núñez, S. A. Vázquez, J. Santamaria, L. Bañares, Chem. Phys. Lett., 396, 442 (2004).

[176] I. Ohmine, J. Chem. Phys., 83, 2348 (1985).

[177] J.Z.H. Zhang., Theory and application of quantum molecular dynamics, World Scientific, p. 104 (1999).

[178] M. J. Frisch, G. W. Trucks, H. B. Schlegel, G. E. Scuseria, M. A. Robb, J. R. Cheeseman, J. A. Montgomery, Jr., T. Vreven, K. N. Kudin, J. C. Burant, J. M. Millam, S. S. Iyengar, J. Tomasi, V. Barone, B. Mennucci, M. Cossi, G. Scalmani, N. Rega, G. A. Petersson, H. Nakatsuji, M. Hada, M. Ehara, K. Toyota, R. Fukuda, J. Hasegawa, M. Ishida, T. Nakajima, Y. Honda, O. Kitao, H. Nakai, M. Klene, X. Li, J. E. Knox, H. P. Hratchian, J. B. Cross, V. Bakken, C. Adamo, J. Jaramillo, R. Gomperts, R. E. Stratmann, O. Yazyev, A. J. Austin, R. Cammi, C. Pomelli, J. W. Ochterski, P. Y. Ayala, K. Morokuma, G. A. Voth, P. Salvador, J. J. Dannenberg, V. G. Zakrzewski, S. Dapprich, A. D. Daniels, M. C. Strain, O. Farkas, D. K. Malick, A. D. Rabuck, K. Raghavachari, J. B. Foresman, J. V. Ortiz, Q. Cui, A. G. Baboul, S. Clifford, J. Cioslowski, B. B. Stefanov, G. Liu, A. Liashenko, P. Piskorz, I. Komaromi, R. L. Martin, D. J. Fox, T. Keith, M. A. Al-Laham, C. Y. Peng, A. Nanayakkara, M. Challacombe, P. M. W. Gill, B. Johnson, W. Chen, M. W. Wong, C. Gonzalez, J. A. Pople, Gaussian 03, Revision C.02, Gaussian, Inc., Wallingford, CT, 2004 (2004).

[179] C. Clay, M. Balint-Kurti, G. Balint-Kurti, J. Chem. Phys., 91, 3571 (1989).

[180] J. Stare, G. Balint-Kurti, J. Phys. Chem. A, 107, 7204 (2003).

[181] M. D. Feit, J. A. Fleck, Jr., J. Chem. Phys. 80, 2578 (1984).

[182] R. Kosloff, Annu. Rev. Phys. Chem. 45, 145 (1994).

[183] M. Oppel, G. K. Paramonov, Phys. Rev. A, 60, 3663 (1999). Messina, K. R. Wilson, N. Schwentner, R. M. Whitnell , Y. J. Yan. Phys. Rev. Lett., 74, 3360 (1995).

[184] P.W. Brumer, M. Shapiro, Principles of the Quantum Control of Molecular Processes, John Wiley & Sons, Hoboken (2003).

[185] S. A. Rice, M. Zhao. Optical Control of Molecular Dynamics, Wiley-Interscience (2000).

[186] J. P. Sauvage, Molecular Machines and Motors, Springer, Berlin (2001).

[187] M.V. Korolkov, G.K. Paramonov, Phys. Rev. A, 55, 589 (1997).

[188] J. A. Berson, E. M. Evleth, Z. Hamlet, J. Am. Chem. Soc., 87 (1965) 2887.

[189] S. Cogan, Y. Haas, J. Photochem. Photobiol. A, 193, 25 (2008).

[190] S. Zilberg, Y. Haas, Photochem. Photobiol. Sci., 2, 256 (2003).

[191] G.S. Hammond, J. Am. Chem. Soc. 77 (1955) 334.

[192] M.L. Horng, J.A. Gardecki, A. Papazyan, M.J. Maroncelli, Phys. Chem., 99, 17311 (1995).

[193] S. Yamazaki, S. Kato, J. Chem. Phys., 123, 114510 (2005).

[194] S. Ten-no, F. Hirata, S. Kato, J. Chem. Phys., 100, 7443 (1994).

List of Figures

List of Tables

Glossary

1D	one-dimensional
2D	two-dimensional
4MCF	4-(methyl-cyclohexylidene)-Fluoromethane
a	cavity radius
A	one dimensional totally symmetric irreducible representation under the C_2 symmetry point group
A_1	one dimensional totally symmetric irreducible representation under the C_{2v} symmetry point group
A_2	one dimensional anti-symmetric (with respect to vertical mirror plane) irreducible representation under the C_{2v} symmetry point group
Au(t)	autocorrelation function
B	one dimensional anti-symmetric irreducible representation under the C_2 symmetry point group
BIDP	1-butyl-4-(1*H*-inden-1-ylidene)-1,4-dihydropyridine
BRTS	Biradical transition state
c	speed of light
C	expansion coefficients matrix
C_2	cyclic 2-folded proper axis of rotation symmetric point group
C_{2v}	cyclic 2-folded proper axis of rotation with vertical planes, symmetric point group
CASSCF	complete active space self consistent field
SA-CASSCF	state averaged - complete active space self consistent field
CGF	contracted Gaussian basis function
CI	conical intersection
CID	configuration interaction with doubly excitations
CIS	configuration interaction with singly excitations
CISD	configuration interaction with singly and doubly excitations
cc-pVD/T/Q/5/6Z	correlation-consistent polarized valence double/triple/quadruple/quintuple/sextuple zeta basis sets
CPDHP	cyclopentadienyl-dihydropyridine
CSF	configuration state function
cw	continuous wave
d	diagonal element of the coupling potential matrix W
D	Debye
DFT	density functional theory
DZ	double zeta basis sets
DZP	double zeta polarized basis sets
e	charge of electron
E	energy
E_{corr}	correlation energy
E_e	electronic energy
E_{exact}	exact energy
E_{HF}	Hartree Fock energy
E_0	lowest energy eigenvalue
$\vec{E}(t)$	electromagnetic field
$\vec{E}^0$	amplitude of the field with the carrier frequency
E_{tot}	total energy for fixed nuclei

F	Fock matrix
$\vec{\mathrm{f}}(\mathrm{r})$	Fock operator
f(t)	function describes electric field in time domain
$\mathcal{F}$(ω)	function describes electric field in frequency domain
g	Onsager factor
GTF	Gaussian type function
h	Planck's constant
$\hbar$	reduced Planck's constant, $\hbar = \frac{h}{2\pi}$
H	Hamiltonian
H^{ad}	adiabatic Hamiltonian Matrix
H^{d}	diabatic Hamiltonian Matrix
H_e	electronic Hamiltonian
h(i)	one-electron Hamiltonian
HF	Hartree Fock
HOMO	highest occupied molecular orbital
$\hat{H}(t)$	time dependent Hamiltonian
i	complex number
$\hat{\mathrm{I}}$	identity matrix
I_{max}	maximum intensity
I_r	moment of inertia
irrep	irreducible presentation
$\vec{K}$	wave vector
$\vec{k}$	vector in momentum space
l	angular quantum number
LH	Longuet – Higgins
LUMO	lowest unoccupied molecular orbital
m	magnetic quantum number
MCH	Methylcyclohexane
MCSCF	multi configuration self consistent field
MCSCF-SA	multi configuration self consistent field – state averaged
M_A	mass of nucleus A
m_e	mass of electron
MeCN	Acetonitrile
MTHF	2-methyltetrahydrofuran
MO	molecular orbital
m_r	reduced mass
n	principal quantum number
NACM	nonadiabatic coupling matrix
NACME	nonadiabatic coupling matrix element
NACT	nonadiabatic coupling matrix terms
o_f	off-diagonal element of the coupling potential matrix W in the model potentials
$\mathcal{O}(\Delta t)^3$	numerical error function of third order
$\hat{p}$	momentum operator
PES	potential energy surface
P_{kl}	density matrix
P_υ^i	population in each torsional state (Ψ_υ) for potential i
Q	reaction coordinates

Q_1	coordinates connecting the two minima in the fulvene loop
Q_2	coordinates connecting the two transition states in the fulvene loop
q_a	anti-symmetric allylic stretch coordinates
Q_{AR}	aromatic reaction coordinates
q_s	symmetric allylic stretch coordinates
$\tilde{q}_s$	shifted symmetric allylic stretch coordinates
q_{s0}	symmetric allylic stretch coordinates at $q_s = 0$
q_{sci}	symmetric allylic stretch coordinates at the CI
$q_{s,eq}$	symmetric allylic stretch coordinates at equilibrium geometry
Q_{TSi}	reaction coordinates via transition state, TS
R_{AB}	distance between nuclei A and B
RHF	restricted Hartree Fock
R_{iA}	distance between electron i and atom A
r_{ij}	distance between electrons i and j (spatial coordinates)
$\hat{R}_F$	reaction field operator
S	overlap matrix
S_0	ground electronic state
S_1	first excited electronic state
SAS	solvent accessible surface
SCF	self consistent field
SCRF	self consistent reaction field
S_{kl}	overlap matrix
$s(t)$	shape function of the laser pulse envelope
STF	Slater type function
t	time
TDSE	Time-dependent Shrödinger equation
$T_{ji}^{(1)}$	first order nonadaiabatic coupling terms between electronic states *j & i*
$T_{ji}^{(2)}$	second order nonadaiabatic coupling terms between electronic states *j & i*
t_d	starting time
T_e	kinetic energy of electrons
TISE	time-independent Shrödinger equation
T_N	kinetic energy of nuclei
T_{Ne}	Coulomb attraction between the nuclei and electrons
t_p	pulse duration
TS	transition state
u	atomic mass unit
U(R)	unitary transformation matrix
UHF	unrestricted Hartree Fock
$\hat{U}(t)$	time evolution operator
VB	valence bond theory
V_{ee}	repulsion between electrons
$\hat{V}^{ext}$	operator of external field (time dependent)
V_{ex}	excitation energy
V_g	potential energy function of the ground state
V_e	potential energy function of the excited state
V_i	potential energy of state *i*
V_{NN}	repulsion between nuclei
W_{ii}	diabatic potential of diabatic state *i*
W_{ij}	diabatic coupling potentials between states *i & j*

x	spin coordinates
Y_{lm}	angular spherical harmonic function
$Z_n(r)$	polynomial in r, n
Z_A	charge of nucleus A
ZWTS	Zwitterion transition state
$\alpha(R)$	mixing angle between adiabatic electronic states as a function of R coordinates
γ	basis function (orbital) exponent (Gaussian type)
$\Delta G_{electronic}$	stabilization energy in solvent
δ_{ij}	Krönnecker delta
ε	dielectric constant
$\in_0$	permittivity constant
$\in_i$	one-electron energy
$\in^p$	polarization vector
ζ	basis function (orbital) exponent (Slater type)
η_j	basis function
λ	coupling constant
κ	potential energy gradient (tuning mode)
Λ_{ij}	nonadiabatic coupling matrix
μ	dipole moment
$\rho(r)$	charge density
$\upsilon^{HF}(r)$	average potential experienced by each electron due to the presence of other electrons
$\lvert\Phi\rangle$	full configuration interaction expansion of ground state wave functions
ρ_i	time-independent phase
ψ^A	atomic orbital
χ	spin orbital
ψ	spatial wave function
Ψ	total wave function
Ψ_i^{ad}	adiabatic wave function of state *i*
Ψ_i^{d}	diabatic wave function of state *i*
Ψ_e	electronic wave function
Ψ^{HP}	Hartree-Product wave function
Ψ_k	momentum space wave function
Ψ^{MCSCF}	MCSCF wave function
Ψ^{MO}	molecular orbital wave function
Ψ_{eN}	nuclear wave function
$\Psi(t)$	time dependent wave function
$\lvert\Psi_0\rangle$	singlet ground state determinant
$\lvert\Psi_r^a\rangle$	singly excited determinant
$\lvert\Psi_{rs}^{ab}\rangle$	doubly excited determinant

Ψ^{i}_{trans}	translational wave function
Ψ^{i}_{υ}	rovibrational wave function
ω	frequency
ω_{ae}	frequency of the excited state along the anti-symmetric allylic stretch coordinates
ω_{ag}	frequency of the ground state along the anti-symmetric allylic stretch coordinates
ω_{se}	frequency of the excited state along the symmetric allylic stretch coordinates
ω_{sg}	frequency of the ground state along the symmetric allylic stretch coordinates
∇	Laplacian, multidimensional derivative with respect to x,y,z coordinates.
∇_{A}	Laplacian, multidimensional derivative with respect to nuclear coordinates.